ETH
Eidgenössische Technische Hochschule Zürich
Swiss Federal Institute of Technology Zurich

Exploring the Carbuncle Phenomenon in Hypersonic Flows Using the Framework of Entropy Measure Valued Solutions

Master Thesis

Muhammad Hassan

28th September, 2015

Advisor: Prof. Dr. Siddhartha Mishra
Department of Mathematics, ETH Zürich

Acknowledgements

This thesis would not have been possible without the help and support of several people. First and foremost, I would like to thank Dr. Siddhartha Mishra for agreeing to supervise this thesis. I will always be grateful to him for everything he has taught me, for always taking time out of his schedule to meet me and for his kindness and understanding.

In addition, I am grateful to Dr. Roger Käpelli for helping me run simulations on the Euler HPC Cluster, for always being willing to have a discussion with me regarding my work and for all his interesting ideas and helpful suggestions.

I would also like to thank Dr. Arnulf Jentzen for agreeing to supervise another of my semester projects and for the painstaking efforts he made to read everything I wrote and give me excellent suggestions and feedback. Thanks are also due to Deep Ray who helped me with some technical aspects of the numerical simulations and was gracious enough to allow me access to his FVM unstructured mesh solver.

I am also grateful to my friends who made my time here in Zürich very enjoyable. Finally, I wish to thank my parents and my brothers whose love and support means more to me than I can express.

Abstract

The notion of entropy measure valued solutions has recently been advocated as the appropriate framework for solutions to hyperbolic systems of conservation laws. This thesis presents the results of numerical simulations to explore the effectiveness of the entropy measure valued solution paradigm in resolving the so-called Carbuncle phenomenon in hypersonic compressible fluid flow.

We demonstrate the Carbuncle phenomenon in 1D, 1-1/2D and 2D by providing numerical evidence that even state-of-the-art entropy consistent schemes are unable to resolve a steady shock at high Mach numbers in a stable manner. We then use numerical simulations to estimate statistical quantities of interest associated with the entropy measure valued solutions such as the mean and variance.

Our results indicate that these statistical quantities suffer from less severe 1D instability and in some cases no longer suffer from 1-1/2D instability. On the other hand, these statistical quantities are still afflicted by the Carbuncle phenomenon in 2D. This leads us to conclude that the Carbuncle phenomenon is manifested in a significantly different manner in 1D, 1-1/2D and 2D, and furthermore that the limited effectiveness of the entropy measure valued solution framework at resolving this numerical instability supports the prevalent view in the literature that the Carbuncle phenomenon has a purely numerical origin.

Résumé

La notion de solutions mesurables entropiques a récemment été suggéré comme étant le cadre de travail approprié pour les solutions de systèmes hyperboliques de lois de conservation. Ce mémoire présente les résultats de simulations numériques afin d'explorer l'efficacité du paradigme de la solution mesurable entropique pour résoudre le soi-disant phénomène de Carbuncle dans un écoulement compressible hypersonique.

Nous démontrons le phénomène de Carbuncle en 1D, 1-1/2D et 2D et déduisons de nos résultats numériques que même des schémas entropiques de l'état de l'art sont incapables de discerner avec suffisamment de résolution un choc stationnaire à nombre de Mach élevé de manière stable. Nous utilisons ensuite des simulations numériques pour estimer certaines quantités statistiques d'intérêt associés aux solutions mesurables entropiques telles que la moyenne et la variance.

Nos résultats indiquent que ces quantités statistiques souffrent moins d'instabilité à 1D et que dans certains cas ne souffrent pas d'instabilité à 1-1/2D. En revanche, ces quantités statistiques sont toujours affligées par le phénomène de Carbuncle en 2D. Ceci nous porte àconclure que le phénomène de Carbuncle est manifesté de manière différente en 1D, 1-1/2D et 2D, et que l'efficacité limitée du cadre de travail des solutions mesurables entropiques pour résoudre cette instabilité numérique supporte le point de vue partagé dans la littérature que le phénomène de Carbuncle est d'origine purement numérique.

Contents

Chapter 1

Introduction

Several important problems in the physical sciences are modelled by systems of conservation laws

$$\begin{aligned} \partial_t u + \nabla_x f(u) &= 0, \\ u(x,0) &= u_0(x) \end{aligned} \tag{1.1}$$

where $d, N \in \mathbb{N}, u = u(x,t)\colon \mathbb{R}^d \times \mathbb{R}_+ \to \mathbb{R}^N$ is a vector of conserved variables and $f\colon \mathbb{R}^N \to \mathbb{R}^{N\times d}$ is the associated flux function.

The system (1.1) is called *hyperbolic* if the Jacobian of the flux function $\partial_u(f \cdot n)$ has real eigenvalues for all $n \in \mathbb{R}$ with $|n| = 1$. Prominent examples of hyperbolic systems of conservation laws include the shallow water equations from oceanography, the Euler equations from compressible fluid flow and the magnetohydrodynamics (MHD) equations from plasma physics. A rigorous treatment of the theory of hyperbolic conservation laws can, for example, be found in [11].

1.1 Theoretical Results

Solutions to the Cauchy problem (1.1) with smooth initial conditions can develop discontinuities in the form of shockwaves in finite time even for the scalar case $(N = 1)$ (see, e.g., [32]). Therefore, solutions to (1.1) are defined in the sense of *distrbutions*.

Definition 1.1 (Weak Solution) *Let $u \in \mathbb{L}^1_{loc}(\mathbb{R}^d \times \mathbb{R}_+, \mathbb{R}^N)$ be a function with the property that for all test functions $\varphi \in C^1_0(\mathbb{R}^d \times \mathbb{R}_+, \mathbb{R}^N)$ it holds that*

$$\int_{\mathbb{R}_+}\int_{\mathbb{R}^d} \partial_t \varphi(x,t)u(x,t) + \nabla_x \varphi(x,t) f\big(u(x,t)\big) dxdt + \int_{\mathbb{R}^d} \varphi(x,0)u(x,0)dx = 0. \tag{1.2}$$

Then u is called a weak solution to the Cauchy problem (1.1).

Unfortunately, weak solutions are, in general, not unique even for very simple non-linear scalar conservation laws such as Burgers' equation (see, e.g., [32]). This necessitates the imposition of additional admissibility criteria in the form of so-called *entropy conditions*.

Definition 1.2 (Entropy Pair) *Let $\eta\colon \mathbb{R}^N \to \mathbb{R}$ and $q\colon \mathbb{R}^N \to \mathbb{R}^d$ be two functions such that η is convex and such that $q' = \eta' \cdot f'$. Then (η, q) is called an entropy pair for the conservation law (1.1).*

Definition 1.3 (Entropy Solution) *Let $u \in \mathbb{L}^1_{loc}(\mathbb{R}^d \times \mathbb{R}_+, \mathbb{R}^N)$ be a weak solution to the Cauchy problem* (1.1) *with the property that for all entropy pairs (η, q) and all positive test functions $\varphi \in C^1_0(\mathbb{R}^d \times \mathbb{R}_+, \mathbb{R}^N)$ it holds that*

$$\int_{\mathbb{R}_+}\int_{\mathbb{R}^d} \partial_t \varphi(x,t)\eta\big(u(x,t)\big) + \nabla_x \varphi(x,t) q\big(u(x,t)\big) dxdt \geq 0. \tag{1.3}$$

Then u is called an entropy solution to the Cauchy problem (1.1).

Note that for the special case of scalar conservation laws, every convex function $\eta\colon \mathbb{R} \to \mathbb{R}$ gives rise to an entropy pair by defining $q\colon \mathbb{R} \to \mathbb{R}^d$ as the vector $q(u) = \int_0^u \eta'(\xi) f'(\xi) d\xi$. Specifically, defining for every $k \in \mathbb{R}$, $\eta(u) = |u - k|$, we obtain the so-called *Kruzkov entropy pairs*. These entropy pairs were used by S. N. Kruzkov to prove the existence and uniqueness of entropy solutions to the scalar Cauchy problem (1.1) [29].

Unfortunately, global well-posedness results for systems of conservation laws are much more limited in the literature. P. D. Lax proved the existence and stability of entropy solutions to the Cauchy problem (1.1) in the special case of one-dimension ($d = 1$) with Riemann initial data [31]. Existence of entropy solutions to one-dimensional Cauchy problems (1.1) with more general initial conditions was proven by S. Bianchini and A. Bressan using the vanishing viscosity method [5].

Global well-posedness results for general systems of conservation laws in several space dimensions however, do not exist in the literature. Indeed, recent results such as, .e.g, [7] show that infinitely many entropy solutions can exist for well known systems of conservation laws such as the isentropic Euler equations in two space dimensions.

1.2 Numerical Methods

Of fundamental importance in the study of systems of conservation laws is the design of numerical methods for approximating solutions to the Cauchy problem (1.1). Essentially, numerical schemes for approximating (1.1) can be divided into two broad categories. The first category consists of the so-called finite volume methods (FVM), which are based on approximate Riemann solvers and use total variation diminishing (TVD) (see, e.g., [20]), essentially non-oscillatory (ENO) (see, e.g., [21]) or weighted ENO (WENO) (see, e.g., [27]) reconstruction techniques along with strong stability preserving (SSP) Runge-Kutta methods. The second class of numerical schemes consist of the so-called discontinuous Galerkin finite element methods (DGFEM) (see, e.g., [9]).

The analysis of these numerical schemes usually involves proving convergence to an entropy solution in the limit as the mesh width is reduced to zero. Unfortunately, most results in the literature are restricted to the special case of scalar conservation laws. Monotone (first-order) schemes have been proven to converge to the entropy solution for scalar conservation laws (see, e.g., [8, 10]) and more recently arbitrarily (formally), high order schemes have also been shown to converge to the entropy solution for scalar conservation laws [19]. Similarly, convergence results have also been obtained for arbitrarily (formally) high order DGFEM schemes (see, e.g., [22, 26]).

Rigorous convergence results for generic systems of conservation laws in several space dimensions however, do not exist in the literature. Moreover, the stability of numerical approximations of solutions to systems of conservation laws is not well understood. Indeed, the only notion of numerical stability that has been analysed in detail is that of entropy stability. Essentially, numerical schemes are designed to satisfy a discrete version of the entropy inequality (1.3) but evidence indicates that this might not be sufficient to guarantee convergence to an entropy solution. Indeed, numerical examples such as the Kelvin-Helmholtz problem and the Richtmeyer-Meshkov problem (see, e.g., [18]) indicate that the numerical approximations produced by even state-of-the-art numerical methods such as the TeCNO schemes [19] do not converge to an entropy solution and are not stable under perturbations of the initial conditions [18].

1.3 The Carbuncle Problem in Hypersonic Compressible Fluid Flow

A key problem in the numerical simulation of hypersonic flows is the accurate capture of strong shocks. Indeed, over the past three decades there have been many articles in the literature that demonstrate the failure of oth-

erwise stable finite volume schemes to accurately predict strong shocks at very high Mach numbers without introducing numerical anomalies (see, e.g., [34, 35, 36]).

The term *Carbuncle phenomenon* is often used to describe this numerical instability that prevents the accurate numerical capture of shock waves (see, e.g, [34]). A precise definition of the Carbuncle phenomenon is difficult to obtain from the literature and instead the term is used to refer to a wide range of numerical problems in shock capturing. Indeed, M. Pandolfi and D. Ambrosio also refer to problems in the numerical simulation of quasi-conical shock waves around slender bodies or in the numerical simulation of interstellar flows in astrophysics as examples of the Carbuncle phenomenon [34]. Nevertheless, a large proportion of articles in the literature concern supersonic and hypersonic flows, and this will be our focus in this thesis.

Numerical artefacts were first observed by K. Peery and S. Imlay [35] when computing hypersonic flows past a circular cylinder. Instead of obtaining a smooth bow shock profile upstream of the cylinder, they observed that the solution featured a pair of oblique shocks replacing the bow shock. Interestingly, the numerical solution was still an entropy solution of the Euler equations but it was clearly fundamentally different from the expected physical solution. Since this original discovery, similar problems have been observed when computing a steady hypersonic shock in $1D$ or $1-1/2D$ by, e.g., T. Barth and F. Ismail et al [4, 23, 25, 28].

Many fixes and numerical schemes have been proposed that claim to resolve this anomaly. Most articles in the literature claim that the cause of the numerical instability is insufficient numerical diffusion and the fact that numerically diffusive schemes such as the Rusanov scheme do not suffer from this instability supports this view. Nevertheless, a universally accepted, rigorous treatment of the causes and cure of the carbuncle phenomenon is lacking in the literature (see, .e.g, [15, 25, 28, 33]). From a theoretical point of view, this is caused by the lack of an accepted explanation for this breakdown. Furthermore, verifying the claims of different schemes using numerical experiments is also troublesome because the phenomenon depends crucially on several factors such as mesh width, the positioning of the shock and the flow Mach number etc. Indeed, K. Kitamura et al have demonstrated that even extremely dissipative schemes such as the HLLE solver [14], which is widely considered to be a Carbuncle-free scheme, can display numerical instability under certain conditions [28]. An extremely comprehensive treatment of the topic can, e.g., be found in [23].

1.4 Goals and Scope of this Thesis

The discussion in the previous sections indicates that there are serious deficiencies in both the conventional mathematical paradigm of entropy solutions as well as the numerical methods that approximate entropy solutions. These inadequacies have lead to a good deal of interest in reformulating the Cauchy problem (1.1) as a more general *measure valued* (MV) Cauchy problem. Solutions to such MV Cauchy problems are then *Young measures*, which are essentially parameterised probability measures. This framework was originally introduced by R. J. DiPerna in 1983 [12] and was based on the work of L. Tartar on compensated compactness [37]. More recently, U. S. Fjordholm et al [17, 18] have expanded on these results and proven certain theoretical results as well as convergence of numerical approximations of a broad class of schemes to a so-called *entropy measure valued* (EMV) solution. In particular, the issue of lack of convergence in the Kelvin-Helmholtz and Richtmeyer-Meshkov problems has been shown to be resolved using the framework of Young measures [18].

Our purpose in this thesis is to explore the effectiveness of this new mathematical paradigm in resolving the Carbuncle phenomenon in hypersonic compressible fluid flow. Due to the difficulty of applying purely analytical methods to prove convergence or lack of convergence to a steady state solution, we will rely primarily on numerical evidence to support our arguments. The rest of this thesis is organised as follows: In Chapter 2 we give a self-contained introduction to Young measures and entropy measure valued solutions and we discuss existing results on the well-posedness of EMV solutions to both scalar conservation laws and systems of conservation laws. In Chapter 3 we discuss briefly the convergence and construction of approximate EMV solutions and we supplement this with simple numerical examples. In Chapters 4 and 5 we explore the Carbuncle phenomenon in $1D$ and $1-1/2D$ respectively, by first providing numerical evidence that state-of-the-art finite volume schemes do indeed display numerical instability when resolving a steady shock, and then considering corresponding MV Cauchy problems and using numerical simulations to estimate statistical quantities associated with the EMV solution. Our aim in Chapters 4 and 5 is to analyse the stability and convergence properties of these statistical quantities. Finally, in Chapter 6 we explore the Carbuncle phenomenon in $2D$, which arises when computing hypersonic flow past a circular cylinder. We provide numerical evidence that this instability also afflicts several finite volume schemes and we once again use numerical simulations to estimate statistical quantities associated with the EMV solution to corresponding MV Cauchy problems.

Chapter 2

Young Measures and Entropy Measure Valued Solutions

2.1 Young Measures

This section contains a brief introduction to Young measures. In an effort to keep the introduction self-contained, some elementary concepts from Probability theory and Topology are also stated. More information on these concepts can, e.g., be found in [16]. A comprehensive treatment of Young measures can, e.g., be found in [2].

2.1.1 Radon Measures and Weak* Convergence

Definition 2.1 (Borel Measure) *Let $n \in \mathbb{N}$, let $\mathcal{B}(\mathbb{R}^n)$ denote the Borel σ-algebra on $\mathbb{R}^n$ and let μ be a measure on the space $(\mathbb{R}^n, \mathcal{B}(\mathbb{R}^n))$. Then μ is called a Borel measure on $\mathbb{R}^n$.*

Definition 2.2 (Borel Regular Measure) *Let $n \in \mathbb{N}$ and let μ be a Borel measure on $\mathbb{R}^n$ such that for every $A \subset \mathbb{R}^n$, there exists a Borel set $B \in \mathcal{B}(\mathbb{R}^n)$ such that $A \subset B$ and $\mu(A) = \mu(B)$. Then the measure μ is said to be Borel regular on $\mathbb{R}^n$.*

Definition 2.3 (Radon Measure) *Let $n \in \mathbb{N}$ and let μ be a Borel regular measure on $\mathbb{R}^n$ such that for all compact sets $K \subset \mathbb{R}^n$ it holds that $\mu(K) < \infty$. Then μ is called a Radon measure.*

We denote the set of all Radon measures on $\mathbb{R}^n$ by $\mathcal{M}(\mathbb{R}^n)$. A famous result in Measure theory is the Riesz-Markov representation theorem, which establishes a link between $\mathcal{M}(\mathbb{R}^n)$ and $C_0(\mathbb{R}^n)$ i.e., the set of real-valued, continuous functions on $\mathbb{R}^n$ with compact support equipped with the *supremum* norm.

Theorem 2.4 (Riesz-Markov Representation Theorem) *Let $\psi\colon C_0(\mathbb{R}^n) \to \mathbb{R}$ be a positive linear functional. Then there exists a unique Radon measure $\mu \in \mathcal{M}(\mathbb{R}^n)$ such that for all $f \in C_0(\mathbb{R}^n)$ it holds that*

$$\langle \psi, f \rangle := \psi(f) = \int_{\mathbb{R}^n} f d\mu := \langle \mu, f \rangle. \tag{2.1}$$

A proof of Theorem 2.4 can, e.g., be found in [16]. We remark that by an abuse of notation we shall sometimes write $\langle \mu, f \rangle$ as $\langle \mu, f(\xi) \rangle$.

Essentially, Theorem 2.4 states that $\mathcal{M}(\mathbb{R}^n)$ can be associated with the dual space of $C_0(\mathbb{R}^n)$. In particular, this duality induces a weak* (or narrow) topology on $\mathcal{M}(\mathbb{R}^n)$:

Definition 2.5 (Weak* Toplogy on $\mathcal{M}(\mathbb{R}^n)$) *Let $\mathcal{T}^* \subseteq 2^{\mathcal{M}(\mathbb{R}^n)}$ be the the coarsest topology on $\mathcal{M}(\mathbb{R}^n)$ such that for every $f \in C_0(\mathbb{R}^n)$, the mapping $\mathcal{I}_f\colon \mathcal{M}(\mathbb{R}^n) \to \mathbb{R}$ given by $\mu \mapsto \int_{\mathbb{R}^n} f d\mu$ is continuous. Then $\mathcal{T}^*$ is called the weak* topology on $\mathcal{M}(\mathbb{R}^n)$.*

This leads naturally to the idea of weak* (also called weak or narrow) convergence of Radon measures:

Definition 2.6 (Weak* Convergence of Radon Measures) *Let $\mu \in \mathcal{M}(\mathbb{R}^n)$ be a Radon measure and let $\{\mu^n\}_{n\in\mathbb{N}} \subseteq \mathcal{M}(\mathbb{R}^n)$ be a sequence of Radon measures such that for all functions $f \in C_0(\mathbb{R}^n)$ it holds that*

$$\lim_{n\to\infty} \langle \mu_n, f \rangle = \langle \mu, f \rangle. \tag{2.2}$$

Then we say that the sequence $\{\mu^n\}_{n\in\mathbb{N}}$ converges weakly to μ and we denote weak convergence by $\mu^n \rightharpoonup \mu$.*

2.1.2 Probability Measures and the Wasserstein Metric

Definition 2.7 (Set of Probability Measures on $\mathbb{R}^n$) *Let $\mathcal{P}(\mathbb{R}^n) \subset \mathcal{M}(\mathbb{R}^n)$ be the set given by*

$$\mathcal{P}(\mathbb{R}^n) = \Big\{ \mu \in \mathcal{M}(\mathbb{R}^n)\colon \mu \geq 0, \mu(\mathbb{R}^n) = 1 \Big\}. \tag{2.3}$$

Then $\mathcal{P}(\mathbb{R}^n)$ is called the set of probability measures on $\mathbb{R}^n$.

Definition 2.8 (Probability Measures with Finite Moments) *Let $p \in [1, \infty)$ and let $\mathcal{P}^p(\mathbb{R}^n) \subset \mathcal{P}(\mathbb{R}^n)$ be the set given by*

$$\mathcal{P}^p(\mathbb{R}^n) = \Big\{ \mu \in \mathcal{P}(\mathbb{R}^n)\colon \langle \mu, |\xi|^p \rangle < \infty \Big\}. \tag{2.4}$$

Then $\mathcal{P}(\mathbb{R}^n)$ is called the set of probability measures on $\mathbb{R}^n$ with finite p-th moment.

Definition 2.9 (Wasserstein Metric) *Let $p \in [1, \infty)$ and let $W_p \colon \mathcal{P}^p(\mathbb{R}^n) \times \mathcal{P}^p(\mathbb{R}^n) \to [0, \infty)$ be the function given by*

$$W_p(\mu, \nu) = \inf \Big\{ \int_{\mathbb{R}^n \times \mathbb{R}^n} |\xi - \zeta|^p d\pi(\mu, \nu) \colon \pi(\mu, \nu) \in \Pi(\mu, \nu) \Big\}^{\frac{1}{p}} \tag{2.5}$$

where $\Pi(\mu, \nu)$ is the set of all probability measures on $\mathbb{R}^n \times \mathbb{R}^n$ with marginals μ and ν:

$$\Pi(\mu, \nu) = \Big\{ \pi \in \mathcal{P}(\mathbb{R}^n \times \mathbb{R}^n) \colon \pi(A \times \mathbb{R}^n) = \mu(A),\ \pi(\mathbb{R}^n \times A) = \nu(A)\ \forall A \in \mathcal{B}(\mathbb{R}^n) \Big\}. \tag{2.6}$$

Then W_p is called the Wasserstein metric on $\mathcal{P}^p(\mathbb{R}^n)$.

Of course, the fact that W_p is indeed a metric on $\mathcal{P}^p(\mathbb{R}^n)$ is non-trivial. A detailed proof can, e.g., be found in [1]. Another important fact is that W_p metrizes the topology of weak* convergence on $\mathcal{P}^p(\mathbb{R}^n)$.

2.1.3 Young Measures and Random Fields

Definition 2.10 (Young Measure) *Let $\nu \colon D \subseteq \mathbb{R}^d \to \mathcal{P}(\mathbb{R}^N)$ be a mapping with the property that for all $f \in C_0(\mathbb{R}^n)$ it holds that the function $\langle \nu, f \rangle \colon D \subseteq \mathbb{R}^d \to \mathbb{R}$ is Borel-measurable. Then ν is called a Young measure from $D \subseteq \mathbb{R}^d$ to $\mathbb{R}^n$.*

In other words, a Young measure is a weakly measurable function. We denote the set of all Young measures from $D \subseteq \mathbb{R}^d$ to $\mathbb{R}^n$ by $\mathbb{Y}(D, \mathbb{R}^n)$. Moreover, for simplicity we often write the image of a Young measure $\nu(z)$ as ν_z.

Definition 2.11 (Uniformly Bounded Young Measures) *Let $D \subset \mathbb{R}^d$, let $K \subset \mathbb{R}^n$ be a compact set and let $\nu \in \mathbb{Y}(D, \mathbb{R}^n)$ be a Young measure such that for all $x \in D$ it holds that*

$$supp \nu_x \subset K. \tag{2.7}$$

Then ν is said to be a uniformly bounded Young measure.

We remark that for the special case when ν is *atomic* i.e. there exists some function $u \colon D \subseteq \mathbb{R}^d \to \mathbb{R}^n$ such that for all $x \in D$ it holds that $\nu_x = \delta_{u(x)}$, the Young measure ν is uniformly bounded if and only if $\|u\|_{\mathbb{L}^\infty(D)} < \infty$.

The following elementary result is also extremely useful.

Proposition 2.12 *Let $u \colon \mathbb{R}^d \to \mathbb{R}^n$ be a measurable function and let $\nu \colon \mathbb{R}^d \to \mathcal{P}(\mathbb{R}^N)$ be the mapping with the property that for all $x \in \mathbb{R}^d$ it holds that*

$$\nu(x) := \nu_x = \delta_{u(x)}. \tag{2.8}$$

Then $\nu \in \mathbb{Y}(\mathbb{R}^d, \mathbb{R}^n)$.

The proof of this proposition is straightforward and is omitted for the sake of brevity.

Two notions of convergence can now be defined on $\mathbb{Y}(\mathbb{R}^d, \mathbb{R}^n)$:

Definition 2.13 (Narrow Convergence) *Let $D \subseteq \mathbb{R}^d$, let $\nu \in \mathbb{Y}(D, \mathbb{R}^n)$ be a Young measure and let $\{\nu^n\}_{n\in\mathbb{N}} \subseteq \mathbb{Y}(D, \mathbb{R}^n)$ be a sequence of Young measures such that for all $f \in C_0(\mathbb{R}^n)$ and all test functions $\varphi \in \mathbb{L}^1(D)$ it holds that*

$$\lim_{n\to\infty} \int_D \varphi(x) \langle \nu_x^n, f \rangle dx = \int_D \varphi(x) \langle \nu_x, f \rangle dx. \tag{2.9}$$

Then we say that the sequence ν^n converges in the narrow sense to ν and we write $\nu^n \xrightarrow{*} \nu$.

Definition 2.14 (Strong Convergence) *Let $p \in [1, \infty)$, let $D \subseteq \mathbb{R}^d$, let $\nu \in \mathbb{Y}(D, \mathbb{R}^n)$ be a Young measure and let $\{\nu^n\}_{n\in\mathbb{N}} \in \mathbb{Y}(D, \mathbb{R}^n)$ be a sequence of Young measures such that*

$$\lim_{n\to\infty} \| W_p(\nu^n, \nu) \|_{\mathbb{L}^p(D)} = 0. \tag{2.10}$$

Then we say that the sequence ν^n converges in the strong sense to ν and we write $\nu^n \to \nu$.

An important result is the fundamental theorem of Young Measures, which essentially states that under some mild boundedness conditions, every sequence of Young measures has a narrowly convergent subsequence. A comprehensive proof and discussion of this theorem can be found in a classic paper of J. M. Ball [3]. We state a slightly more generalised version of this theorem found in [18].

Theorem 2.15 (Fundamental Theorem of Young Measures) *Let $N_0 \in \mathbb{N}$, let $D \subseteq \mathbb{R}^d$ and let $\{\nu^n\}_{n\in\mathbb{N}} \subseteq \mathbb{Y}(D, \mathbb{R}^n)$ be a sequence of Young measures. Then there exists a subsequence $\{\nu^{n_k}\}_{n_k\in\mathbb{N}}$ of Young measures and a non-negative measure valued function $\nu \colon D \to \mathcal{M}_+(\mathbb{R}^n)$ such that*

- $\nu^{n_k} \xrightarrow{*} \nu$,
- $\|\nu_x\|_{\mathcal{M}(\mathbb{R}^n)} \leq 1$ *for a. e. $x \in D$,*
- *and if $K \subseteq \mathbb{R}^n$ is a closed set such that for all $n \geq N_0$ it holds that $supp\nu_x^n \subset K$ for a. e. $x \in D$, then $supp\nu_x \subset K$ for a. e. $x \in D$.*

Furthermore, suppose that for every measurable and bounded set $E \subset D$, there exists a non-negative function $\rho \in C(\mathbb{R}^n)$ such that $\lim_{|\xi|\to\infty} \rho(\xi) = \infty$ and with the property that

$$\sup_{n\in\mathbb{N}} \int_E \langle \nu_x^n, \rho \rangle dx < \infty. \tag{2.11}$$

Then it holds that $\|\nu_x\|_{\mathcal{M}(\mathbb{R}^n)} = 1$ for a. e. $x \in D$ and therefore $\nu \in \mathbb{Y}(D, \mathbb{R}^n)$.

The proof of this theorem can be found in the appendix of [18].

We remark that for the special case in which $\rho \in C(\mathbb{R}^n)$ is the function with the property that for all $\xi \in \mathbb{R}^n$ it holds that $\rho(\xi) = |\xi|^p$ for some $p \in [1, \infty)$, the inequality (2.11) simplifies to

$$\sup_{n \in \mathbb{N}} \int_D \langle \nu_x^n, |\xi|^p \rangle dx < \infty, \tag{2.12}$$

which is essentially an $\mathbb{L}^p$-bound.

Another important concept is the connection between Young measures and *random fields*.

Definition 2.16 (Random Fields) *Let $(\Omega, \mathcal{F}, \mathbb{P})$ be a probability space, let $D \in \mathcal{B}(\mathbb{R}^d)$ and let $u \colon \Omega \times D \to \mathbb{R}^n$ be a function with the property that for all $x \in D$, the mapping $\omega \mapsto u(\omega, x)$ is $\mathcal{F}$-measurable. Then u is called a random field.*

Definition 2.17 (Law of a Random Field) *Let $(\Omega, \mathcal{F}, \mathbb{P})$ be a probability space, let $D, F \in \mathcal{B}(\mathbb{R}^d)$ and let $u \colon \Omega \times D \to \mathbb{R}^n$ be a random field. Then the law of the random field u is given by*

$$\nu_z(F) := \mathbb{P}\big(u(., z) \in F\big) = \mathbb{P}\big(\{\omega \in \Omega \colon u(\omega, z) \in F\}\big), \tag{2.13}$$

or equivalently, for all $f \in C_0(\mathbb{R}^n)$ it holds that

$$\langle \nu_z, f \rangle := \int_\Omega f(u(\omega, z)) dP(\omega). \tag{2.14}$$

In the special case where the random field is also jointly-measurable, the law of the random field in fact defines a Young measure.

Proposition 2.18 *Let $(\Omega, \mathcal{F}, \mathbb{P})$ be a probability space, let $D, F \in \mathcal{B}(\mathbb{R}^d)$ and let $u \colon \Omega \times D \to \mathbb{R}^n$ be a random field with the property that u is $\big(\mathcal{F} \otimes \mathcal{B}(\mathbb{R}^d)\big)$-measurable. Then the law of the random field u defines a Young measure from D to $\mathbb{R}^n$.*

The proof is straightforward and can, e.g., be found in the appendix of [18].

Interestingly, the converse statement is also true: for every Young measure ν, it is possible to construct a random variable with law given by ν.

Proposition 2.19 *Let $D \in \mathbb{R}^d$ and let $\nu \in \mathbb{Y}(D, \mathbb{R}^n)$ be a Young measure. Then there exists a probability space $(\Omega, \mathcal{F}, \mathbb{P})$ and an $\big(\mathcal{F} \otimes \mathcal{B}(\mathbb{R}^d)\big)$-measurable function $u \colon \Omega \times D \to \mathbb{R}^n$ with the property that for all Borel sets $B \in \mathcal{B}(\mathbb{R}^d)$ it holds that*

$$\nu_z(B) = \mathbb{P}\big(u(\omega, z) \in B\big). \tag{2.15}$$

This proof can also be found, e.g., in the appendix of [18]. The major implication of Propositions 2.18 and 2.19 is that every Young measure can be associated with the law of a jointly measurable random field.

2.2 Entropy Measure Valued Solutions

We can now state the measure valued (MV) Cauchy problem corresponding to the Cauchy problem (1.1).

Definition 2.20 (Measure Valued Cauchy Problem) *Let $d, n \in \mathbb{N}$, let $\nu \in \mathbb{Y}(\mathbb{R}^d \times \mathbb{R}_+, \mathbb{R}^n)$, $\sigma \in \mathbb{Y}(\mathbb{R}^d, \mathbb{R}^n)$ be two Young measures, let $f\colon \mathbb{R}^d \to \mathbb{R}^{n\times d}$ be the flux function and let $id\colon \mathbb{R}^n \to \mathbb{R}^n$ be the identity function. Then the measure valued (MV) Cauchy problem corresponding to* (1.1) *is given by*

$$\begin{aligned} \partial_t \langle \nu, id \rangle + \nabla_x \cdot \langle \nu, f \rangle &= 0, \\ \nu_{(x,0)} &= \sigma_x. \end{aligned} \tag{2.16}$$

Solutions to the MV Cauchy Problem (2.16) are defined in the following way:

Definition 2.21 (Measure Valued (MV) Solutions) *Let $\nu \in \mathbb{Y}(\mathbb{R}^d \times \mathbb{R}_+, \mathbb{R}^n)$ be a Young measure with the property that for all test functions $\varphi \in C_0^1(\mathbb{R}^d \times \mathbb{R}_+, \mathbb{R}^N)$ it holds that*

$$\begin{aligned} \int_{\mathbb{R}_+} \int_{\mathbb{R}^n} \partial_t \varphi(x,t) \langle \nu_{(x,t)}, id \rangle + \nabla_x \varphi(x,t) \cdot \langle \nu_{(x,t)}, f \rangle dx dt \\ + \int_{\mathbb{R}^d} \varphi(x,0) \langle \sigma_x, id \rangle dx = 0. \end{aligned} \tag{2.17}$$

Then ν is called a measure valued (MV) solution to the MV Cauchy problem (2.16)*.*

Definition 2.22 (Entropy Measure Valued (EMV) Solutions) *Let $\nu \in \mathbb{Y}(\mathbb{R}^d \times \mathbb{R}_+, \mathbb{R}^n)$ be an MV solution to the MV Cauchy problem* (2.16) *with the property that for every entropy pair (η, q) and every non-negative test function $\varphi \in C_0^1(\mathbb{R}^d \times \mathbb{R}_+, \mathbb{R}^N)$ it holds that*

$$\begin{aligned} \int_{\mathbb{R}_+} \int_{\mathbb{R}^n} \partial_t \varphi(x,t) \langle \nu_{(x,t)}, \eta \rangle + \nabla_x \varphi(x,t) \cdot \langle \nu_{(x,t)}, q \rangle dx dt \\ + \int_{\mathbb{R}^d} \varphi(x,0) \langle \sigma_x, \eta \rangle dx \geq 0. \end{aligned} \tag{2.18}$$

Then ν is called an entropy measure valued (EMV) solution to the MV Cauchy problem (2.16)*.*

We denote the set of all entropy solutions to the MV Cauchy problem (2.16) by $\mathcal{E}_{f,\sigma}$. It is immediately seen that $\left|\mathcal{E}_{f,\sigma}\right|$ is at least as large the number of entropy solutions to the corresponding Cauchy problem (1.1) since every entropy solution u gives rise to an EMV solution by defining $\nu \in \mathbb{Y}(\mathbb{R}^d \times \mathbb{R}_+, \mathbb{R}^n)$ as the Young measure with the property that for all $(x,t) \in \mathbb{R}^d \times \mathbb{R}_+$ it holds that $\nu_{(x,t)} = \delta_{u(x,t)}$. In particular, it immediately follows that EMV solutions are a more general notion that simple entropy solutions.

2.3 Well-Posedness of Entropy Measure Valued Solutions

This section contains a discussion of the existence and uniqueness of EMV solutions to the MV Cauchy problem (2.16). The entire construction of the mathematical framework of EMV solutions is based on the hope that the fundamental question of well-posedness can be resolved. While it is currently not possible to prove global well-posedness of EMV solutions to a generic MV Cauchy problem (2.16), some promising results for special cases can be stated and proven (see, e.g., [18]).

2.3.1 Scalar Conservation Laws

Theorem 2.23 (Existence of EMV Solutions) *Consider the MV Cauchy problem* (2.16) *in the special case* $N = 1$ *and the Young measure* $\sigma \in \mathbb{Y}(\mathbb{R}, \mathbb{R})$ *be uniformly bounded. Then there exists an EMV solution to* (2.16)*.*

The proof of Theorem 2.23 is straightforward and relies on the properties of Young measures that were stated in Section 2.2. We omit this proof for the sake of brevity but a detailed argument can be found in [18].

Remark It is important to note that the proof of Theorem 2.23 relies on the implicit assumption that an entropy solution to the corresponding scalar Cauchy problem (1.1) is known to exist. It would be an interesting exercise to construct a proof of this theorem without explicitly utilising a priori our knowledge of the existence of an entropy solution.

Unfortunately, as the next example indicates, uniqueness of EMV solutions does not hold in general.

Example 2.24 (Non-uniqueness of EMV Solutions) *Consider the one-dimensional inviscid Burgers' equation given by*

$$\partial_t u + \partial_x \left(\frac{u^2}{2}\right) = 0. \tag{2.19}$$

Let $\Omega = [0,1]$, $\mathcal{F} = \mathcal{B}\big([0,1]\big)$, $\mathbb{P} = \lambda_{[0,1]}$, *let* $u_0 \colon \Omega \times \mathbb{R} \to \mathbb{R}$ *be the* $\mathcal{F} \otimes \mathcal{B}(\mathbb{R})$*-measurable mapping with the property that for all* $\omega \in \Omega$ *it holds that*

$$u_0(\omega, x) = \begin{cases} 1/2 + \omega & \text{for } x < 0, \\ 1/2 - \omega & \text{for } x > 0 \end{cases} \tag{2.20}$$

and let $\tilde{u}_0 \colon \Omega \times \mathbb{R} \to \mathbb{R}$ *be the* $\mathcal{F} \otimes \mathcal{B}(\mathbb{R})$*-measurable mapping with the property that for all* $\omega \in \Omega$ *it holds that*

$$\tilde{u}_0(\omega, x) = \begin{cases} 3/2 - \omega & \text{for } x < 0, \\ 1/2 - \omega & \text{for } x > 0. \end{cases} \tag{2.21}$$

Then, the law of both u_0 and $\tilde{u}_0$ is given by

$$\sigma_x = \begin{cases} \lambda_{[1/2,3/2]} & \text{for } x < 0, \\ \lambda_{[-1/2,1/2]} & \text{for } x > 0. \end{cases} \tag{2.22}$$

The entropy solution $u\colon \mathbb{R} \times \mathbb{R}_+ \to \mathbb{R}$ of the system (2.19) *with initial condition* (2.20) *is given by*

$$u(x,t) = \begin{cases} 1/2 + \omega & \text{for } x < \frac{t}{2}, \\ 1/2 - \omega & \text{for } x > \frac{t}{2} \end{cases} \tag{2.23}$$

and the entropy solution $\tilde{u}\colon \mathbb{R} \times \mathbb{R}_+ \to \mathbb{R}$ of the system (2.19) *with initial condition* (2.21) *is given by*

$$\tilde{u}(x,t) = \begin{cases} 3/2 - \omega & \text{for } x < t - \omega t, \\ 1/2 - \omega & \text{for } x > t + \omega t. \end{cases} \tag{2.24}$$

The law ν of u is therefore given by

$$\nu_{(x,t)} = \begin{cases} \lambda_{[1/2,3/2]} & \text{for } x < \frac{t}{2}, \\ \lambda_{[-1/2,1/2]} & \text{for } x > \frac{t}{2} \end{cases} \tag{2.25}$$

and the law $\tilde{\nu}$ of $\tilde{u}$ is given by

$$\tilde{\nu}_{(x,t)} = \begin{cases} \lambda_{[1/2,3/2]} & \text{for } x < 0, \\ \lambda_{[-1/2,x/t-1/2]} + \lambda_{[x/t+1/2,3/2]} & \text{for } 0 < x < t, \\ \lambda_{[-1/2,1/2]} & \text{for } x > t. \end{cases} \tag{2.26}$$

Therefore, both $\nu, \tilde{\nu} \in \mathcal{E}_{f,\sigma}$ and hence $\left|\mathcal{E}_{f,\sigma}\right| > 1$.

Clearly therefore, we cannot expect uniqueness of EMV solutions to a generic MV Cauchy problem (2.16). In the special case of atomic initial data however, the following stability result holds.

Theorem 2.25 (Stability of EMV Solutions) *Consider the MV Cauchy problem* (2.16) *in the special case $N = 1$, let $Id\colon \mathbb{R} \to \mathbb{R}$ be the identity function, let $u_0 \in \mathbb{L}^\infty(\mathbb{R}^d)$, let $\sigma \in \mathbb{Y}(\mathbb{R}^d, \mathbb{R})$ be a uniformly bounded Young measure, let $u \in \mathbb{L}^\infty(\mathbb{R}^d \times \mathbb{R}_+, \mathbb{R})$ be the entropy solution of the Cauchy problem* (1.1) *with initial condition u_0, let $\nu \in \mathbb{Y}(\mathbb{R}^d \times \mathbb{R}_+, \mathbb{R})$ be an EMV solution of the MV Cauchy problem* (2.16) *with initial data $\sigma \in \mathbb{Y}(\mathbb{R}^d, \mathbb{R})$ and with the property that*

$$\frac{1}{T} \int_0^T \int_{\mathbb{R}^d} \left\langle \nu_{(x,t)}, |u_0(x) - Id| \right\rangle dx dt = 0. \tag{2.27}$$

Then for all $t > 0$ it holds that

$$\int_{\mathbb{R}^d} \langle \nu_{(x,t)}, |u(x,t) - Id| \rangle dx \leq \int_{\mathbb{R}^d} \langle \sigma_x, |u_0(x) - Id| \rangle dx, \tag{2.28}$$

or equivalently, for all $t > 0$ it holds that

$$\| W_1(\nu_{(.,t)}, \delta_{u(.,t)}) \|_{\mathbb{L}^1(\mathbb{R}^d)} \leq \| W_1(\sigma, \delta_{u_0}) \|_{\mathbb{L}^1(\mathbb{R}^d)}. \tag{2.29}$$

In particular $\sigma = \delta_{u_0} \implies \nu = \delta_u$.

The proof of Theorem 2.25 can be found in [18].

2.3.2 Systems of Conservation Laws

As mentioned previously, it is too much to expect a uniqueness or stability result for MV Cauchy problems (2.16) involving a generic hyperbolic system of conservation laws. However, in the case when the corresponding Cauchy problem (1.1) is known to have a *classical* solution, the following stability result holds:

Theorem 2.26 (Stability of Perturbations of Classical Solutions) *Let $K \subset \mathbb{R}^n$ be a compact set, let $Id \colon \mathbb{R}^n \to \mathbb{R}^n$ be the identity function, let $u_0 \colon \mathbb{R}^d \to K$, let $u \in W^{1,\infty}(\mathbb{R}^d \times \mathbb{R}_+, K)$ be a classical solution of the the Cauchy problem* (1.1) *with initial condition u_0, let $\sigma \in \mathbb{Y}(\mathbb{R}^d, \mathbb{R}^n)$ with $supp\sigma \subset K$, let $\nu \in \mathbb{Y}(\mathbb{R}^d \times \mathbb{R}_+, \mathbb{R})^d$ with $supp\nu \subset K$ and let the associated entropy function $\eta \colon \mathbb{R}^n \to \mathbb{R}$ be uniformly convex on K. Then there exists a constant $C \in \mathbb{R}$ such that for all $t > 0$ it holds that*

$$\int_{\mathbb{R}^d} \langle \nu_{(x,t)}, |u(x,t) - Id|^2 \rangle dx \leq C(1 + te^{Ct}) \int_{\mathbb{R}^d} \langle \sigma_x, |u_0(x) - Id|^2 \rangle dx, \tag{2.30}$$

or equivalently, there exists a constant $C \in \mathbb{R}$ such that for all $t > 0$ it holds that

$$\| W_2(\nu_{(.,t)}, \delta_{u(.,t)}) \|_{\mathbb{L}^2(\mathbb{R}^d)} \leq C(1 + te^{Ct}) \| W_2(\sigma, \delta_{u_0}) \|_{\mathbb{L}^2(\mathbb{R}^d)}. \tag{2.31}$$

In particular $\sigma = \delta_{u_0} \implies \nu = \delta_u$ and therefore there exists a unique classical, weak and entropy solution.

The proof of Theorem 2.26 can also be found in [18].

Remark Note that Theorem 2.26 proves the consistency of EMV solutions with classical solutions when they exist. In particular, this implies local uniqueness in time of the MV solutions for as long as a unique classical solution exists.

Chapter 3

Approximate EMV Solutions

The discussion in Chapter 2 was limited to a theoretical study of the framework of EMV solutions to the MV Cauchy problem (2.16). This Chapter will briefly discuss the construction and convergence properties of numerical approximations of EMV solutions. A detailed exposition on this subject can be found in [18].

For clarity of exposition we restrict ourselves to the case of two spatial dimensions ($d = 2$). We first set up some notation. The computational domain is discretised into cells $\mathcal{C}_i := [x_{i-\frac{1}{2}}, x_{i+\frac{1}{2}}) \times [y_{i-\frac{1}{2}}, y_{i+\frac{1}{2}})$ with uniform mesh width denoted by Δx and Δy in the x and y directions respectively. We denote by u_0^Δ the numerical approximation of the initial data, by $\mathcal{S}^\Delta$ the discrete evolution operator associated with a given numerical scheme, by u^Δ the numerical approximation of the solution u and by ν^Δ the law of u^Δ.

3.1 Convergence of Approximate EMV Solutions

The main convergence result on numerical approximations of EMV Solutions to the MV Cauchy problem (2.16) is given below.

Theorem 3.1 (Convergence) *Let $u^\Delta \colon \Omega \times \mathbb{R}_+ \to \mathbb{L}^\infty(\mathbb{R}^2, \mathbb{R}^n)$ denote the numerical approximation of the random field $u \colon \Omega \times \mathbb{R}_+ \to \mathbb{L}^\infty(\mathbb{R}^2, \mathbb{R}^n)$ whose law is the EMV solution to* (2.16) *and suppose that u^Δ satisfies the following conditions:*

- *Uniform boundedness: there exists some constant $C \in \mathbb{R}$ such that for all $\omega \in \Omega$ it holds that*

$$\|u^\Delta(\omega)\|_{\mathbb{L}^\infty(\mathbb{R}^d, \mathbb{R}^n)} \leq C. \tag{3.1}$$

- *Weak Bounded Variation: there exists $1 \leq r < \infty$ such that that for all*

$\omega \in \Omega$ *it holds that*

$$\lim_{\Delta x,\Delta y\to 0}\int_0^T \sum_{i,j}\Big(\big|u^\Delta_{i+1,j}(\omega,t)-u^\Delta_{i,j}(\omega,t)\big|^r + \big|u^\Delta_{i,j+1}(\omega,t)-u^\Delta_{i,j}(\omega,t)\big|^r\Big)\Delta x\Delta y dt = 0. \tag{3.2}$$

- *Entropy Consistency: there exists some entropy pair* (η, q) *such that the numerical approximations* u^Δ *satisfy the semi-discrete entropy inequality.*
- *Consistency with initial data: for all test functions* $\psi \in C_0^1(\mathbb{R}^2)$ *the law* σ^Δ *of the initial data* $u_0^\Delta \colon \Omega \to \mathbb{L}^\infty(\mathbb{R}^2,\mathbb{R}^n)$ *satisfies*

$$\lim_{\Delta x,\Delta y\to 0}\int_{\mathbb{R}^2}\psi(x,y)\langle \sigma^\Delta_{(x,y)}, id\rangle dxdy = \int_{\mathbb{R}^2}\psi(x,y)\langle \sigma_{(x,y)}, id\rangle dxdy, \tag{3.3}$$

and for all for all positive test functions $\psi \in C_0^1(\mathbb{R}^2)$ *the law* σ^Δ *of the initial data* u_0^Δ *satisfies*

$$\limsup_{\Delta x,\Delta y\to 0}\int_{\mathbb{R}^2}\psi(x,y)\langle \sigma^\Delta_{(x,y)}, \eta\rangle dxdy \le \int_{\mathbb{R}^2}\psi(x,y)\langle \sigma_{(x,y)}, \eta\rangle dxdy. \tag{3.4}$$

Then the approximate Young measures ν^Δ *converge in the narrow sense up to a subsequence to an EMV solution* $\nu \in \mathbb{Y}(\mathbb{R}^2\times\mathbb{R}_+,\mathbb{R}^n)$ *of the MV Cauchy problem* (2.16) *as* $\Delta x, \Delta y \to 0$.

The proof of Theorem 3.1 can be found in [18].

3.2 Construction of Approximate EMV Solutions

Since the uniqueness of EMV solutions to (2.16) can only be guaranteed in the case of atomic initial data, it makes sense to focus on the special case where $\sigma = \delta_{u_0}$ for some function $u_0 \in \mathbb{L}^\infty(\mathbb{R}^d,\mathbb{R}^n)\cap\mathbb{L}^1(\mathbb{R}^d,\mathbb{R}^n)$. U. S. Fjordholm et al propose the following algorithm to construct approximate EMV solutions.

Algorithm Let $(\Omega,\mathcal{F},\mathbb{P})$ be a probability space and let $X\colon \Omega\to\mathbb{L}^\infty(\mathbb{R}^d,\mathbb{R})\cap\mathbb{L}^1(\mathbb{R}^d,\mathbb{R})$ be a measurable mapping such that $\|X\|_{\mathbb{L}^1(\mathbb{R}^d)} \le 1$ P-almost surely.

- Fix a real number $\varepsilon \ll 1$, perturb u_0 by defining $u_0^\varepsilon(\omega,x) := u_0(x) + \varepsilon X(\omega,x)$ and let σ^ε be the law of u_0^ε.
- For each $\omega\in\Omega$ and $\varepsilon > 0$, let $u^{\Delta,\varepsilon}(\omega) := \mathcal{S}^\Delta u_0^\varepsilon(\omega)$ where $\mathcal{S}^\Delta$ is the discrete evolution operator corresponding to the numerical scheme.

- Define $\nu^{\Delta,\varepsilon}$ to be the law of $u_0^{\Delta,\varepsilon}$.

In practice we are primarily interested in statistical quantities such as the mean and the moments of the entropy measure valued solution. Thus, in practice we can use Monte Carlo approximations to obtain an ensemble average for many such values of ε in order to estimate these quantities.

Examples of Narrowly Convergent Numerical Schemes U. S. Fjordholm et al identify at least three broad classes of numerical methods that produce approximations that converge in the narrow sense to an EMV solution.

- All monotone finite volume schemes for scalar conservation laws are uniformly bounded in $\mathbb{L}^\infty$, satisfy a discrete entropy inequality and are TVD. Hence, they satisfy the hypothesis of Theorem 3.1 and are therefore narrowly convergent.
- In addition, the class of TeCNO schemes introduced by U. S. Fjordholm et al in [19] is an example of formally, arbitrarily high order narrowly convergent schemes.
- Finally, as shown by A. Hiltebrand and S. Mishra in [22], space-time DGFEM methods are also narrowly convergent schemes.

3.3 Numerical Examples

3.3.1 Burgers' Equation

As a first example of an application of the algorithm proposed in Section 3.2, we consider a Cauchy problem involving Burgers equation.

Let $(\Omega, \mathcal{F}, \mathbb{P})$ be a probability space, let $X\colon \Omega \to [-0.5, 0.5]$ and $Y\colon \Omega \to [-0.5, 0.5]$ be independent, uniformly distributed random variables, let $\alpha, \beta \in \mathbb{R}$ be small constants and consider the Cauchy problem

$$\begin{aligned} \partial_t u + \partial_x\Big(\frac{u^2}{2}\Big) &= 0, \\ u(x,0) &= u_0(x,\omega) \end{aligned} \tag{3.5}$$

where

$$u_0(x,\omega) = \begin{cases} 1 + \alpha X(\omega) & \text{if} \quad x < 0, \\ 0 + \beta Y(\omega) & \text{if} \quad x > 0. \end{cases} \tag{3.6}$$

For the purpose of this experiment, we restrict our spatial computational domain to the interval $[-1, 1]$ and employ so-called *transparent* boundary conditions. Our aim is to use Monte-Carlo simulations to estimate the mean and variance of the approximate measure valued solutions to the associated MV Cauchy problem. This will allow us to analyse the convergence of the

MV solution as the mesh width is refined and as the amplitude of perturbations α, β is decreased. All results are computed using 400 Monte-Carlo iterations and using an entropy stable scheme with *Roe*-type numerical diffusion (see, e.g., [17]).

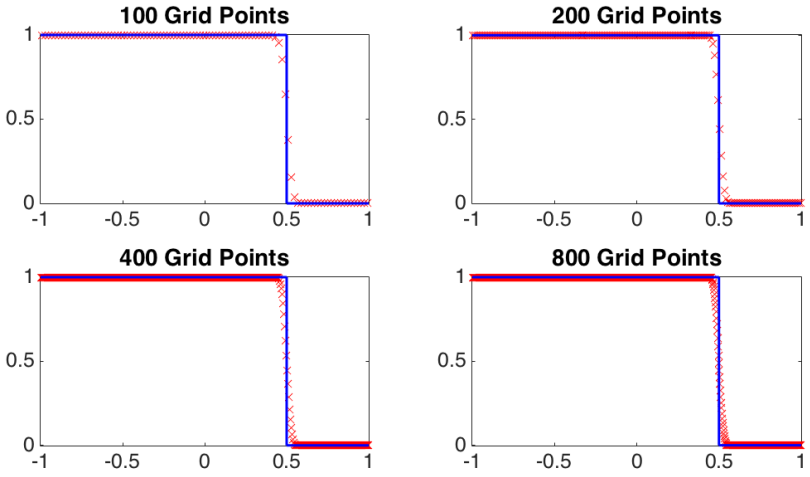

Figure 3.1 – Approximate ensemble mean and the exact solution at time $t = 1$ with perturbations $\alpha = \beta = 0.1$ and different mesh widths.

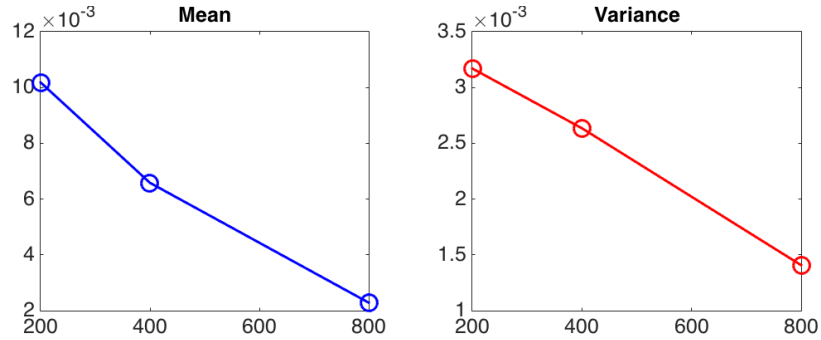

Figure 3.2 – Cauchy Rates for the ensemble mean as a function of the total number of mesh points.

We begin by computing the Monte-Carlo approximation of the mean, denoted by $\bar{u}_{x,1}^{\Delta x}$ of the probability measures $\nu_{x,1}^{\Delta x}$ for different values of the mesh width. Figure 3.1 displays our results and indicates that this mean seems to converge to the exact solution as the number of mesh points is increased. To further verify this convergence, we calculate the $\mathbb{L}^1$-norm of the successive differences in the ensemble mean across the different mesh widths:

$$\|\bar{u}_{x,1}^{\Delta x} - \bar{u}_{x,1}^{\Delta \frac{x}{2}}\|_{\mathbb{L}^1(\mathbb{R})}. \tag{3.7}$$

As shown in Figure 3.2, the approximations indeed seem to form a Cauchy sequence and are therefore convergent.

Next, we calculate the Monte-Carlo approximation of the variance of the probability measures $\nu_{x,1}^{\Delta x}$ for different values of the mesh width. Figure 3.3 displays our results and indicate that the variance also seems to converge to a sharp peak at the location of the shock.

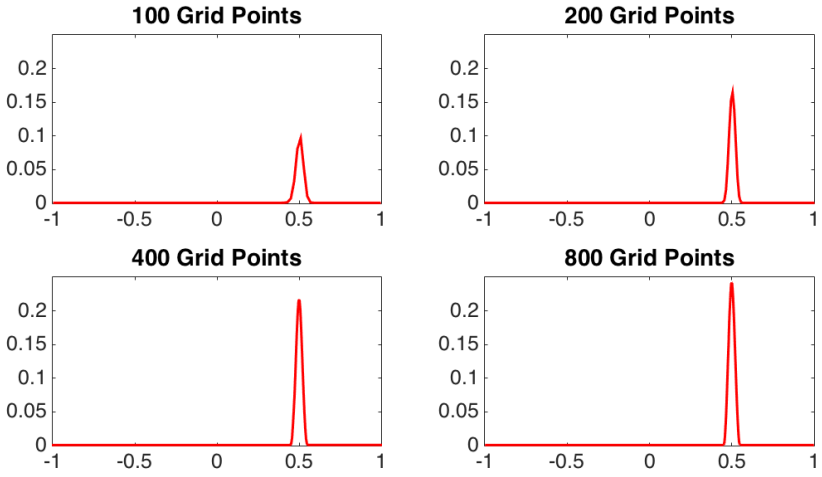

Figure 3.3 – Approximate ensemble variance at time $t = 1$ with perturbation amplitude $\alpha = \beta = 0.1$ and different mesh widths.

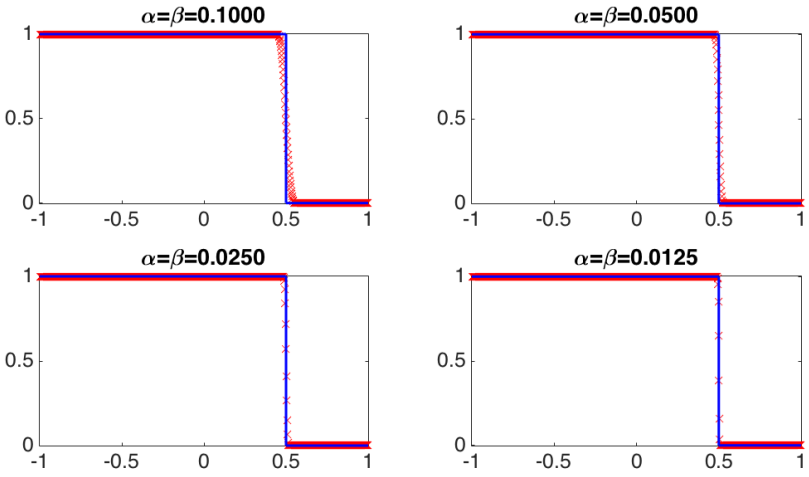

Figure 3.4 – Approximate ensemble mean at time $t = 1$ with 800 mesh points for different values of the amplitude of perturbation.

We also wish to explore the effect of the perturbation amplitude α and β on

the convergence of the ensemble mean and variance. We therefore calculate the Monte-Carlo approximation of the ensemble mean, denoted by $\bar{u}_{x,1}^{\Delta x}$ of the probability measures $\nu_{x,1}^{\Delta x}$ for different values of the perturbation $\alpha = \beta$. Figure 3.4 displays our results and indicates that this mean seems to converge to the exact solution as $\alpha, \beta \to 0$. To further verify this convergence, we again calculate the $\mathbb{L}^1$-norm of the successive differences in the ensemble mean and variance across decreasing values of $\alpha = \beta$. As shown in Figure 3.5, the approximations indeed seem to form a Cauchy sequence and are therefore convergent.

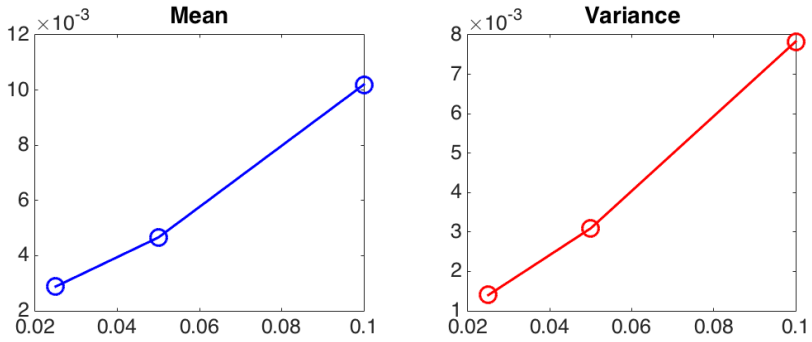

Figure 3.5 – Cauchy Rates for the ensemble mean and variance as a function of amplitude of perturbation $\alpha = \beta$.

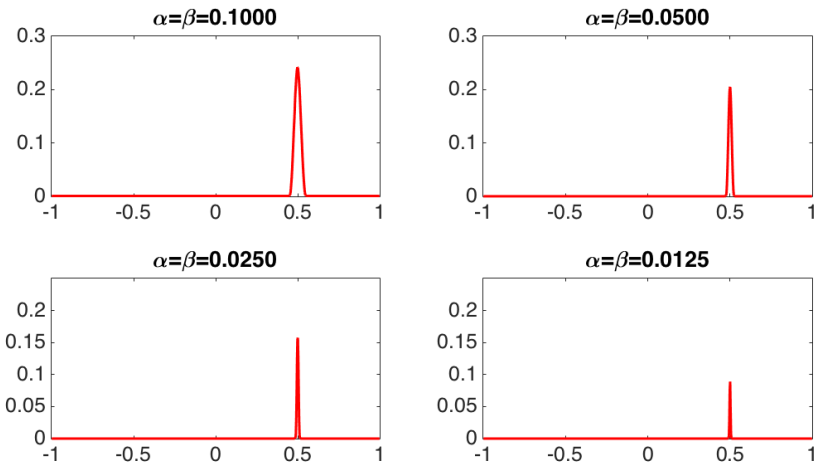

Figure 3.6 – Approximate ensemble variance at time $t = 1$ with 800 mesh points for different values of the amplitude of perturbation.

Finally, we calculate the Monte-Carlo approximation of the variance of the probability measures $\nu_{x,1}^{\Delta x}$ for decreasing values of the perturbation amplitude. Figure 3.6 displays our results and indicates that the variance seems to vanish as $\alpha, \beta \to 0$.

3.3.2 One-Dimensional Euler Equations

Let $\rho : \mathbb{R} \times \mathbb{R}_+ \to \mathbb{R}_+$, let $p : \mathbb{R} \times \mathbb{R}_+ \to \mathbb{R}_+$, let $u : \mathbb{R} \times \mathbb{R}_+ \to \mathbb{R}$ and let $E : \mathbb{R} \times \mathbb{R}_+ \to \mathbb{R}_+$ be functions which denote the density, pressure, one-dimensional velocity and energy density of a compressible, inviscid fluid. Then the compressible Euler equations in one dimension are given by

$$\begin{aligned} \partial_t \rho + \partial_x(\rho u) &= 0, \\ \partial_t(\rho u) + \partial_x\big(\rho u^2/2 + p\big) &= 0, \\ \partial_t E + \partial_x\big(u(E+p)\big) &= 0. \end{aligned} \tag{3.8}$$

Of course (3.8) is not a closed system and we require an additional equation relating the energy to the pressure and density. In the case of a polytropic, ideal gas with adiabatic exponent γ, the equation of state is given by

$$E = \frac{p}{\gamma - 1} + \frac{1}{2}\rho u^2. \tag{3.9}$$

For the sake of brevity we can write (3.8) in the more compact form

$$\partial_t\, \mathbf{u} + \partial_x(\, \mathbf{F}) = 0 \tag{3.10}$$

where

$$\mathbf{u} = \begin{bmatrix} \rho \\ \rho u \\ E \end{bmatrix}, \qquad \mathbf{F} = \begin{bmatrix} \rho u \\ \rho u^2/2 \\ \big(u(E+p)\big) \end{bmatrix}. \tag{3.11}$$

We now consider the following Cauchy problem involving the Euler equations (3.10). Let $(\Omega, \mathcal{F}, \mathbb{P})$ be a probability space, let $X \colon \Omega \to [-0.5, 0.5]$ and $Y \colon \Omega \to [-0.5, 0.5]$ be independent, uniformly distributed random variables, let $\alpha, \beta \in \mathbb{R}$ be small constants and consider the Cauchy problem

$$\begin{aligned} \partial_t \mathbf{u} + \partial_x(\mathbf{F}) &= 0, \\ \mathbf{u}(x, 0) &= \mathbf{u}_0(x, \omega) \end{aligned} \tag{3.12}$$

where

$$\mathbf{u}_0(x, \omega) = \begin{cases} \begin{bmatrix} 1 + \alpha X(\omega) \\ 0 + \alpha X(\omega) \\ 2.5 + \alpha X(\omega) \end{bmatrix} & \text{if} \quad x < 0, \\ \begin{bmatrix} 0.125 + \beta Y(\omega) \\ 0 + \beta Y \\ 0.25 + \beta Y \end{bmatrix} & \text{if} \quad x > 0. \end{cases} \tag{3.13}$$

Thus the Cauchy problem (3.12) is essentially the sod-shock tube problem with perturbed initial conditions. Once again we restrict our spatial computational domain to the interval $[-2, 2]$ and employ *transparent* boundary conditions. We shall use Monte-Carlo simulations to estimate the mean and variance of the approximate measure valued solutions to the associated MV Cauchy problem and analyse the convergence of these statistical quantities with respect to mesh width and the perturbation amplitudes. All results are computed using 400 Monte-Carlo iterations and using a first order entropy stable scheme with *Rusanov*-type numerical diffusion (see, e.g., [17]).

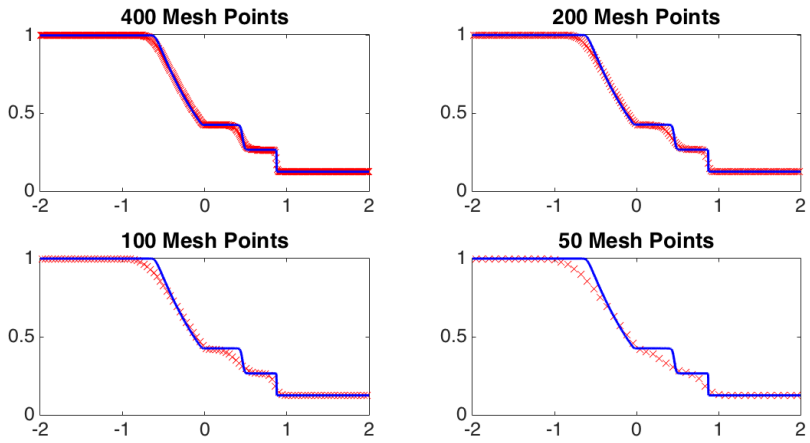

Figure 3.7 – Approximate ensemble mean at time $t = 0.5$ with perturbations $\alpha = \beta = 0.05$ and different mesh widths.

We denote by $\bar{u}^{\Delta x}_{x,\frac{1}{2}}$ the Monte-Carlo approximation of the mean of the probability measures $\nu^{\Delta x}_{x,\frac{1}{2}}$ for different values of the mesh width. Figure 3.7 displays the ensemble mean of the density and indicates that this mean seems to converge to the unperturbed solution as the number of mesh points is increased. To further verify this convergence, we calculate the $\mathbb{L}^1$-norm of the successive differences in the ensemble mean across the different mesh widths:

$$\|\bar{u}^{\Delta x}_{x,\frac{1}{2}} - \bar{u}^{\Delta \frac{x}{2}}_{x,\frac{1}{2}}\|_{\mathbb{L}^1(\mathbb{R})}. \tag{3.14}$$

As shown in Figure 3.8, the approximations indeed seem to form a Cauchy sequence and are therefore convergent.

Next, we calculate the Monte-Carlo approximation of the ensemble variance of the probability measures $\nu^{\Delta x}_{x,1}$ for different values of the mesh width. Figure 3.9 displays our results and indicate that the variance also seems to converge to a series of peaks corresponding to the location of the rarefaction wave, the contact discontinuity and the shock wave.

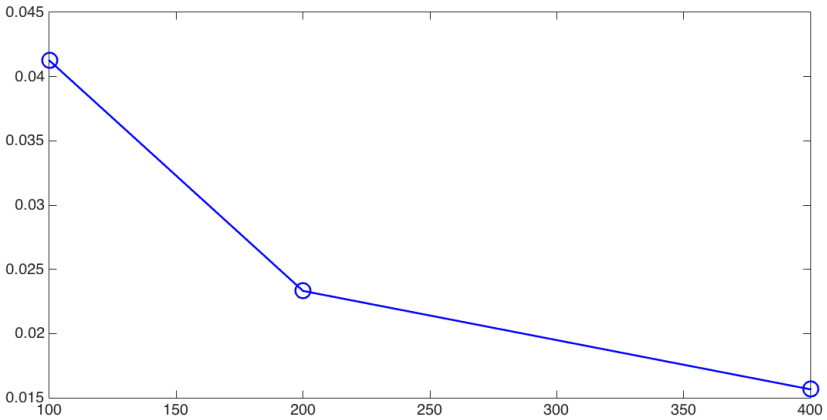

Figure 3.8 – Cauchy Rates for the ensemble mean of the density as a function of the total number of mesh points for perturbation amplitude $\alpha = \beta = 0.05$.

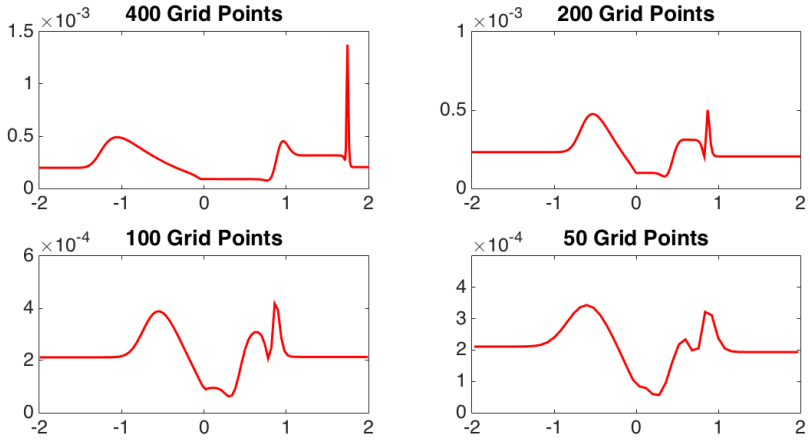

Figure 3.9 – Approximate ensemble variance with perturbations $\alpha = \beta = 0.05$ and different mesh widths.

Finally, we explore the effect of the perturbation amplitude α and β on the convergence of the ensemble mean and variance. We therefore calculate the Monte-Carlo approximation of the ensemble mean, denoted by $\bar{u}^{\Delta x}_{x,\frac{1}{2}}$ of the probability measures $\nu^{\Delta x}_{x,\frac{1}{2}}$ for different values of the perturbation $\alpha = \beta$. Figure 3.10 displays our results and indicates once again that the ensemble mean of the density seems to converge to the unperturbed solution as $\alpha, \beta \to 0$. Figure 3.11 indicates that the $\mathbb{L}^1$-norm of the successive differences in the ensemble approximations indeed seem to form a Cauchy sequence and are therefore convergent.

In addition, figure (3.12) displays the Monte-Carlo approximation of the

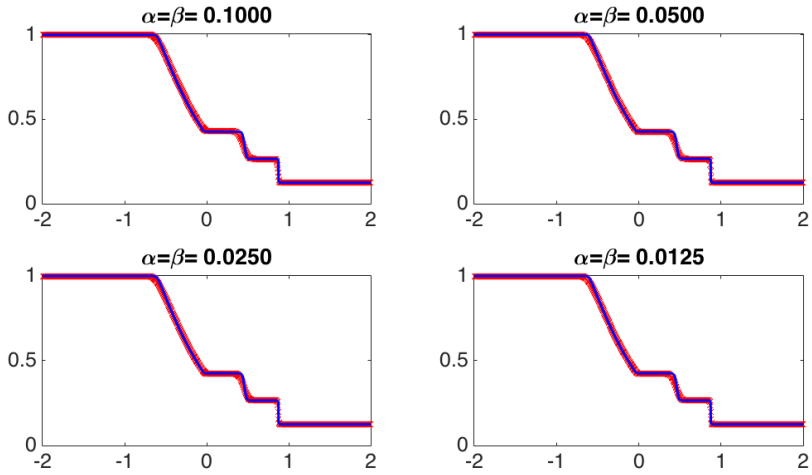

Figure 3.10 – Approximate ensemble mean at time $t = 0.5$ with 400 mesh points and different values of the perturbation amplitude $\alpha = \beta$.

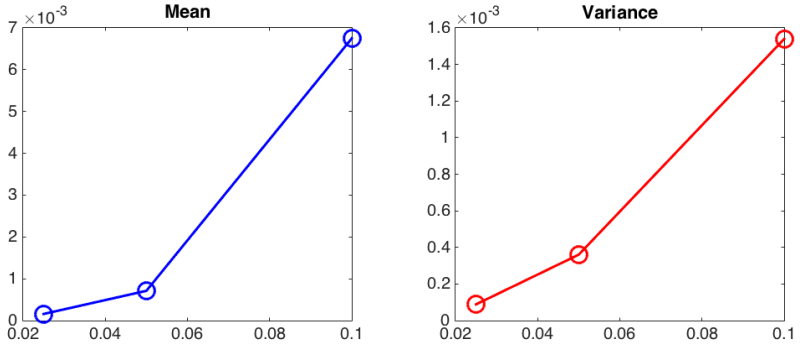

Figure 3.11 – Cauchy Rates for the ensemble mean and ensemble variance of the density as a function of the perturbation amplitude $\alpha = \beta$ with 400 mesh points.

ensemble variance of the probability measures $\nu_{x,1}^{\Delta x}$ for decreasing values of the perturbation amplitude. The results indicate that the variance also seems to vanish as $\alpha, \beta \to 0$.

These two examples serve to demonstrate that our numerical results agree with the theoretical results presented in the previous sections. Of course, the consequence of this fact is not in itself of much importance since state-of-the-art schemes such as the TECNO schemes presented by U. S. Fjordholm et al [19] can always be used to solve these Cauchy problems with much greater accuracy and much less computational power.

The utility of the EMV solution framework and the algorithm presented in Section (3.2) however, lies in the fact that the ensemble mean, variance and other statistical quantities of interest can converge under increasing mesh width resolution and may remain stable under decreasing perturbation am-

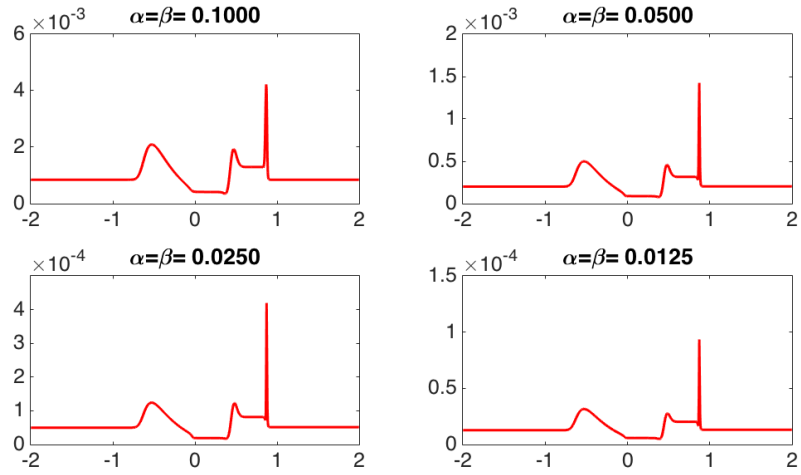

Figure 3.12 – Approximate ensemble variance at time $t = 0.5$ with 400 mesh points and different values of the perturbation amplitude $\alpha = \beta$.

plitudes even in cases where conventional schemes fail to produce numerical approximations that converge to an entropy solution. It is precisely this property of approximate EMV solutions that was utilised by U. S. Fjordholm et al [18] and it is precisely this property that we hope to take advantage of when performing numerical simulations to explore the Carbuncle phenomenon.

Chapter 4

The Carbuncle Phenomenon in 1D

4.1 Numerical Experiments in 1D

The following numerical example was proposed by K. Kitamura, P. Roe and F. Ismail [28]. While this is an extremely simplified version of the classical Carbuncle phenomenon in 2D, it nevertheless serves to illustrate that state-of-the-art entropy stable numerical schemes can exhibit numerical instability even in such a simple situation.

We consider the one-dimensional Euler equations (3.10) in the case of a steady shock and explore the effects of the shock location on the computational grid and the free-stream Mach number on the numerical solution. The computational domain consists of a mesh of uniform width, divided into exactly 50 cells with piecewise constant initial conditions for the left ($L : i \leq 12$) and right ($R : i \geq 14$) states:

$$\mathbf{U}_L = \begin{bmatrix} 1 \\ 1 \\ \frac{1}{\gamma(\gamma-1){M_0}^2} + \frac{1}{2} \end{bmatrix}, \qquad \mathbf{U}_R = \begin{bmatrix} f(M_0) \\ 1 \\ \frac{g(M_0)}{\gamma(\gamma-1){M_0}^2} + \frac{1}{2f(M_0)} \end{bmatrix} \tag{4.1}$$

where

$$f(M_0) = \left(\frac{2}{(\gamma+1){M_0}^2} + \frac{\gamma-1}{\gamma+1} \right)^{-1}, \qquad g(M_0) = \frac{2\gamma {M_0}^2}{\gamma+1} - \frac{\gamma-1}{\gamma+1}, \tag{4.2}$$

and it can be checked that the states (5.7) satisfy the Rankine-Hugoniot conditions across the shock.

The internal shock condition ($M : i = 13$) can then be deduced by following the procedure proposed by Chauvat, Moschetta and Gressier [6]. We define

the shock-position parameter $\varepsilon = 0.0, 0.1, \ldots 1$. The intermediate state ($M : i = 13$) that lies on the Hugoniot curve connecting $\mathbf{U}_L$ and $\mathbf{U}_R$ is then given by

$$\begin{aligned} \rho_M &= \rho_L + \varepsilon(\rho_R - \rho_L), \\ u_M &= u_L + \varepsilon_u(u_R - u_L), \\ p_M &= p_L + \varepsilon_p(p_R - p_L) \end{aligned} \tag{4.3}$$

where

$$\begin{aligned} \varepsilon_u &= 1 - (1-\varepsilon)\Big(1 + \varepsilon\frac{M_0^2 - 1}{1 + (\gamma-1)M_0^2/2}\Big)^{-1/2}\Big(1 + \varepsilon\frac{M_0^2 - 1}{1 - 2\gamma M_0^2/(\gamma-1)}\Big)^{-1/2}, \\ \varepsilon_p &= \varepsilon\Big(1 + (1-\varepsilon)\frac{\gamma+1}{\gamma-1}\frac{M_0^2 - 1}{M_0^2}\Big)^{-1/2}. \end{aligned} \tag{4.4}$$

We employ a fixed mass flux boundary condition at the outflow boundary:

$$(\rho v)_{i_{max}+1} = (\rho v)_0 = 1 \tag{4.5}$$

and we prescribe zero gradient boundary conditions for the remaining variables at the outflow boundary and free-stream boundary conditions at the inflow boundary. This choice of outflow boundary conditions might seem non-intuitive but it ensures that the total mass in the computational domain remains constant and therefore the shock position is fixed. Furthermore, these boundary conditions also make sense from a physical point of view since they try to capture the situation of a steady shock sitting in front of a wall. Using transparent boundary conditions at the outflow is more difficult to justify from a physical perspective and results in any numerical instability essentially flowing through the outflow boundary. The resulting simulations are therefore neither particularly useful nor interesting.

For the purpose of this experiment the free-stream Mach number is chosen in the range $2 \leq M_0 \leq 20$. Our goal is to examine the stability of the numerical schemes for different values of the shock-position parameter ε and the free-stream Mach number M_0. We employ a variety of first-order finite volume schemes including schemes that are widely accepted to be stable shock-capturing methods. We use the original (linearised) Roe solver (see, e.g, [32]), the Rusanov or local Lax-Friedrichs scheme (see, e.g., [32]), an entropy stable scheme with Roe-type diffusion $(RoeES)$ (see, e.g., [17]), an entropy stable scheme with Rusanov-type diffusion $(RusanovES)(see, e.g., [17])$ and the entropy consistent Roe scheme $(RoeEC1)$ introduced by K. Kitamura, P. Roe and F. Ismail (see, e.g.[28]) with diffusion parameter $\alpha = 0.2$ and $\alpha = 0.8$. We categorise our numerical schemes in the following way

- We declare a numerical scheme to be $1D$ **stable** if the approximate solution produced by the scheme converges to a steady state shock solution for all values of ε and M_0.
- We declare a numerical scheme to be $1D$ **unstable** if the approximate solution produced by the scheme does not converge to a steady state shock solution and instead forms a limit cycle for some value of ε and M_0.

All computations were performed using a CFL number of $1/3$, which resulted in a mesh-width to time-step ratio $\lambda \approx 0.25$ and the simulations were run for a minimum of $40,000$ time steps.

4.1.1 Results of the Numerical Experiments

Our results indicate that the stability of the shock depends on the numerical scheme employed and the parameters ε and M_0. Thus for example, the Roe scheme seems to be stable for some choices of ε and M_0 and unstable for others while the Rusanov scheme seems to be stable for all values of ε and M_0. Table 4.1 displays the results of the stability tests for the different schemes we have tested.

Scheme	$1D$ Stability
Roe	Unstable
RoeEC1 $(\alpha = 0.2)$	Unstable
RoeES	Stable
RoeEC1 $(\alpha = 0.8)$	Stable
Rusanov	Stable
RusanovES	Stable

Table 4.1 – Summary of the $1D$ stability of different numerical schemes.

Scheme	ε	M_0
Roe	0.2	20
RoeEC1 $(\alpha = 0.2)$	0.5	20
RoeES	0.4	20
RoeEC1 $(\alpha = 0.8)$	0.4	15
Rusanov	0.7	20
RusanovES	0.6	20

Table 4.2 – Concrete choice of the parameters ε and M_0 for the purpose of our experiments.

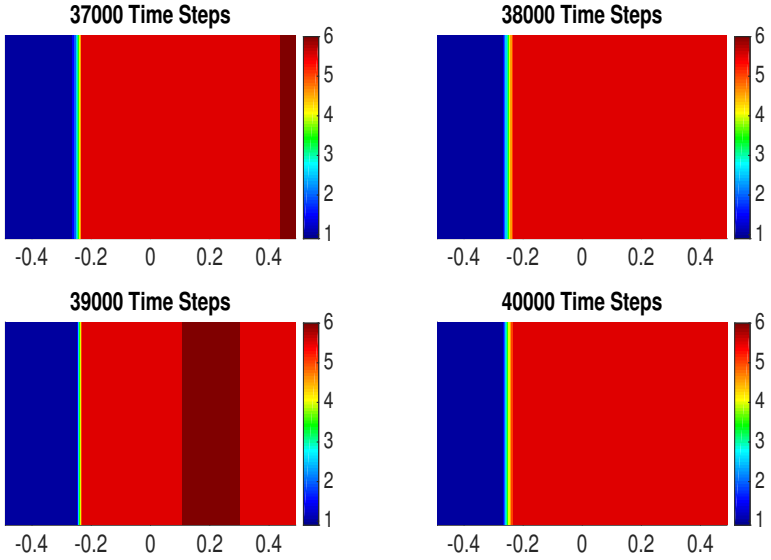

Figure 4.1 – Unstable. Isodensity contour plots of the original Roe scheme for $\varepsilon = 0.2, M_0 = 20$ at 37000, 38000, 39000 and 40000 time steps.

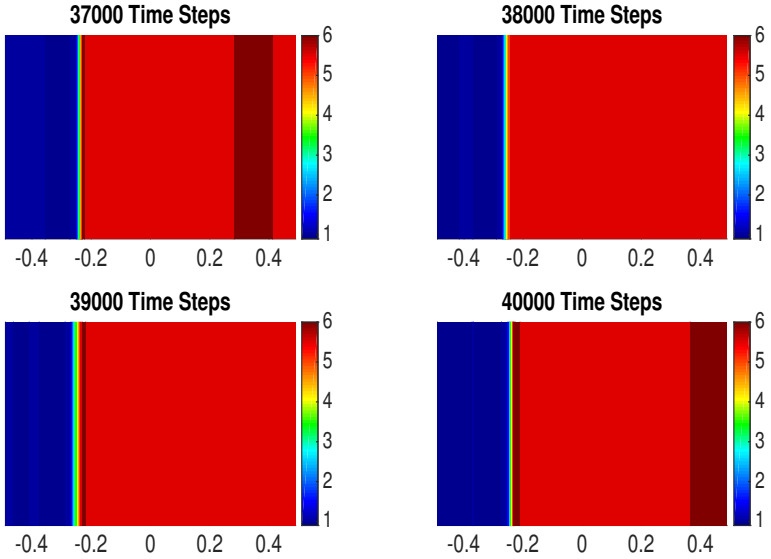

Figure 4.2 – Unstable. Isodensity contour plots of the *RoeEC*1 scheme for $\varepsilon = 0.5, M_0 = 20$ at 37000, 38000, 39000 and 40000 time steps.

Even for this simplified $1D$ test case, we begin to see that entropy stability is neither a necessary nor a sufficient condition for stable shock resolution. Indeed as shown in Figure 4.1 and 4.2, for high Mach number M_0, the original Roe scheme and the entropy stable *RoeEC*1 ($\alpha = 0.2$) are both unable to resolve the steady shock in a stable manner and instead produced numerical

approximations which form a limit cycle.

Furthermore, as shown in Figure 4.3 the shock solution produced by the *RoeES* scheme, while stable, is not monotone and contains a significant spurious overshoot.

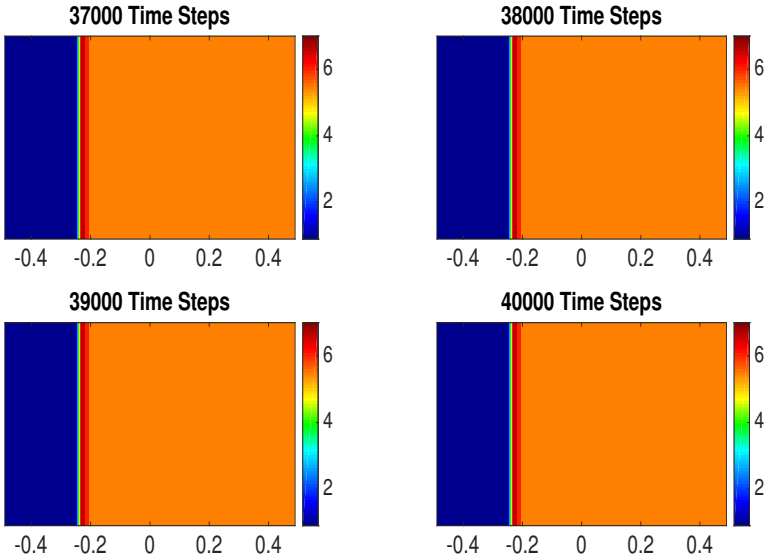

Figure 4.3 – Stable. Isodensity contour plots of the *RoeES* scheme for $\varepsilon = 0.4$, $M_0 = 20$ at 37000, 38000, 39000 and 40000 time steps.

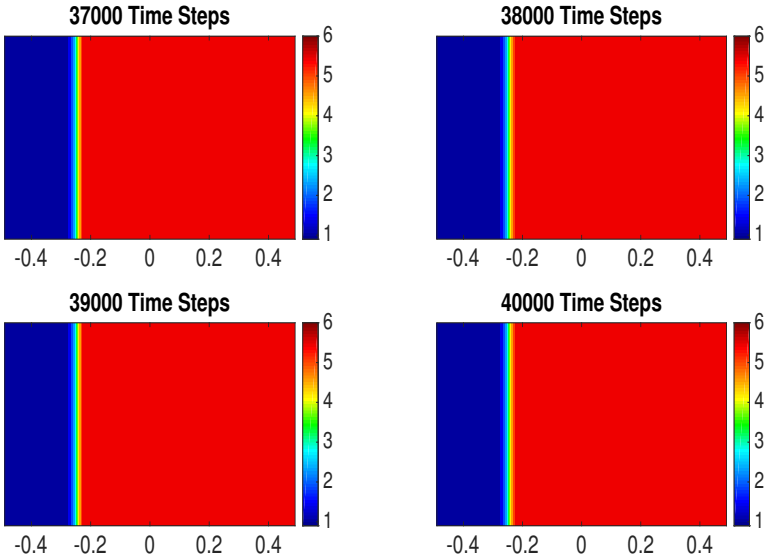

Figure 4.4 – Stable. Isodensity contour plots of the *RoeEC*1 ($\alpha = 0.8$) scheme for $\varepsilon = 0.4$, $M_0 = 15$ at 37000, 38000, 39000 and 40000 time steps.

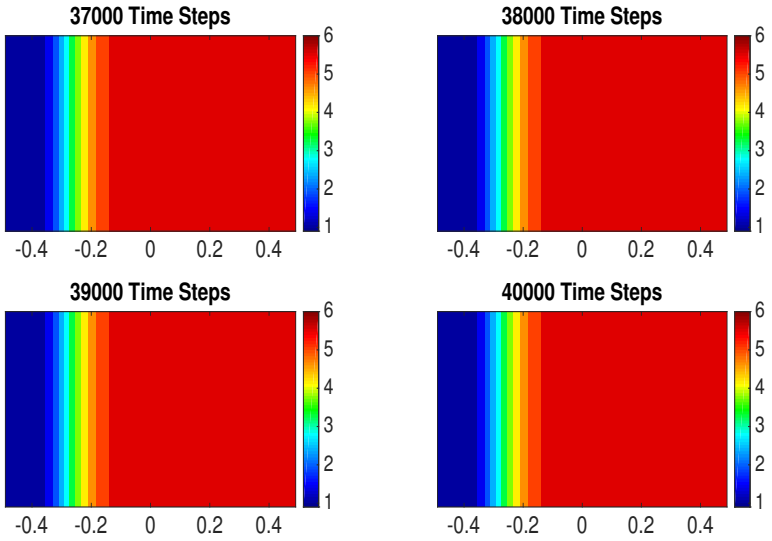

Figure 4.5 – Stable. Isodensity contour plots of the Rusanov scheme for $\varepsilon = 0.7, M_0 = 20$ at 37000, 38000, 39000 and 40000 time steps.

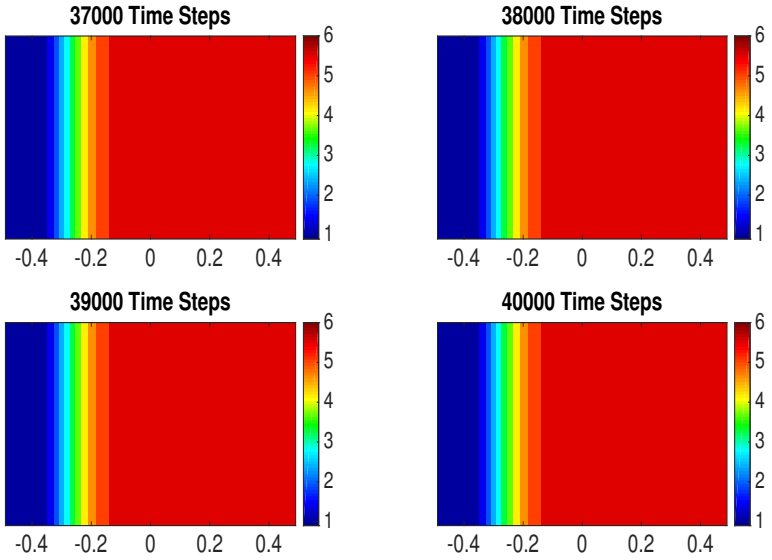

Figure 4.6 – Stable. Isodensity contour plots of the *RusanovES* scheme for $\varepsilon = 0.6, M_0 = 20$ at 37000, 38000, 39000 and 40000 time steps.

On the other hand as shown in Figure 4.4, the *RoeEC*1 ($\alpha = 0.8$) scheme successfully resolve the steady shock in a minimally diffusive manner. The Rusanov scheme and the *RusanovES* scheme also produce stable shock solutions but these are significantly 'smeared out'. Figures 4.1-4.6 display isodensity contour plots of each of the schemes we have tested for a specific

choice of the shock position parameter ε and the free-stream Mach number M_0 as given in Table 4.2.

A comprehensive breakdown of the results of this numerical experiment for all possible values of M_0 and ε can be found in [28].

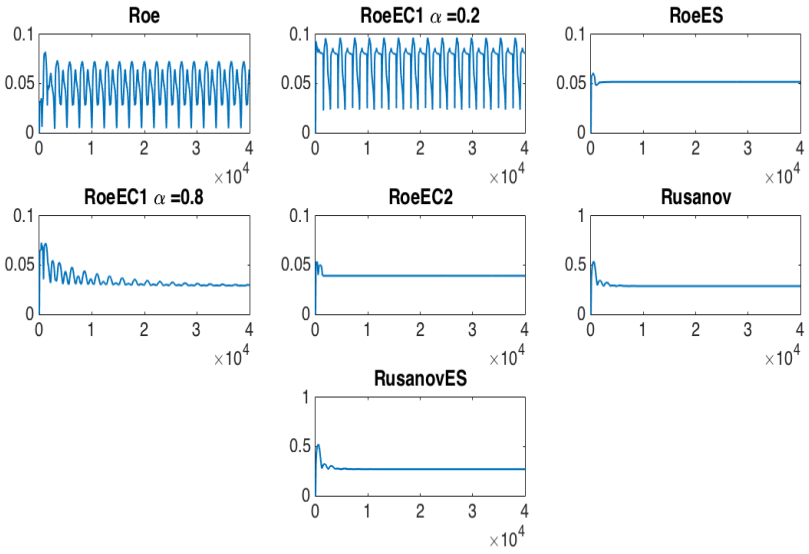

Figure 4.7 – The error $\|\rho_0 - \rho^n_{\Delta x}\|_{L^1}$ vs. the number of time steps n for each numerical scheme for the specific choice of ε and M_0 listed in Table 4.2.

A clearer picture can be obtained by plotting error residuals for each of the experiments that we have performed. Figure 4.7 displays the $L1$-norm of the difference between the initial condition and the approximate solution density at each time step for each of the numerical schemes that we have used. Clearly, both the original Roe scheme and the $RoeEC1$ $(\alpha = 0.2)$ scheme are unable to resolve the shock in a stable manner and instead lead to approximate solutions which seem to form a limit cycle. On the other hand the error plots for the remaining schemes all converge to a fixed value indicating convergence of the solution. In addition, Figure 4.8 displays the $L1$-norm of the difference between successive solution approximations of the density at each time step for each of the numerical schemes. This constitutes further evidence that the Roe scheme and the $RoeEC1$ $(\alpha = 0.2)$ scheme are unable to produce solution approximations that converge while the errors for the remaining schemes quickly decay to zero.

As mentioned previously the specific choice of a fixed mass flux condition at the outflow boundary is necessary to obtain this behaviour. As displayed in Figure 4.9, the use of transparent outflow boundary conditions removes the numerical instability and results in stable shock resolution.

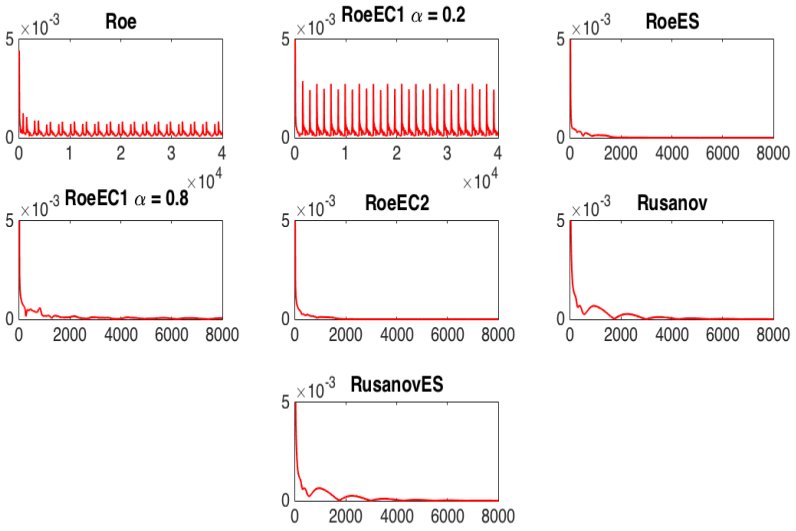

Figure 4.8 – The error $\|\rho^{n+1}_{\Delta x} - \rho^{n}_{\Delta x}\|_{L^1}$ vs. the number of time steps n for each numerical scheme for the specific choice of ε and M_0 listed in Table 4.2.

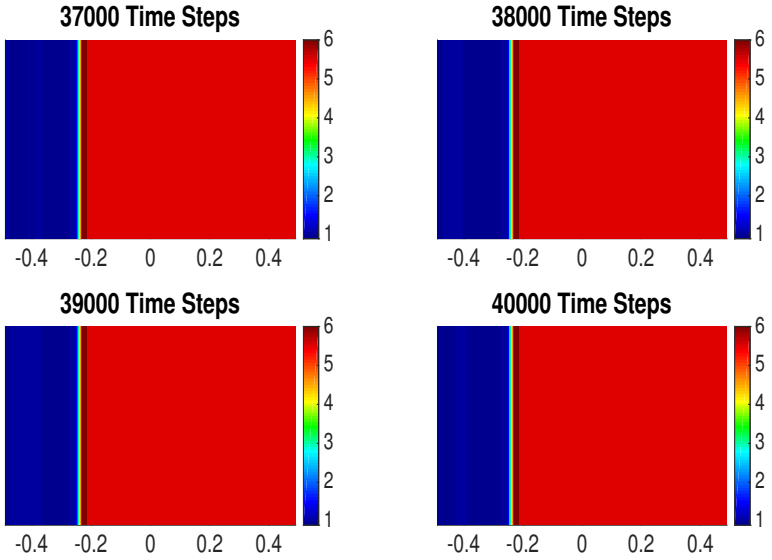

Figure 4.9 – **Stable**. Isodensity contour plots of the *RoeEC*1 ($\alpha = 0.2$) scheme with *transparent* outflow boundary conditions for $\varepsilon = 0.5$, $M_0 = 20$ at 37000, 38000, 39000 and 40000 time steps.

In particular these numerical experiments illustrate that even entropy stable schemes can exhibit the Carbuncle phenomenon in $1D$. In view of this numerical evidence, the next logical task is to determine if there is an underlying problem with the numerical methods we are using, which leads to the numerical instability or if the framework of entropy solutions itself is deficient. In case of the latter, we would expect to obtain stability and convergence results for statistical quantities associated with the corresponding EMV solutions. In order to answer this question therefore, we resort to the framework of Entropy measure valued solutions and apply the algorithm presented in Section 3.2 to attempt to resolve this numerical instability.

4.1.2 Numerical Experiments involving the MV Cauchy Problem

Experiment 1

We first consider the corresponding MV Cauchy problem involving the Euler equations (3.10) by perturbing the initial conditions (5.7).

Let $(\Omega, \mathcal{F}, \mathbb{P})$ be a probability space, let $X\colon \Omega \to [-0.5, 0.5]$ be a uniformly distributed random variable, let $\delta \in [0, 1]$ be a constant and consider the same Cauchy problem introduced in Section (4.1) but with perturbed shock position parameter given by

$$\tilde{\varepsilon} = \varepsilon + \delta X. \tag{4.6}$$

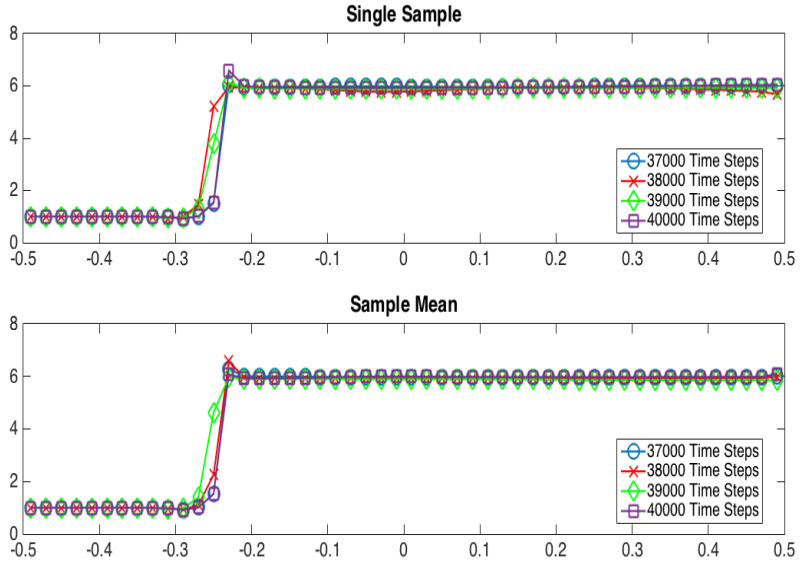

Figure 4.10 – Density plots of the ensemble mean and original solution using $RoEC1$ scheme for $\varepsilon = 0.5, M_0 = 20$ at 37000, 38000, 39000 and 40000 time steps.

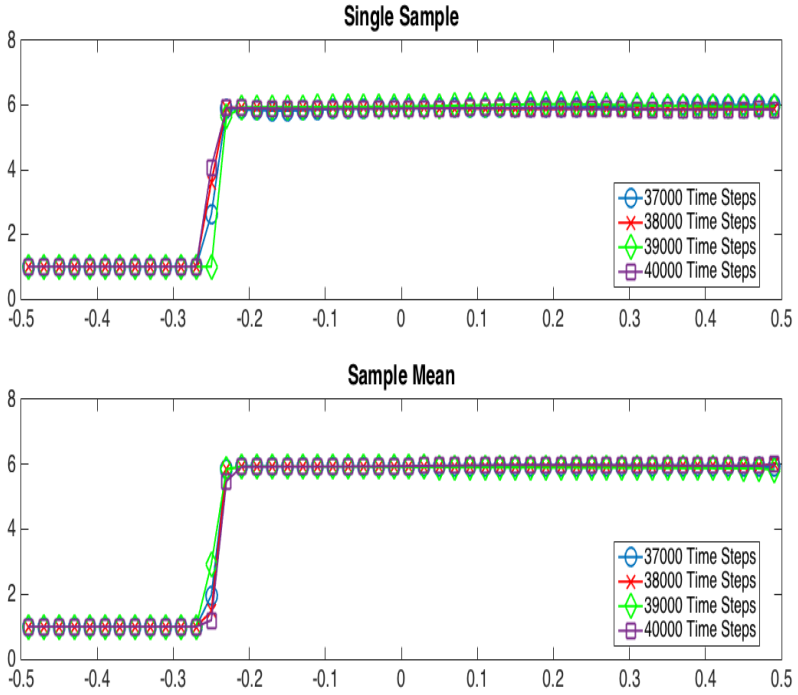

Figure 4.11 – Density plots of the ensemble mean and original solution using Roe scheme for $\varepsilon = 0.2$, $M_0 = 20$ at 37000, 38000, 39000 and 40000 time steps.

The remaining set up including the initial conditions and the boundary conditions are left unchanged. We use Monte-Carlo simulations to estimate the ensemble mean and variance of the approximate measure valued solutions to the associated MV Cauchy problem and analyse the convergence of these statistical quantities. Based on our results in Section 4.1 we are only interested in the $1D$ unstable schemes i.e. the original Roe scheme and the entropy consistent $RoeEC1$ scheme. As a concrete test case we consider $\delta = 0.2,\ \varepsilon = 0.2,\ M = 20$ for the Roe scheme and $\delta = 0.2,\ \varepsilon = 0.5,\ M = 20$ for the $RoeEC1$ scheme. All results are computed using 400 Monte-Carlo iterations.

Figure 4.10, which displays the density plot of the $RoeEC1$ scheme for $\varepsilon = 0.5$ and $M_0 = 20$, clearly indicates that the $RoeEC1$ scheme does not produce approximate solutions that converge to the steady state shock solution. Indeed, even after $30,000$ time steps, the solution has not converged and the shock location continues to oscillate. Unfortunately, Figure 4.10 also indicates that the ensemble mean also does not converge to a steady state shock solution. Indeed the shock location of the ensemble mean of the density also continues to oscillate even after $35,000$ time steps. However, it does appear that the oscillations of the shock position for the ensemble mean are qualitatively

smaller than the oscillations of the shock position for the single sample.

Figure 4.11 displays the density plot of the Roe scheme for $\varepsilon = 0.2$ and $M_0 = 20$ and the ensemble mean of the density for the corresponding MV Cauchy problem. Once again we observe that the Roe scheme does not produce approximate solutions that converge to the steady state shock solution. Furthermore, the ensemble mean also does not converge to a steady state shock solution. The shock location of the ensemble mean of the density continues to oscillate well after $30,000$ time steps. Interestingly Figure 4.11 again indicates that the oscillations of the shock position for the ensemble mean are qualitatively smaller than the oscillations of the shock position for the single sample.

We also analyse the ensemble variance of the density for both test cases. Figure 4.12 displays the ensemble variance the density for both the *RoeEC*1 scheme and the Roe scheme. As expected while the variance does consist of a sharp spike at the shock location for both test cases, the magnitude of the spike oscillates considerably even after $35,000$ time steps. It is therefore reasonable to conclude that the ensemble variance also does not converge to a steady state.

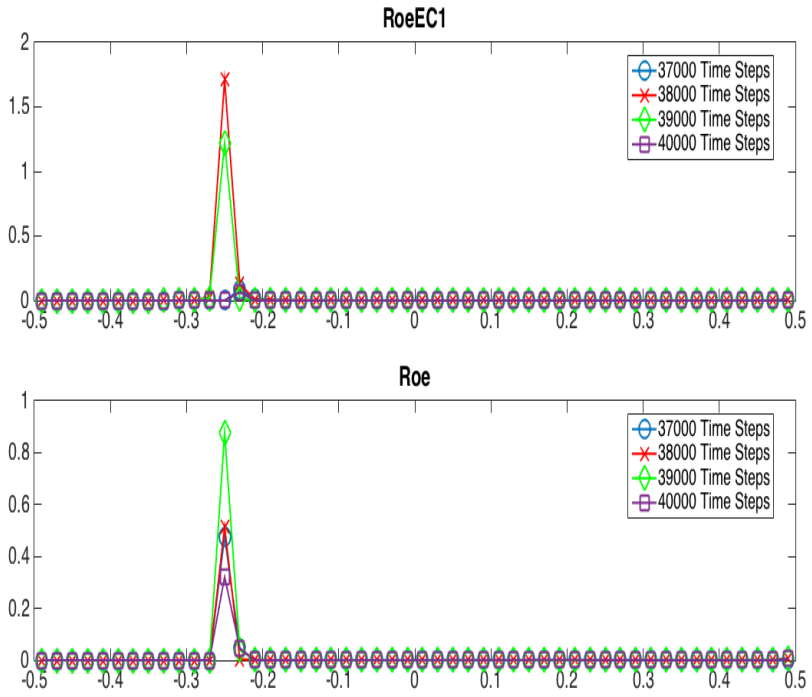

Figure 4.12 – Ensemble variance of the entropy measure valued solution for the *RoeEC*1 scheme and the original Roe scheme.

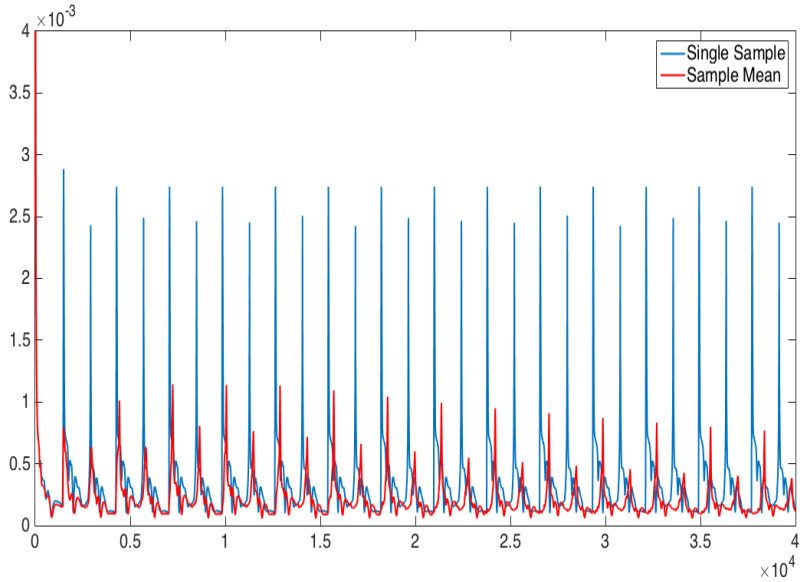

Figure 4.13 – The error $\|\rho_{\Delta x}^{n+1} - \rho_{\Delta x}^{n}\|_{L^1}$ vs. the number of time steps for the *RoeEC*1 scheme.

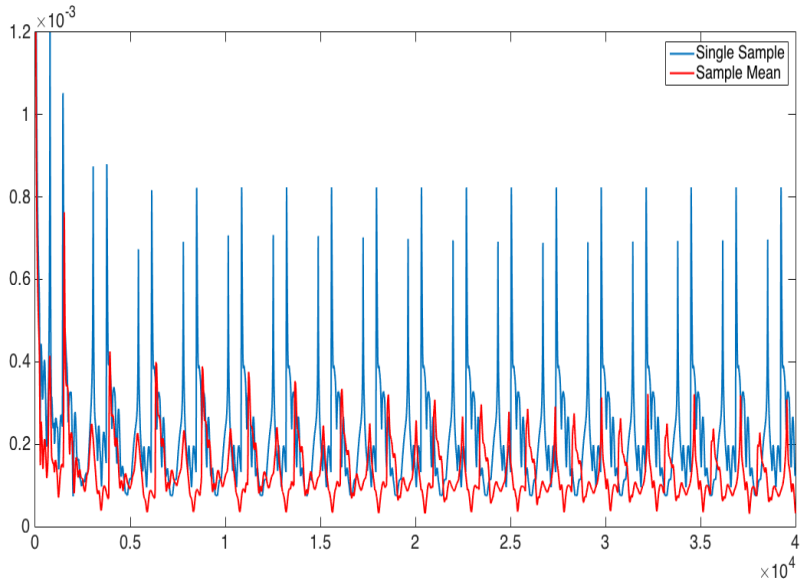

Figure 4.14 – The error $\|\rho_{\Delta x}^{n+1} - \rho_{\Delta x}^{n}\|_{L^1}$ vs. the number of time steps for the original Roe scheme.

The analysis of the error residuals for the two test cases confirms our conclusions. Figure 4.13 displays the $L1$-norm of the difference between successive solution approximations of the density at each time step for the $RoeEC1$ scheme. Two important points can immediately be inferred from the plot. First, that the error for the ensemble mean of the density does not decay immediately to zero although there is a visible trend towards a slow decay and second, that the error residual of the ensemble mean is smaller than the error residual of the original solution. Figure 4.14, which displays the $L1$-norm of the difference between successive solution approximations of the density at each time step for the original Roe scheme indicates a similar result.

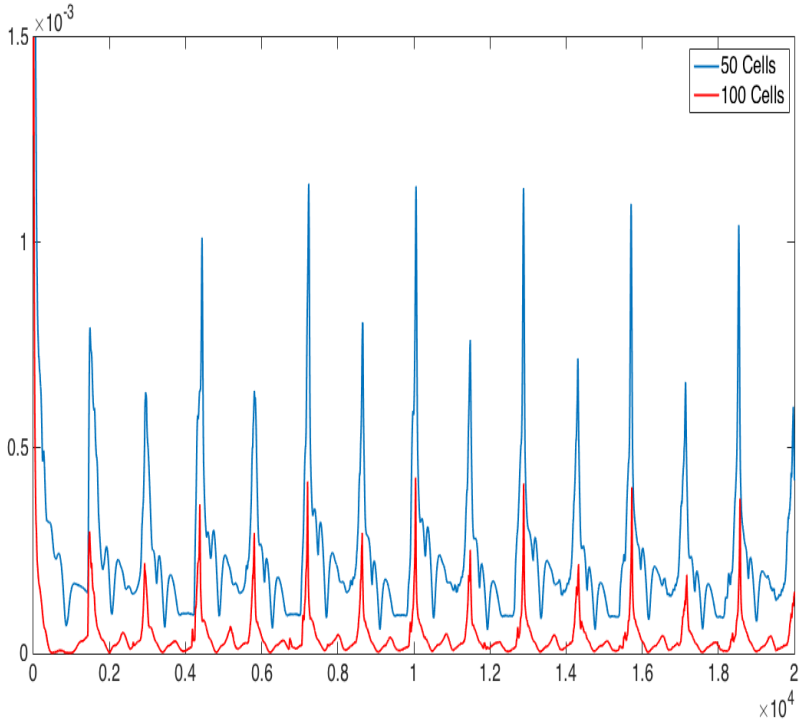

Figure 4.15 – The error $\|\rho_{\Delta x}^{n+1} - \rho_{\Delta x}^{n}\|_{L^1}$ vs. the number of time steps for both 100 cells and 50 cells using the $RoeEC1$ scheme.

We next explore the effects of increasing the mesh width refinement on the stability and convergence of the ensemble mean and variance for the test case involving the $RoeEC1$ scheme. In particular, we repeat the same experiment with a computational domain consisting of 100 cells i.e. with mesh width exactly halved. Figure 4.15 displays the $L1$-norm of the difference between successive solution approximations of the ensemble mean of the density at each time step for both 100 cells and 50 cells. Clearly, the er-

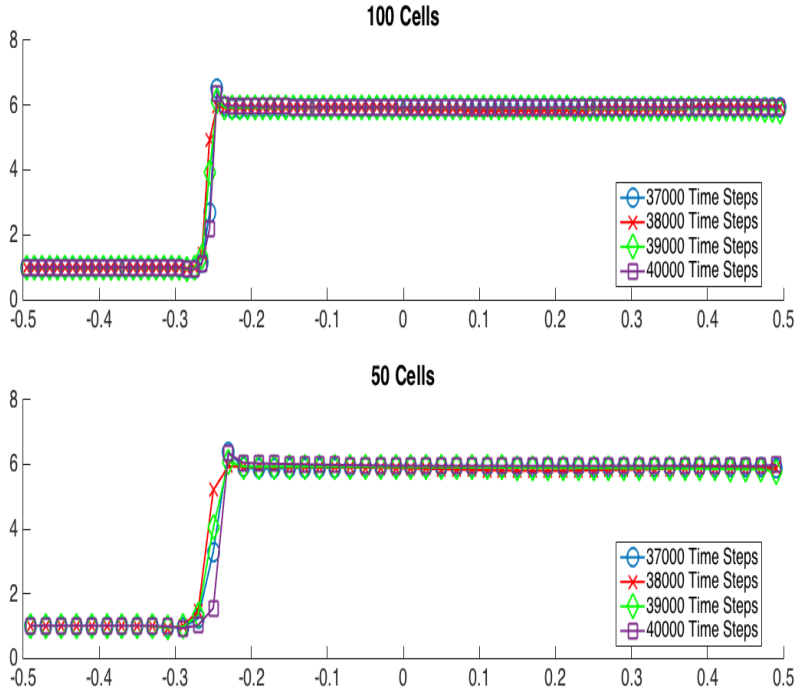

Figure 4.16 – Density plots of the ensemble mean using the *RoeEC*1 scheme for both 100 cells and 50 cells at 37000, 38000, 39000 and 40000 time steps.

ror residual for 100 cells is smaller than the error residual for 50 cells and this seems to indicate that ensemble mean of the density may converge to a steady state shock solution as the mesh width is refined. However, it is important to note that error residual still oscillates and does not immediately decay to zero. It is not immediately clear therefore, if this decrease in the error residual is due to the fact that the shock is more sharply resolved and therefore the oscillation in shock position leads to a smaller error residual or if this decrease in the error residual is due to a genuine convergence of the ensemble mean to a steady state solution as the mesh width is refined.

Figure 4.16 displays the ensemble mean of the density for both 100 and 50 cells. As expected the shock is more sharply resolved in the case of 100 cells but once again, it is clear that the shock position is not stable and instead oscillates even after $35,000$ time steps.

A similar result is obtained for the ensemble variance of the density. Figure 4.17 displays the ensemble variance for both 100 and 50 cells. Once again we observe that while the spike in the variance at the shock location is sharper for the case of 100 cells, there is nonetheless no convergence of the variance to a steady state. It is thus reasonable to conclude that while the error

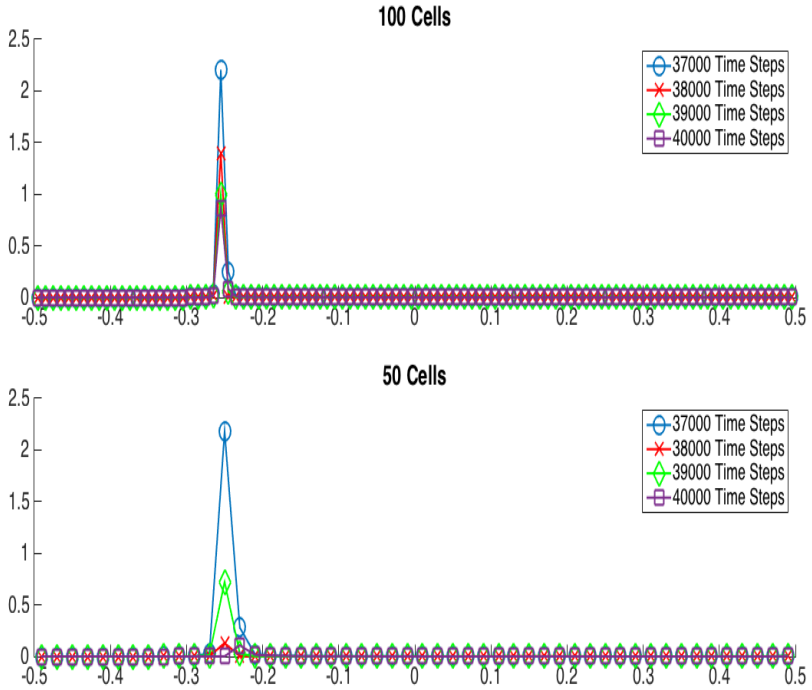

Figure 4.17 – Ensemble variance of the entropy measure valued solution for both 100 cells and 50 cells using the *RoeEC*1 scheme.

residual does indeed decrease as the mesh is refined, both the ensemble mean and the ensemble variance do not converge to a steady state solution. In view of theoretical results (see, e.g., [18]), this is an important indication that the $1D$ numerical instability we are observing has, at least partially, numerical origin.

Finally we explore the effects of decreasing the perturbation parameter δ on the stability of the ensemble mean and variance of the measure valued entropy solution. Theoretical results once again imply (see, e.g., [18]) that decreasing the parameter δ would lead to convergence of the ensemble mean and variance of the approximate measure entropy valued solutions. Conversely, if the mean and variance are not stable under decreasing values of the perturbation parameter δ, this would be another important indication that the Carbuncle phenomenon in $1D$ has a numerical origin.

Figure 4.18 displays the $L1$-norm of the difference between successive solution approximations of the ensemble mean of the density at each time step for different values of the parameter δ. Clearly, the error residual does not decrease as the value of δ is decreased. Indeed the error residual actually seems to *increase* as the value of δ is decreased and this implies that the en-

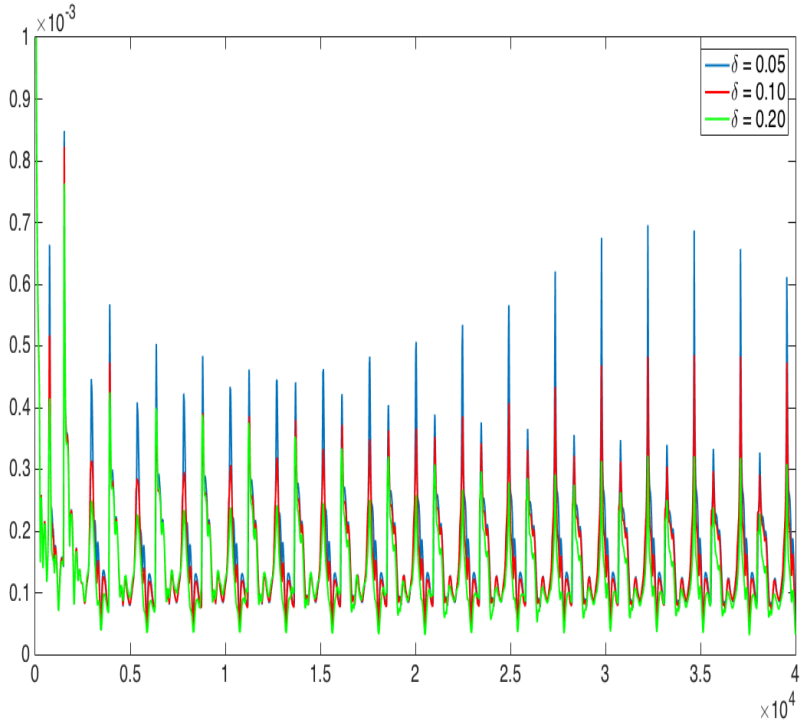

Figure 4.18 – The error $\|\rho^{n+1}_{\Delta x} - \rho^{n}_{\Delta x}\|_{L^1}$ vs. the number of time steps for different values of the parameter δ using the Roe scheme.

semble mean is not stable under decreasing amplitudes of perturbation. We also remark that the error residuals for all values of δ are characterised by large oscillations which further implies that in each case the ensemble mean still suffers from numerical instability and does not converge to a steady state shock solution.

Plots of the ensemble mean of the density support our conclusion. Figure 4.19 displays the ensemble mean of the density for different values of δ. We immediately observe two important points. First, for each value of delta the shock position of the mean still suffers from instability and consequently the mean does not converge to a steady state shock solution even after $35,000$ time steps. Second, as the value of δ is decreased there is little qualitative decrease in the amplitude of oscillations of the shock position. This reinforces our conclusion that there is no convergence of the ensemble mean of the approximate EMV solution to a steady state as δ is decreased.

A similar result is obtained for the ensemble variance of the density. Figure 4.20 displays the ensemble variance for different values of δ. We observe that while the variance does decrease as expected as the value of δ is decreased, there is nonetheless no convergence of the variance for any value of δ to a

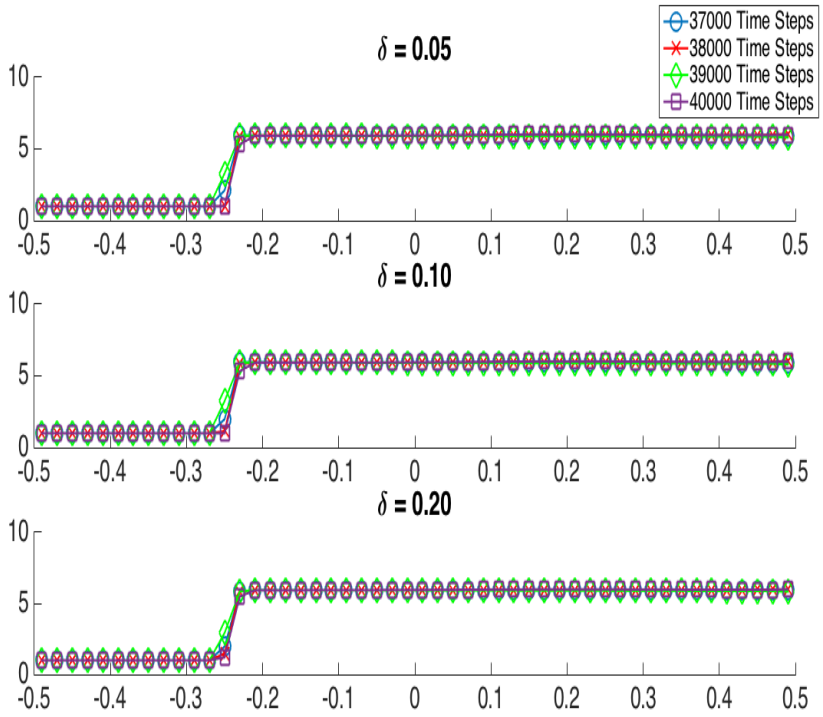

Figure 4.19 – Density plots of the ensemble mean for different values of the parameter δ using the Roe scheme at 37000, 38000, 39000 and 40000 time steps.

steady state even after $35,000$ time steps. It is thus reasonable to conclude that both the ensemble mean and the ensemble variance are not stable under decreasing values of the amplitude of perturbation δ. We therefore feel confident in our conclusion that there is no convergence of the ensemble mean and variance of the density as the value of δ is decreased.

In light of the results of these numerical experiments we feel that the following three conclusions can be drawn:

- The error residual of the ensemble mean of the density of the corresponding measure valued Cauchy problem is smaller than the error residual of the solution to the original Cauchy problem.
- The ensemble mean and variance still suffer from numerical instability and therefore do not converge to a steady state solution even after $30,000$ time steps.
- There does not seem to be any convergence of the ensemble mean and variance either as the mesh width is refined or as the value of δ is decreased.

We feel that this supports the prevalent view in the literature that the origin

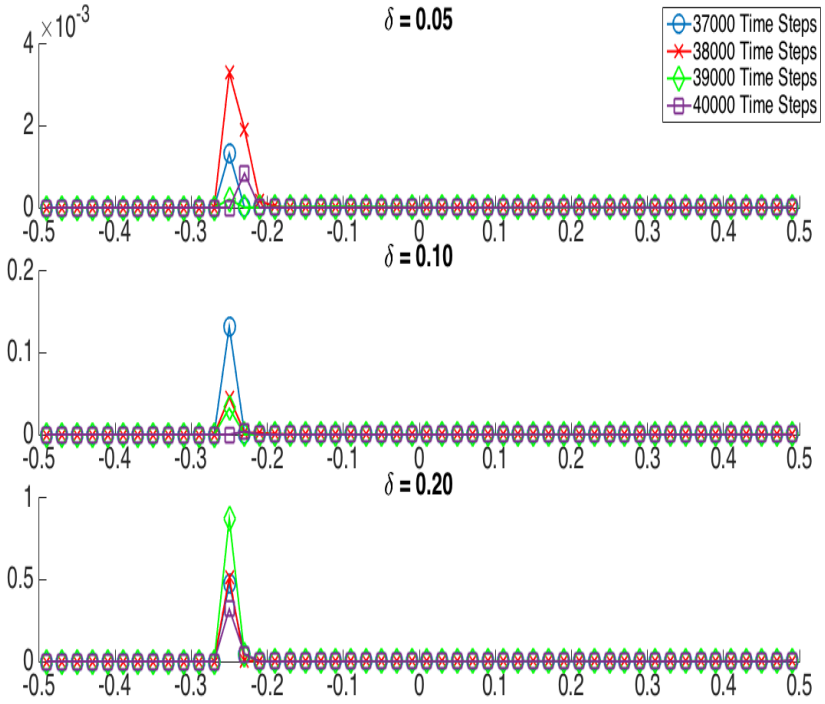

Figure 4.20 – Ensemble variance of the entropy measure valued solution for different values of the parameter δ using the Roe scheme.

of the $1D$ carbuncle phenomenon is numerical in nature to a large degree.

Experiment 2

We now consider the following MV Cauchy problem involving the Euler equations (3.10) by perturbing the initial conditions (5.7).

Let $(\Omega, \mathcal{F}, \mathbb{P})$ be a probability space, let $\Theta\colon \Omega \to [0, 25]$ be a uniformly distributed random variable, let $\kappa \in \mathbb{R}$ be a constant and consider the Cauchy problem (5.7) with initial conditions given by

$$\mathbf{U}_0(x) = \mathbf{U}_L + \mathbf{U}_R \frac{2}{\sqrt{\pi}} \int_0^{\kappa\Theta(x+1/4)} e^{-t^2} dt \tag{4.7}$$

where

$$\mathbf{U}_L = \begin{bmatrix} \dfrac{1+f(M_0)}{2} \\ 1 \\ \dfrac{\frac{1}{\gamma(\gamma-1){M_0}^2} + \frac{1}{2} + \frac{g(M_0)}{\gamma(\gamma-1){M_0}^2} + \frac{1}{2f(M_0)}}{2} \end{bmatrix}, \tag{4.8}$$

$$\mathbf{U}_R = \begin{bmatrix} \frac{f(M_0)-1}{2} \\ 1 \\ \frac{\frac{g(M_0)}{\gamma(\gamma-1){M_0}^2} + \frac{1}{2f(M_0)} - \frac{1}{\gamma(\gamma-1){M_0}^2} + \frac{1}{2}}{2} \end{bmatrix}, \tag{4.9}$$

and the internal shock position ($M : i = 13$) is chosen according to the conditions (4.3).

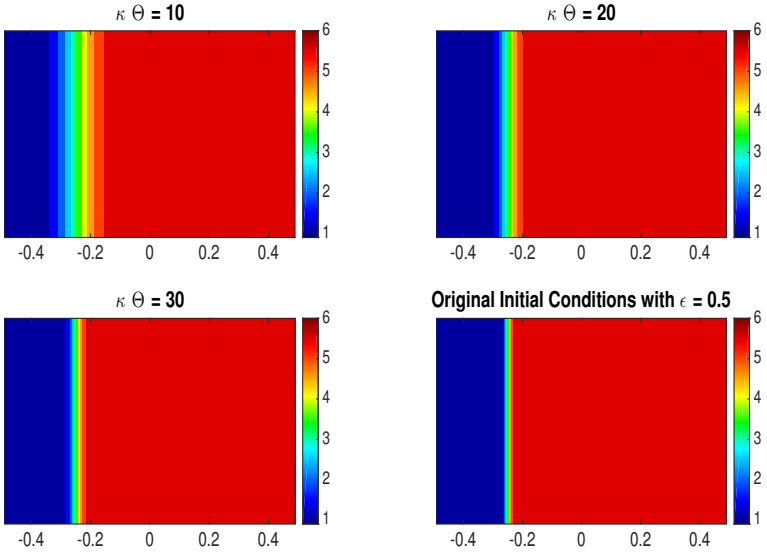

Figure 4.21 – Isodensity contour plots of the initial conditions for different realisations of the random variable Θ along with the original non-random initial conditions.

Figure 4.21 displays the isodensity contour plots for the initial conditions 4.7 for different values of $\kappa \cdot \Theta$ along with the isodensity contour plot for the initial conditions 5.7 with the parameter values $\varepsilon = 0.5, M_0 = 20$. As can be seen, the new initial conditions result in a more 'smeared' version of the shock. Clearly, in the limit $\kappa \to \infty$ the perturbed initial conditions 4.7 approach the original initial conditions 5.7. The remaining set up including the boundary conditions is left unchanged. Once again we use Monte-Carlo simulations to estimate the ensemble mean and variance of the approximate measure valued solutions to the associated MV Cauchy problem. Our aim once again is to analyse the stability and convergence properties of these statistical quantities of interest. In order to be consistent we focus only on the specific parameter values chosen in the Experiment 1. Specifically, we consider the two test cases consisting of $\kappa = 10,\ \varepsilon = 0.2,\ M = 20$ for the Roe

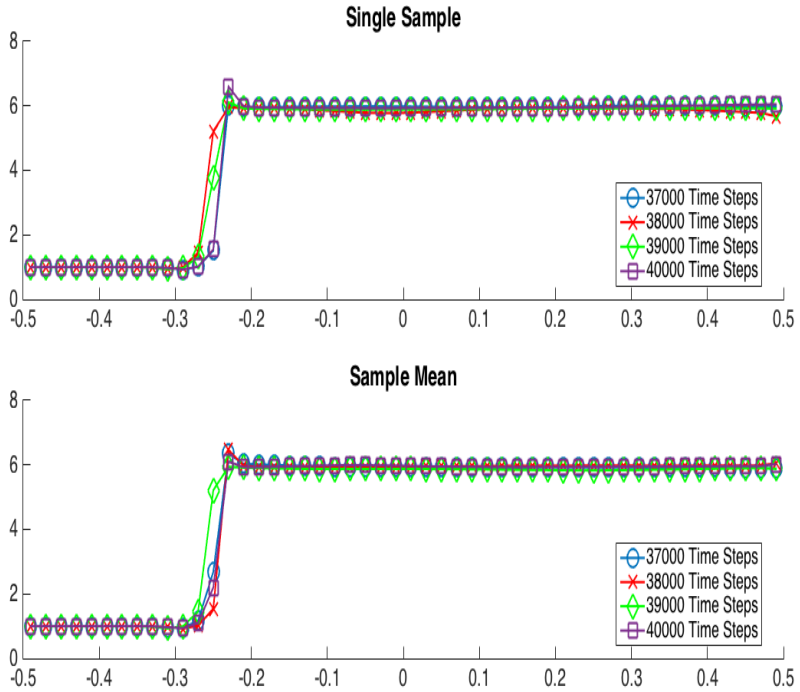

Figure 4.22 – Density plots of the ensemble mean and original solution using the *RoeEC*1 scheme for $\varepsilon = 0.5, M_0 = 20$ at 37000, 38000, 39000 and 40000 time steps.

scheme and $\kappa = 10,\ \varepsilon = 0.5,\ M = 20$ for the *RoeEC*1 scheme. All results are computed using 400 Monte Carlo iterations.

Figure 4.22, which displays the density plot of the *RoeEC*1 scheme for $\varepsilon = 0.5$ and $M_0 = 20$, clearly indicates that the *RoeEC*1 scheme does not produce approximate solutions that converge to the steady state shock solution. Indeed, even after $30,000$ time steps, the solution has not converged and the shock location continues to oscillate. Figure 4.22 also indicates that the ensemble mean also does not converge to a steady state shock solution. Indeed the shock location of the ensemble mean of the density also continues to oscillate even after $35,000$ time steps. Furthermore, it appears that the oscillations of the shock position for the ensemble mean are qualitatively similar to the oscillations of the shock position for the original solution.

Figure 4.23 displays the density plot of the Roe scheme for $\varepsilon = 0.2$ and $M_0 = 20$ and the ensemble mean of the density for the corresponding MV Cauchy. Once again we observe that the Roe scheme does not produce approximate solutions that converge to the steady state shock solution. Interestingly however, the ensemble mean does seem to consist of a much more stable shock location. There is only a slight difference in the intermediate

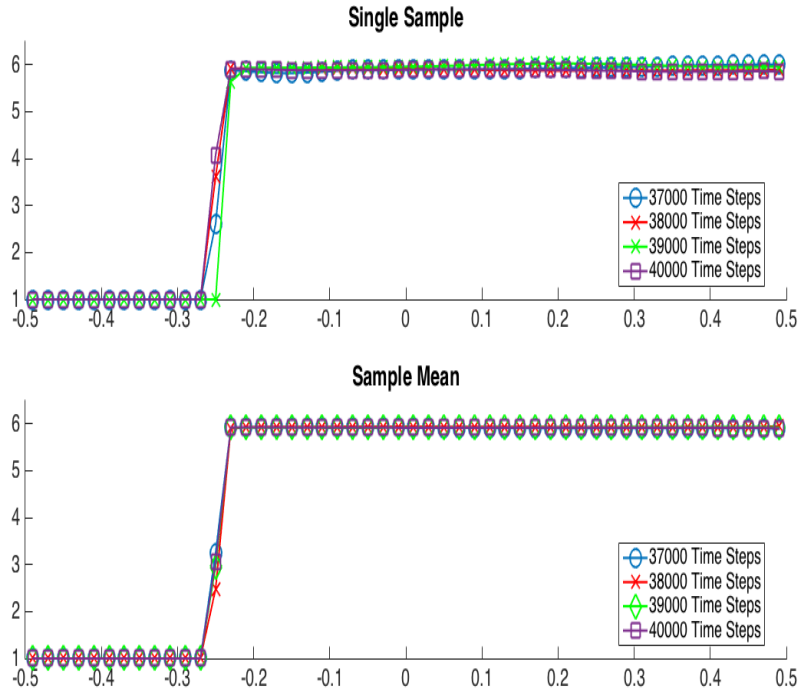

Figure 4.23 – Density plots of the ensemble mean and original solution using the Roe scheme for $\varepsilon = 0.2, M_0 = 20$ at 37000, 38000, 39000 and 40000 time steps.

shock location at $37,000$, $38,000$, $39,000$ and $40,000$ time steps. This is a very interesting result that will be explored in more detail below.

We also analyse the ensemble variance of the density for both test cases. Figure 4.24 displays the ensemble variance of the density for both the *RoeEC*1 scheme and the Roe scheme. While the variance does consist of a sharp spike at the shock location for both cases, the magnitude of the spike oscillates considerably even after $35,000$ time steps. In particular this seems to imply that the ensemble variance does not converge to a steady state for either the *RoeEC*1 scheme or the Roe scheme. This is particularly interesting in light of the results of the ensemble mean for the Roe scheme because it seems to imply that the apparent convergence of the ensemble mean is misleading. In fact it is our contention that the reason the ensemble mean appears to converge in the case of the Roe scheme is because the self-reinforcing nature of the strong shock causes the initial conditions to form a more sharply resolved shock as the system evolves in time and this sharply resolved shock does not suffer from an unstable shock location. This issue will be explored in detail below by considering the effects of increasing the value of κ on the convergence of the ensemble mean and variance for the Roe scheme.

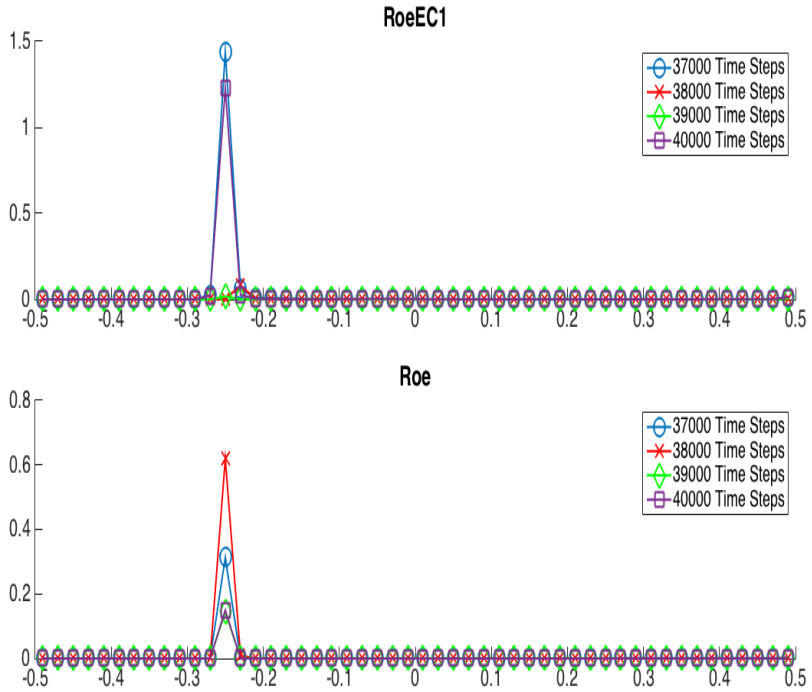

Figure 4.24 – Ensemble variance of the entropy measure valued solution for the *RoeEC*1 scheme and the original Roe scheme.

The analysis of the error residuals for the two test cases confirms our conclusions. Figure 4.25 displays the $L1$-norm of the difference between successive solution approximations of the ensemble mean of the density at each time step for the *RoeEC*1 scheme. Once more, two important points can immediately be inferred from the plot. First, that the error for the ensemble mean of the density does not converge to zero and in contrast with Experiment 1, there is no visible trend towards a slow decay, and second that the error residual of the ensemble mean is smaller than the error residual of the original solution. Figure 4.26, which displays the $L1$-norm of the difference between successive solution approximations of the ensemble mean of the density at each time step for the original *Roe* scheme indicates a qualitatively similar result although in this case the error residual for the ensemble mean is significantly smaller than the error residual for the original solution. This is to be expected in view of the results of the ensemble mean displayed in Figure 4.23.

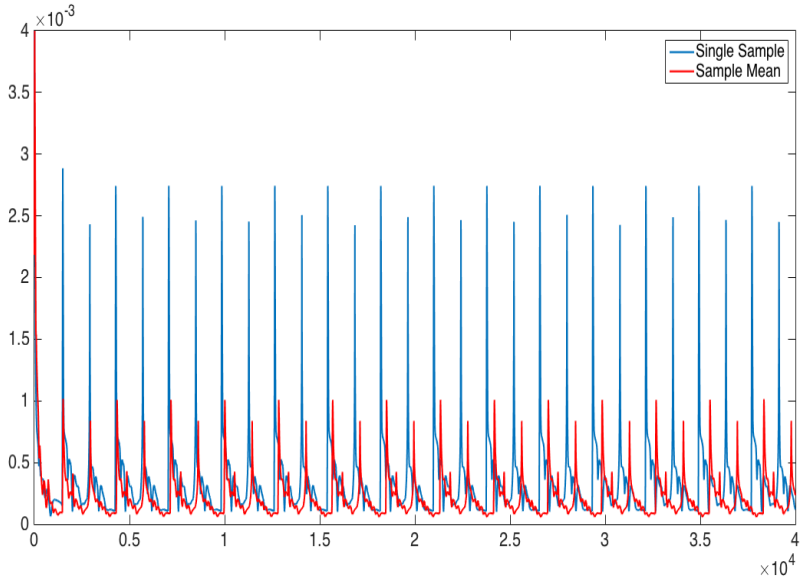

Figure 4.25 – The error $\|\rho_{\Delta x}^{n+1} - \rho_{\Delta x}^{n}\|_{L^1}$ vs. the number of time steps for the *RoeEC*1 scheme.

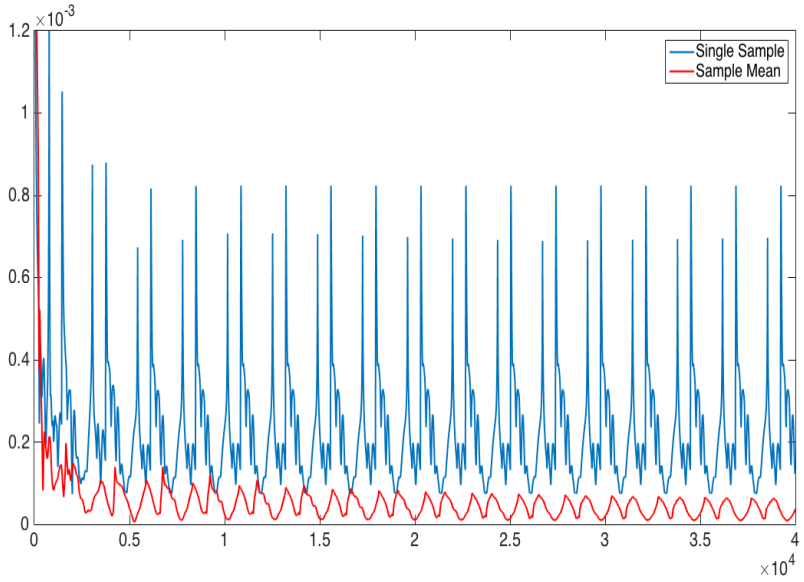

Figure 4.26 – The error $\|\rho_{\Delta x}^{n+1} - \rho_{\Delta x}^{n}\|_{L^1}$ vs. the number of time steps for the Roe scheme.

Similar to Experiment 1, we next explore the effects of increasing the value of the parameter κ for the test case involving the *RoeEC*1 scheme. In particular we repeat the same experiment for $\kappa = 20$. As mentioned previously, theoretical results (see, e.g., [18]) imply that increasing the parameter κ should lead to convergence of the ensemble mean and variance of the approximate

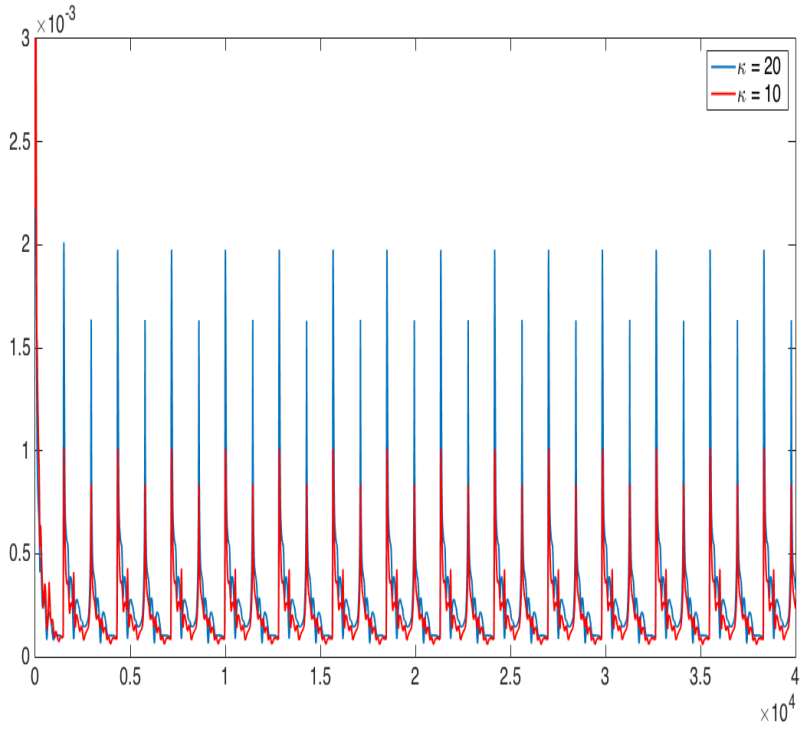

Figure 4.27 – The error $\|\rho_{\Delta x}^{n+1} - \rho_{\Delta x}^{n}\|_{L^1}$ vs. the number of time steps for $\kappa = 10$ and $\kappa = 20$ using the *RoeEC*1 scheme.

entropy measure valued solutions and conversely, if the ensemble mean and variance are not stable under increasing values of the perturbation parameter κ, this would be another strong indication that carbuncle phenomenon in $1D$ has a numerical origin. Figure 4.27 displays the $L1$-norm of the difference between successive solution approximations of the ensemble mean of the density at each time step for both $\kappa = 20$ and $\kappa = 10$. Clearly, the error residual for $\kappa = 20$ is larger than the error residual for $\kappa = 10$ and this implies that the ensemble mean is not stable under increasing values of the parameter κ.

Figure 4.28 displays the ensemble mean of the density for both $\kappa = 20$ and $\kappa = 10$. As expected the shock position continues to suffer from instability and the ensemble mean has not converged for either case even after $30,000$ time steps. Furthermore, there is little qualitative difference in the magnitude of the oscillations of the shock position.

A similar result is obtained for the ensemble variance of the density. Figure 4.29 displays the ensemble variance for both $\kappa = 20$ and $\kappa = 10$. Once again we observe that in both cases there is no convergence of the variance to a steady state. It is thus reasonable to conclude that both the ensemble

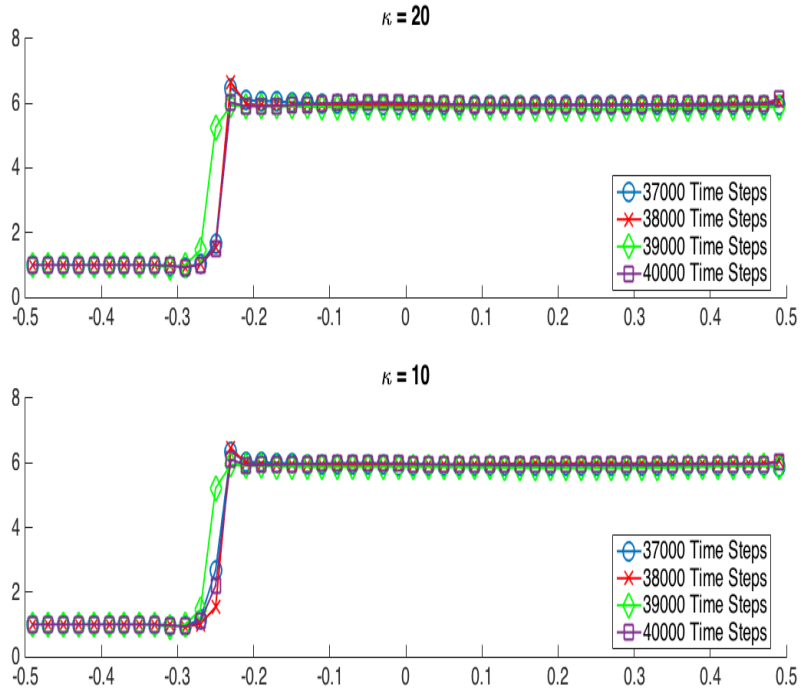

Figure 4.28 – Density plots of the ensemble mean for $\kappa = 10$ and $\kappa = 20$ using the *RoeEC*1 scheme at 37000, 38000, 39000 and 40000 time steps.

mean and the ensemble variance do not converge to a steady state solution if the value of κ is increased. This supports our conclusion that the ensemble mean and variance of the approximate measure valued solution continue to suffer from $1D$ instability and are not stable under decreasing amplitudes of perturbations.

In light of the results of the *RoeEC*1 scheme, we also explore the effects of increasing the parameter κ on the convergence of the ensemble mean and variance of the approximate measure valued entropy solution produced by the original Roe scheme. Once again, we would deduce from theoretical results (see, e.g., [18]) that the ensemble mean and variance should be stable with respect to an increase in the parameter κ. Unfortunately, this does not appear to be the case.

Figure 4.30 displays the $L1$-norm of the difference between successive solution approximations of the ensemble mean of the density at each time step for $\kappa = 20$ and $\kappa = 10$. Clearly, the error residual does not decrease as the value of κ is decreased and in fact increases considerably. While there is a gradual decay of the error residual, we feel that this does not disprove our basic conclusion that there is no convergence of the mean of the entropy

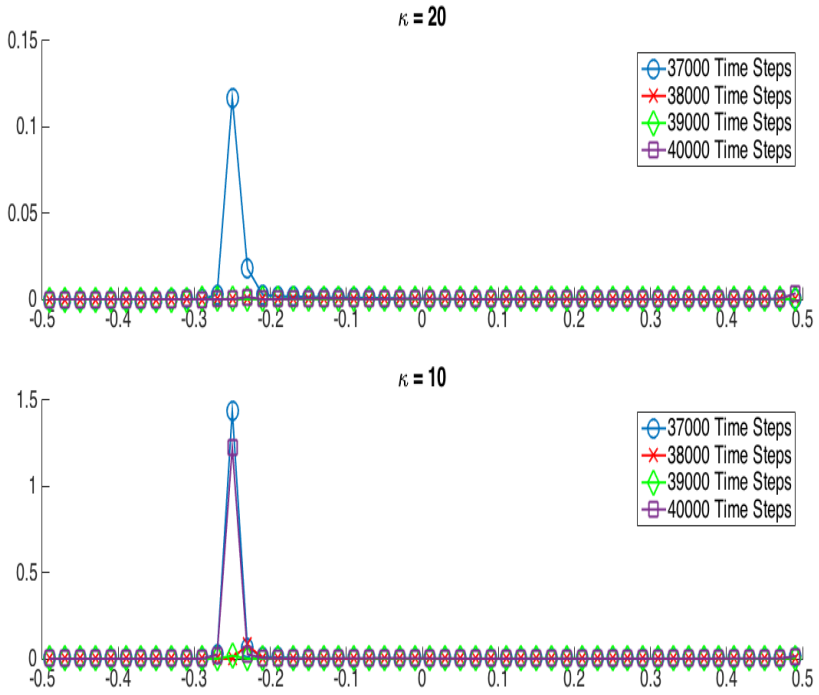

Figure 4.29 – Ensemble variance of the entropy measure valued solution for $\kappa = 10$ and $\kappa = 20$ using the *RoeEC*1 scheme at 37000, 38000, 39000 and 40000 time steps.

measure valued solution as κ is increased. Once more we remark that the error residuals for both values of κ are characterised by large oscillations which implies that in each case the ensemble mean still suffers from numerical instability and does not converge to a steady state shock solution even after $30,000$ time steps.

An analysis of the ensemble mean of the density supports our conclusion. Figure 4.31 displays the ensemble mean of the density for $\kappa = 20$ and $\kappa = 10$. We immediately observe observe that the shock position instability is much larger for the case $\kappa = 20$, which is in agreement with the results of the error residuals displayed in Figure 4.30. Indeed, the ensemble mean for the case $\kappa = 20$ continues to suffer from shock position instability even after $35,000$ time steps. This reinforces our conclusion that there is no convergence of the mean of the entropy measure valued solution to a steady state as κ is increased.

A similar result is obtained for the ensemble variance of the density. Figure 4.32 displays the ensemble variance for $\kappa = 20$ and $\kappa = 10$. We observe that while the spike in the variance is sharper for the case $\kappa = 20$ decrease as expected as the value of κ is decreased, there is nonetheless no convergence

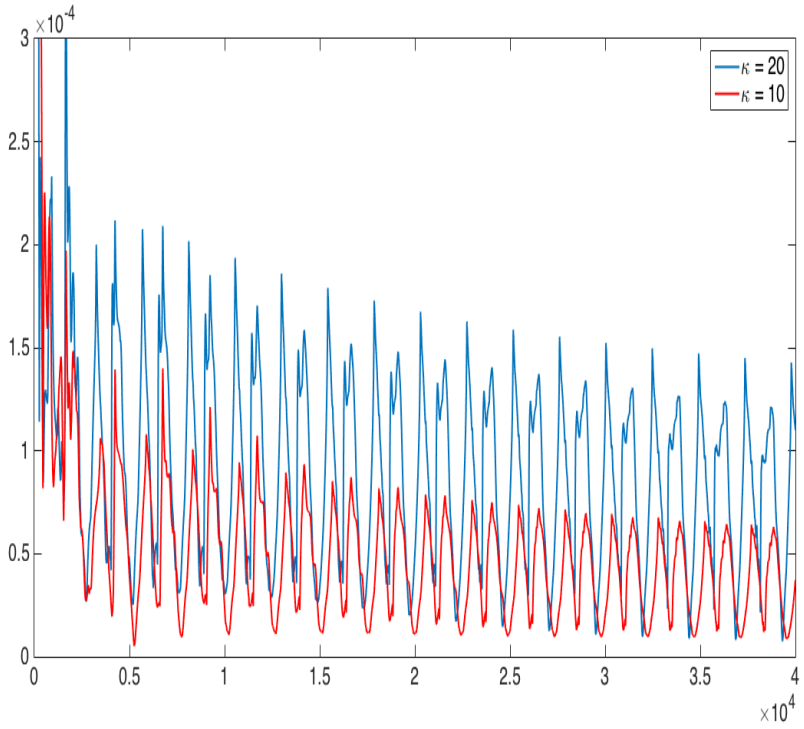

Figure 4.30 – The error $\|\rho^{n+1}_{\Delta x} - \rho^{n}_{\Delta x}\|_{L^1}$ vs. the number of time steps for $\kappa = 10$ and $\kappa = 20$ using the Roe scheme.

of the variance for either value of κ to a steady state even after $35,000$ time steps. It is thus reasonable to conclude that both the ensemble mean and the ensemble variance do not converge to a steady state solution as the value of δ is decreased. We therefore feel confident in our conclusion that the ensemble mean and variance of the approximate entropy measure valued solution are not stable under increasing values of the perturbation parameter κ.

To summarise, we feel that the following conclusions can be drawn in light of the results of Experiment 2.

- The error residual of the ensemble mean of the density of the corresponding measure valued Cauchy problem is smaller than the error residual of the solution to the original Cauchy problem.
- The ensemble mean and variance still suffer from numerical instability and therefore do not converge to a steady state solution even after $30,000$ time steps.
- There does not seem to be any convergence of the ensemble mean and variance as the value of κ is increased. Instead the error residuals imply that the mean and variance are even more unstable for higher values of κ.

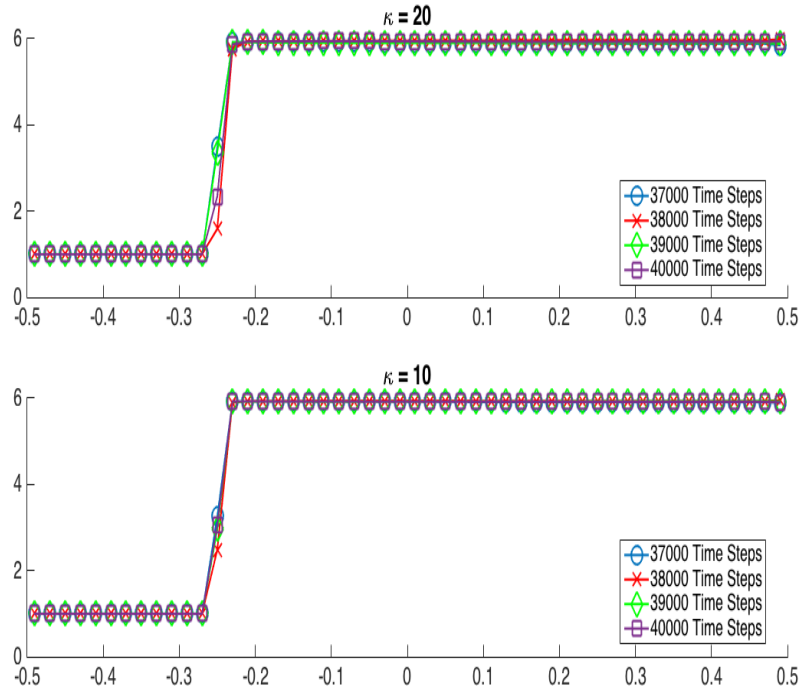

Figure 4.31 – Density plots of the ensemble mean for $\kappa = 10$ and $\kappa = 20$ using the Roe scheme at 37000, 38000, 39000 and 40000 time steps.

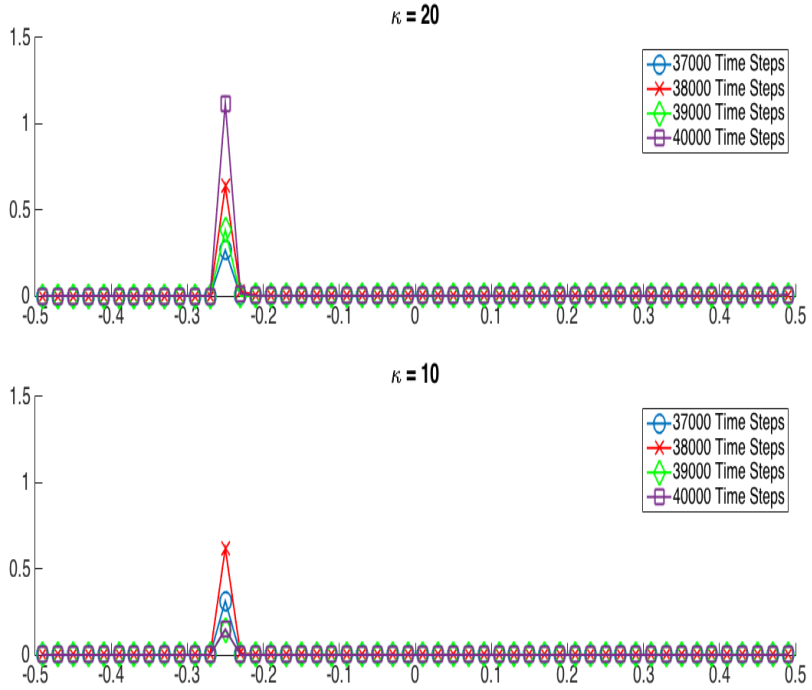

Figure 4.32 – Ensemble variance of the entropy measure valued solution for $\kappa = 10$ and $\kappa = 20$ using the Roe scheme at 37000, 38000, 39000 and 40000 time steps.

In summary, the results of Experiment 1 and Experiment 2 both seem to support the conclusion that the $1D$ carbuncle phenomenon cannot be completely resolved simply by considering a corresponding MV Cauchy problem and calculating the ensemble mean and ensemble variance. While the results of our numerical experiments do indicate that both the mean and variance are somewhat more stable than the original solutions, these statistical quantities continue to suffer from numerical instability and do not converge to a steady state shock solution. The failure of the entropy measure valued solution framework in resolving this instability seems to support the prevalent view in the literature that the origin of the $1D$ carbuncle phenomenon is numerical to a significant extent and is related to insufficient numerical diffusion. Interestingly the *RoeEC*1 scheme, which is not only an *entropy stable* scheme but also an *entropy consistent* scheme also suffers from this numerical instability. Therefore our conclusion seems to imply that entropy stability or indeed entropy consistency is not a sufficient condition for stable shock resolution for hypersonic flows even in the framework of entropy measure valued solution. It has already been established that the original Rusanov scheme, which is not entropy stable, does not display the $1D$ carbuncle phenomenon. We can therefore conclude that entropy stability, which is a weaker condition that entropy consistency, is neither a sufficient nor a necessary condition for stable shock resolution for hypersonic flows. This is an unfortunate conclusion to draw in light of the many advantages of the entropy measure valued solution framework.

Chapter 5

The Carbuncle Phenomenon in 1-1/2D

5.1 Numerical Experiments in 1-1/2D

The next step in our analysis is to consider a so-called one-and-one-half-dimensional problem involving the two-dimensional Euler equations and consisting of a steady normal shock. This is essentially a $2D$ version of the $1D$ Carbuncle phenomenon that we have considered in Chapter 4 but it is simpler than the full fledged $2D$ Carbuncle phenomenon consisting of hypersonic flow past a circular cylinder. This example was first developed by J. J. Quirk [36] and expanded on by, e.g., M. Dumbser, J. Moschetta and J. Gressier [13]. More recently K. Kitamura, P. Roe and F. Ismail [28], performed a very comprehensive series of experiments involving this problem and for the purpose of this thesis, we follow their example.

Let $\rho : \mathbb{R} \times \mathbb{R}_+ \to \mathbb{R}_+$, let $p : \mathbb{R} \times \mathbb{R}_+ \to \mathbb{R}_+$, let $u : \mathbb{R} \times \mathbb{R}_+ \to \mathbb{R}$, let $v : \mathbb{R} \times \mathbb{R}_+ \to \mathbb{R}$ and let $E : \mathbb{R} \times \mathbb{R}_+ \to \mathbb{R}_+$ be functions which denote the density, pressure, x-directional velocity, y-directional velocity and energy density of a compressible, inviscid fluid respectively. Then the compressible Euler equations in two dimension are given by

$$\partial_t \, \mathbf{u} + \partial_x(\, \mathbf{F}) + \partial_y(\mathbf{G}) = 0 \tag{5.1}$$

where

$$\mathbf{u} = \begin{bmatrix} \rho \\ \rho u \\ \rho v \\ E \end{bmatrix}, \qquad \mathbf{F} = \begin{bmatrix} \rho u \\ \rho u^2/2 + p \\ \rho u v \\ \big(u(E+p)\big) \end{bmatrix}, \qquad \mathbf{G} = \begin{bmatrix} \rho v \\ \rho u v \\ \rho v^2/2 + p \\ \big(v(E+p)\big) \end{bmatrix}, \tag{5.2}$$

and the equation of state is given by

$$E = \frac{p}{\gamma - 1} + 1/2\rho u^2 + 1/2\rho v^2. \tag{5.3}$$

The computational domain consists of a uniform 25×25 grid with piecewise constant initial conditions for the left ($L : i \leq 12$) and right ($R : i \geq 14$) states:

$$\mathbf{U}_L = \begin{bmatrix} 1 \\ 1 \\ 0 \\ \frac{1}{\gamma(\gamma-1){M_0}^2} + \frac{1}{2} \end{bmatrix}, \qquad \mathbf{U}_R = \begin{bmatrix} f(M_0) \\ 1 \\ 0 \\ \frac{g(M_0)}{\gamma(\gamma-1){M_0}^2} + \frac{1}{2f(M_0)} \end{bmatrix} \tag{5.4}$$

where

$$f(M_0) = \left(\frac{2}{(\gamma+1){M_0}^2} + \frac{\gamma-1}{\gamma+1} \right)^{-1}, \qquad g(M_0) = \frac{2\gamma {M_0}^2}{\gamma+1} - \frac{\gamma-1}{\gamma+1}, \tag{5.5}$$

and the internal shock condition ($M : i = 13$) is calculated using the condition (4.3).

Thus, the setup for this $1 - 1/2D$ problem is very similar to the setup for the $1D$ problem. Following K. Kitamura, P. Roe and F. Ismail [28], the free-stream Mach number M_0 is set equal to 6.0 and the boundary conditions are chosen to be periodic in the y-direction and identical to the $1D$ boundary conditions in the x-direction. However, we depart from the example of K. Kitamura, P. Roe and F. Ismail [28] by introducing a very small perturbation of 10^{-14} in a single, randomly chosen cell upstream of the shock. This introduces a source of multidimensional instability in the problem which should lead to numerical instability that is qualitatively different from $1D$ instability.

Similar to the $1D$ case, our first goal is to examine the stability of the previously introduced numerical schemes for different values of the shock-position parameter ε. We categorise our numerical schemes in the following way:

- We declare a numerical scheme to be $1 - 1/2D$ **stable** if the approximate solutions produced by the scheme converge to a steady state shock solution for all values of ε.
- We declare a numerical scheme to be $1 - 1/2D$ **unstable type 1** if the approximate solutions produced by the scheme do not converge to a steady state shock solution and instead oscillate and form jagged spikes for some value of ε.

- We declare a numerical scheme to be $1-1/2D$ **unstable type 2** if the approximate solutions produced by the scheme either diverge completely or evolve to a shock-free solution.

All computations were performed using a CFL number of $1/3$, which resulted in a mesh-width to time-step ratio $\lambda \approx 0.25$ and the simulations were run for a minimum of $20,000$ time steps.

5.1.1 Results of the Numerical Experiments

As expected our results indicate that the stability of the shock depends on the numerical scheme employed and the value of the parameter ε. Thus for example, the Roe scheme seems to be stable for some choices of ε and M_0 and unstable for others while the Rusanov scheme seems to be stable for all values of ε and M_0. Table 5.1 displays the results of the stability tests for the different schemes we have tested.

Scheme	$1-1/2D$ Stability
RoeEC1 $(\alpha = 0.2)$	Unstable Type 1
RoeEC1 $(\alpha = 0.8)$	Unstable Type 2
Roe	Unstable Type 2
RoeES	Stable
Rusanov	Stable
RusanovES	Stable

Table 5.1 – Summary of the $1-1/2D$ stability of different numerical schemes.

Scheme	ε	M_0
RoeEC1 $(\alpha = 0.2)$	0.7	6
RoeEC1 $(\alpha = 0.8)$	0.4	6
Roe	0.2, 0.5	6
RoeES	0.4	6
Rusanov	0.7	6
RusanovES	0.6	6

Table 5.2 – Concrete choice of the parameters ε and M_0 for the purpose of our experiments.

Our results indicate that the numerical schemes that are $1D$ unstable are also $1-1/2D$ unstable. As shown in Figure 5.1 and Figure 5.2 the *RoeEC1* ($\alpha = 0.2$) scheme for instance displays numerical instability in the form of oscillating spikes downstream of the shock which is qualitatively different and indeed much worse than the simple $1D$ shock instability observed in the previous section. All figures presented in this section were obtained using a

specific choice of the shock position parameter ε as given in Table 5.2.

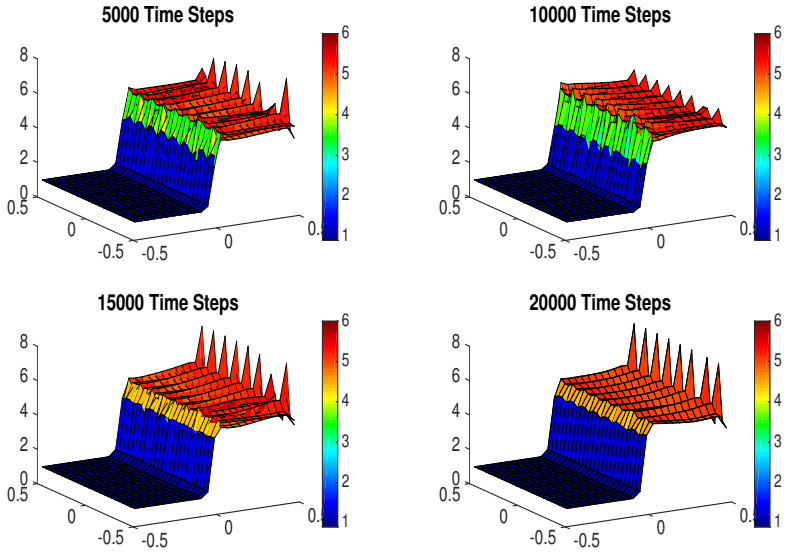

Figure 5.1 – Unstable Type 1. Density plots of the $RoeEC1$ ($\alpha = 0.2$) scheme for $\varepsilon = 0.7$ at 37000, 38000, 39000 and 40000 time steps.

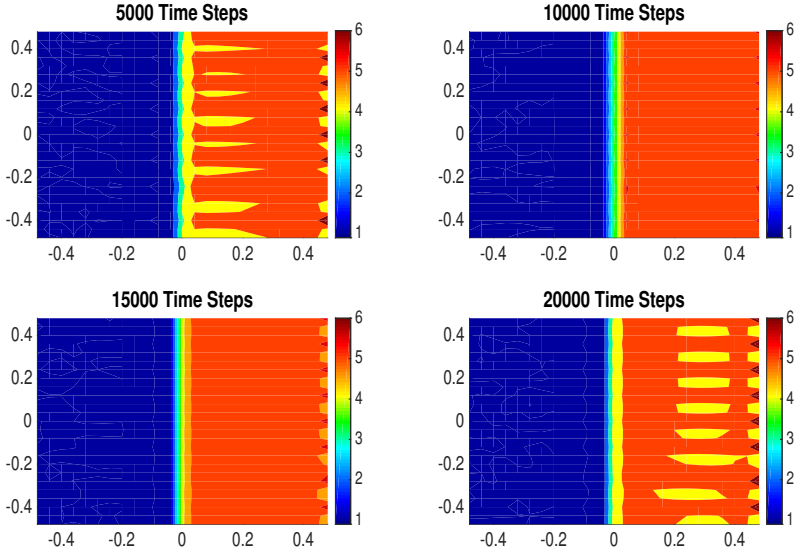

Figure 5.2 – Unstable Type 1. Isodensity contour plots of the $RoeEC1$ ($\alpha = 0.2$) scheme for $\varepsilon = 0.7$ at 37000, 38000, 39000 and 40000 time steps.

Figure 5.3 and Figure 5.4 display the the density and isodensity contour plots respectively of the approximate solutions produced by the $RoeEC1$ ($\alpha = 0.8$) scheme. In a significant departure from the results of the $1D$

stability tests, the *RoeEC*1 ($\alpha = 0.8$) scheme, which is $1D$ stable is completely unstable in $1 - 1/2D$ and leads to approximate solutions that diverge. This is in agreement with the results of K. Kitamura, P. Roe and F. Ismail [28] who point out that the *RoeEC*1 ($\alpha = 0.8$) is unstable in higher dimensions.

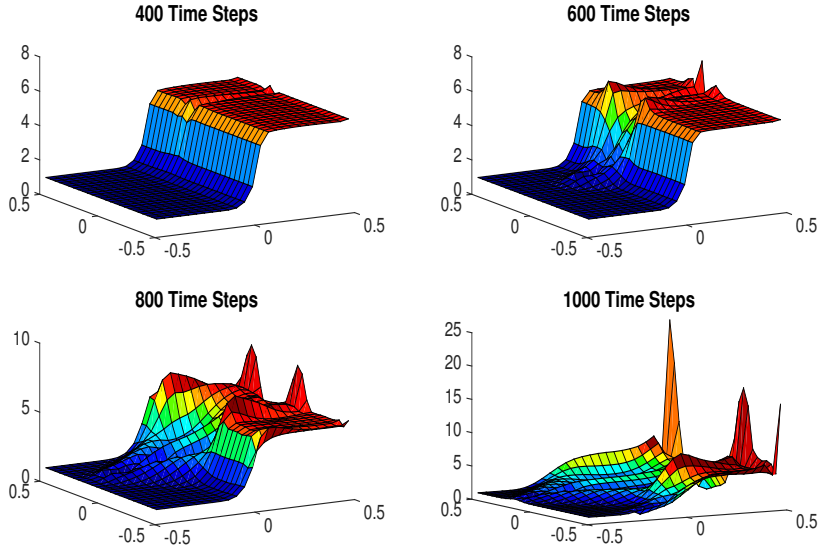

Figure 5.3 – Unstable Type 2. Density plots of the *RoeEC*1 ($\alpha = 0.8$) scheme for $\varepsilon = 0.5$ at 37000, 38000, 39000 and 40000 time steps.

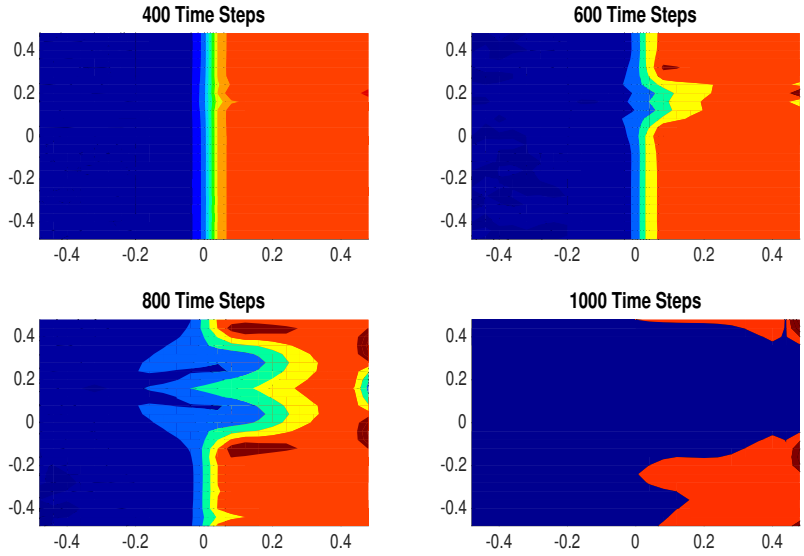

Figure 5.4 – Unstable Type 2. Isodensity contour plots of the *RoeEC*1 ($\alpha = 0.8$) scheme for $\varepsilon = 0.5$ at 37000, 38000, 39000 and 40000 time steps.

The results for the Roe scheme are extremely interesting. Figure 5.5 and Figure 5.6 display the density and the isodensity contour plots respectively of the approximate solution produced by the Roe scheme for $\varepsilon = 0.2$. The approximate solution quickly evolves to a shock-free state and therefore the Roe scheme is $1 - 1/2D$ unstable of type 2. On the other hand as displayed in Figure 5.7 and Figure 5.8 the approximate solutions for the case $\varepsilon = 0.5$ display numerical instability in the form of spikes similar to the *RoeEC*1 scheme. Thus the form of $1 - 1/2D$ instability in the case of the Roe scheme depends on the value of the parameter $\varepsilon = 0.5$.

On the other hand as shown in Figures 5.9-5.11, the remaining schemes are able to successfully resolve the steady shock and are therefore $1 - 1/2D$ stable. We observe however that as expected the Rusanov scheme and the *RusanovES* scheme are more dissipative than the *RoeES* scheme. Furthermore, the *RoeES* scheme, while $1 - 1/2D$ stable, nevertheless produces solutions with significant overshoot. This is a known problem associated with the *RoeES* scheme and as observed by F. Ismail and P.Roe [24] is likely caused due to insufficient entropy dissipation at the shock.

As with the $1D$ numerical experiments, a complete breakdown of the results of this $1 - 1/2D$ numerical experiment for all possible values of ε can be found in [28].

5.1.2 A Possible Case of Even-Odd Decoupling?

In view of the results of Section 5.1.1 it is worth exploring whether the origin of the $1 - 1/2D$ numerical instability of type 1, which results in oscillating spikes is caused by some form of even-odd decoupling. This is a well known numerical problem that arises for example when solving for the pressure field of the incompressible Navier-Stokes equations (see, e.g., [30]) and is manifested as an oscillatory 'checkerboard' distribution of the pressure field. In order to explore this idea further, we perform the following simple experiment.

We consider the same $1 - 1/2D$ Cauchy problem introduced in Section 5 but with one fundamental change. Instead of a normal shock aligned in the x-direction, we consider a sinusoidal shock position. More specifically, instead of fixing the value of the shock location parameter ε for each cell in the y-direction, we instead define the shock location as

$$\varepsilon(y) = 1/2\big(1 + \sin(\tau\pi y + \Theta\pi)\big) \tag{5.6}$$

where τ is a frequency parameter that changes the period of the sinusoidal function and Θ is a $[0, 1]$-uniformly distributed random variable which introduces a source of randomness across different simulations. Figure 5.12 and

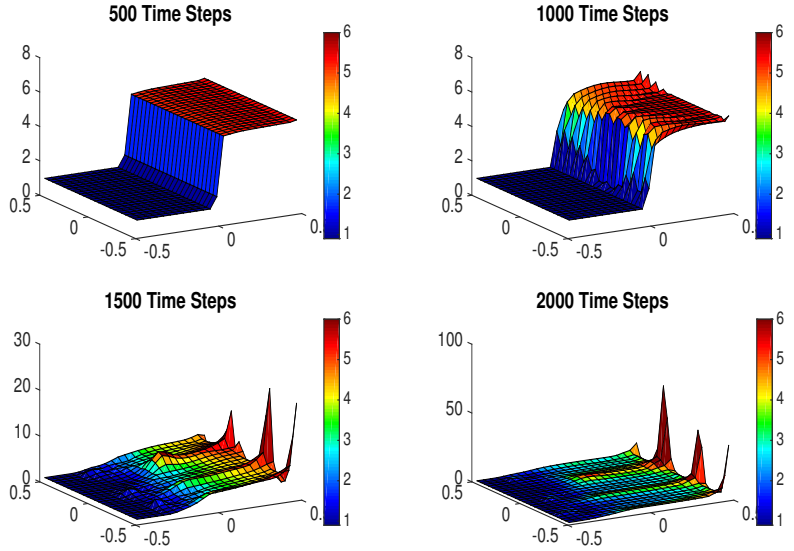

Figure 5.5 – Unstable Type 2. Density plots of the original Roe scheme for $\varepsilon = 0.2$ at 37000, 38000, 39000 and 40000 time steps.

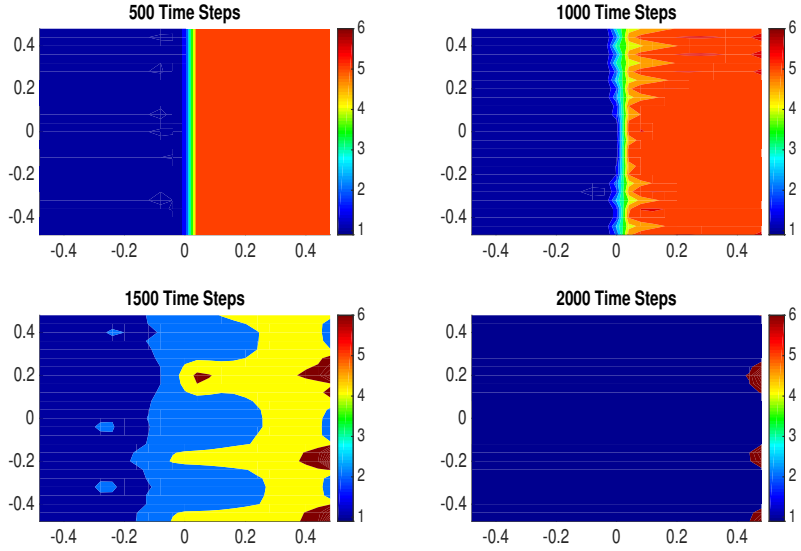

Figure 5.6 – Unstable Type 2. Isodensity contour plots of the original Roe scheme for $\varepsilon = 0.2$ at 37000, 38000, 39000 and 40000 time steps.

Figure 5.13 display the initial isodensity contour plots for this experiment for the values $\tau = 4$ and $\tau = 20$ respectively and for different realisations of the random variable Θ. Once again we employ a fixed mesh-width to time-step ratio $\lambda = 0.25$ and perform all simulations for a minimum of $20,000$ time steps using the $RoeEC1$ ($\alpha = 0.2$).

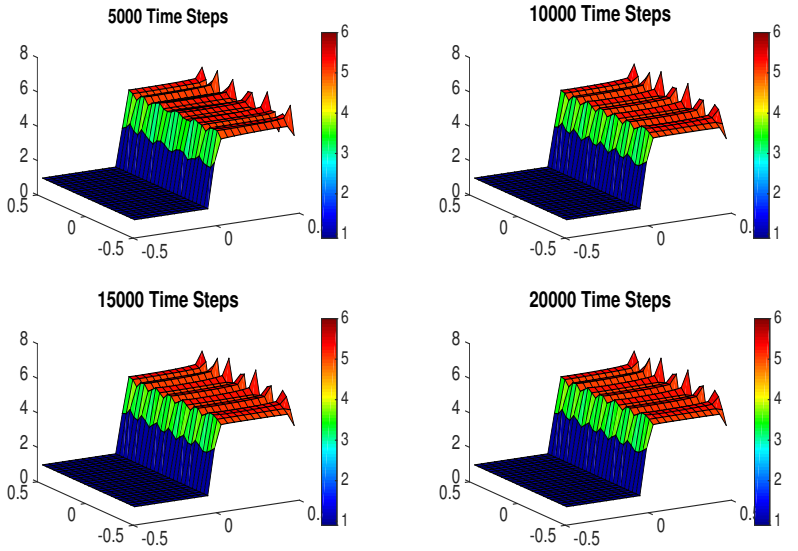

Figure 5.7 – Unstable Type 1. Density plots of the original Roe scheme for $\varepsilon = 0.5$ at 37000, 38000, 39000 and 40000 time steps.

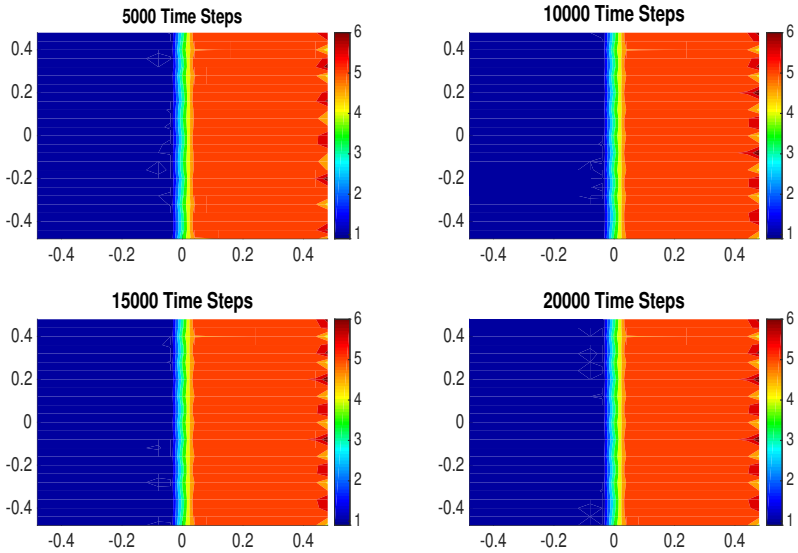

Figure 5.8 – Unstable Type 1. Isodensity contour plots of the original Roe scheme for $\varepsilon = 0.5$ at 37000, 38000, 39000 and 40000 time steps.

Our goal is to explore the effects of increasing the value of the frequency parameter τ on the approximate solutions produced by the $RoeEC1$ ($\alpha = 0.2$) scheme. If the $1 - 1/2D$ numerical instability is indeed caused by even-odd decoupling we would expect to observe that the low frequency test case and the high frequency test case produce approximate solutions that are

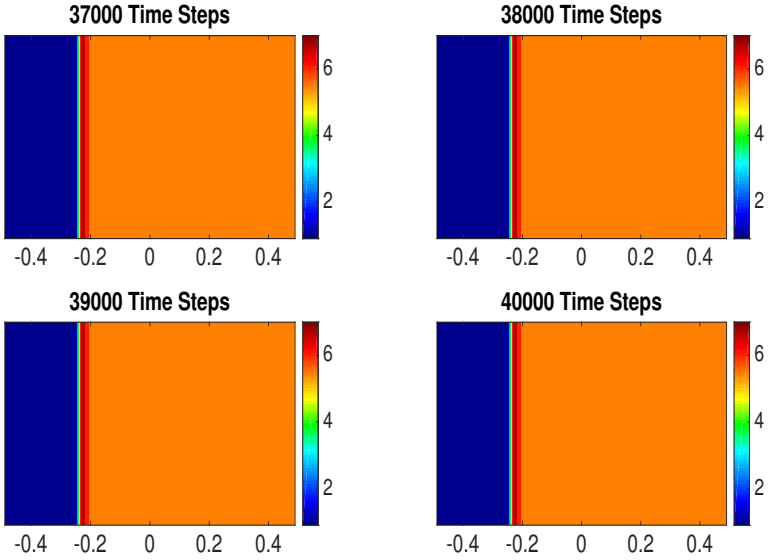

Figure 5.9 – Stable. Isodensity contour plots of the *RoeES* scheme for $\varepsilon = 0.4$ at 37000, 38000, 39000 and 40000 time steps.

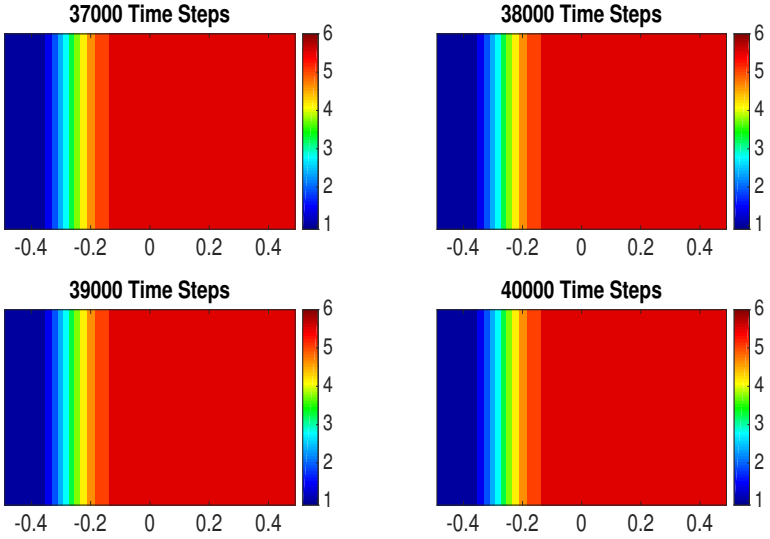

Figure 5.10 – Stable. Isodensity contour plots of the Rusanov scheme for $\varepsilon = 0.7$, $M_0 = 20$ at 37000, 38000, 39000 and 40000 time steps.

characterised by low and high frequency spikes respectively.

Figure 5.14 and Figure 5.15 display the isodensity contour plots after 8000 time steps for the values $\tau = 4$ and $\tau = 20$ respectively and for different realisations of the random variable Θ. As expected the approximate solutions display oscillating spikes but the frequency of these oscillations does not cor-

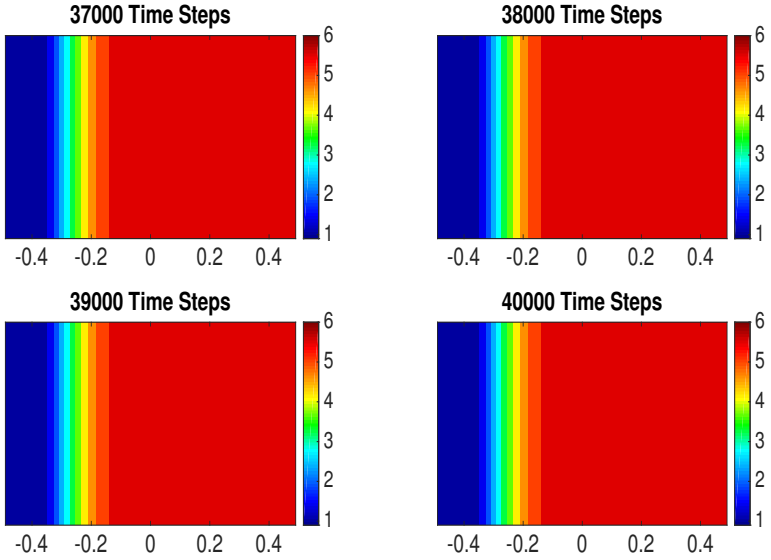

Figure 5.11 – Stable. Isodensity contour plots of the *RusanovES* scheme for $\varepsilon = 0.6, M_0 = 20$ at 37000, 38000, 39000 and 40000 time steps.

respond to the frequency parameter τ. Specifically, a high frequency shock location does not produce high frequency oscillations and a low frequency shock location does not produce low frequency oscillations. This indicates that the origin of the $1 - 1/2D$ is in fact not due to even-odd decoupling.

5.1.3 Numerical Experiments involving the $1 - 1/2D$ MV Cauchy Problem

Experiment 1

We consider the corresponding $1 - 1/2D$ MV Cauchy problem involving the Euler equations (5.1) by perturbing the initial conditions (5.4).

Let $(\Omega, \mathcal{F}, \mathbb{P})$ be a probability space, let $X \colon \Omega \to [-0.5, 0.5]$ be a uniformly distributed random variable, let $\delta \in [0, 1]$ be a constant and consider the same Cauchy problem introduced in Section (5.1) but with perturbed shock position parameter given by

$$\tilde{\varepsilon} = \varepsilon + \delta X. \tag{5.7}$$

The remaining set up including the initial conditions and the boundary conditions are left unchanged. We again use Monte-Carlo simulations to estimate the mean and variance of the approximate entropy measure valued solutions to the associated $1 - 1/2D$ MV Cauchy problem and analyse the

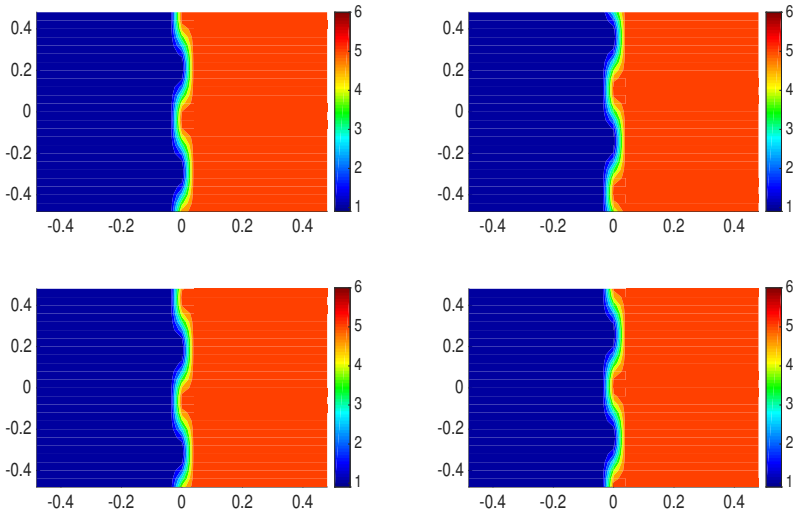

Figure 5.12 – Initial isodensity contour plots for $\tau = 4$ and different realisations of the random variable Θ.

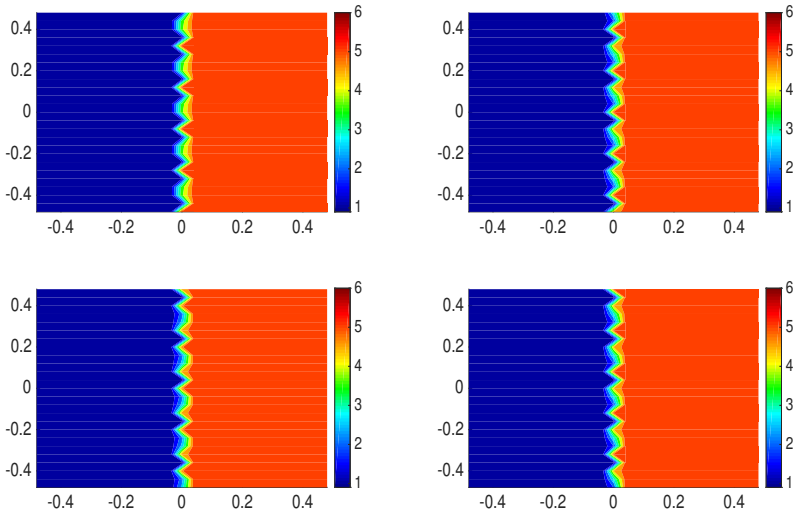

Figure 5.13 – Initial isodensity contour plots for $\tau = 20$ and different realisations of the random variable Θ.

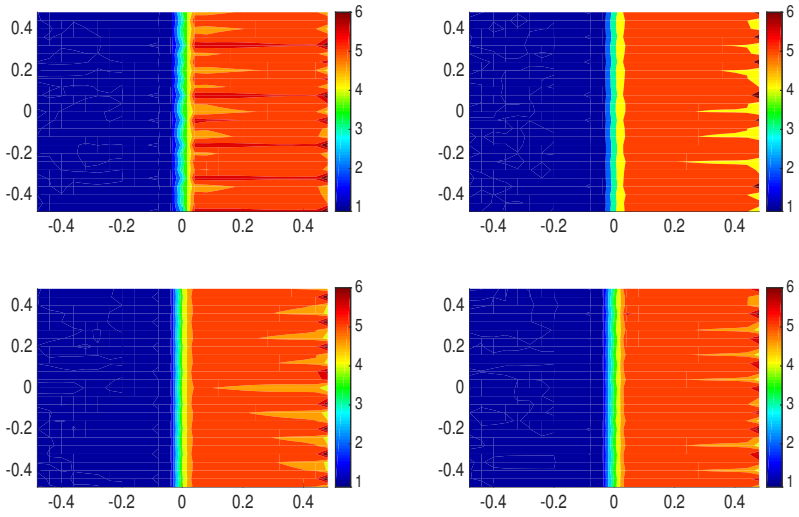

Figure 5.14 – Isodensity contour plots for $\tau = 4$ and different realizations of the random variable Θ after 8000 time steps.

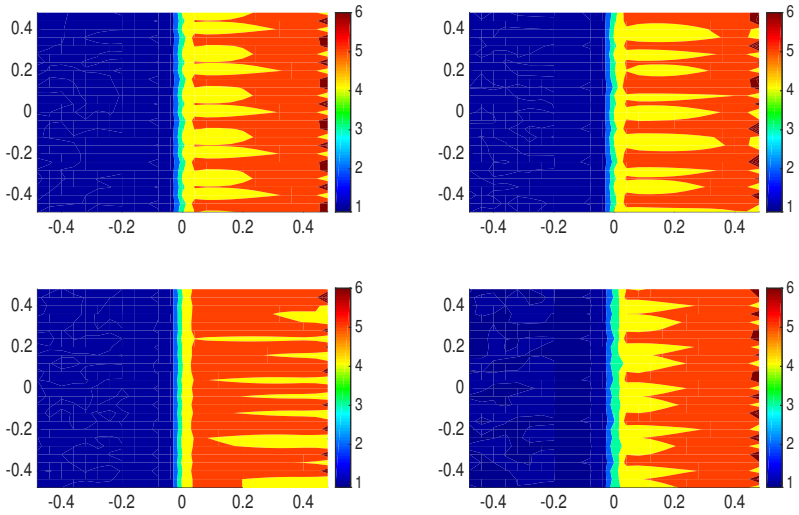

Figure 5.15 – Isodensity contour plots for $\tau = 20$ and different realizations of the random variable Θ after 8000 time steps.

convergence of these statistical quantities. Based on our results in Section 5.1.1 we are interested primarily in the entropy consistent *RoeEC*1 ($\alpha = 0.2$) scheme since this is the only $1 - 1/2D$ unstable scheme of type 1. It is obviously too much to expect numerical instability of type 2 to be resolved by considering the corresponding MV Cauchy problem. For the purpose of this section we consider the test case involving *RoeEC*1 ($\alpha = 0.2$) with parameter values $\delta = 0.2$, $\varepsilon = 0.7$, $M_0 = 6$. All results were computed using 400 Monte-Carlo iterations.

Figure 5.16 and Figure 5.17 display the density plot and the isodensity contour plots respectively of the ensemble mean of the approximate entropy measure valued solution produced by the *RoeEC*1 scheme. The results indicate that the ensemble mean does not suffer from any form of the $1 - 1/2D$ instability and indeed there is no visible evidence of oscillating spikes which were observed in the single samples. Nevertheless, a close examination reveals that the shock location is still slightly unstable and therefore the ensemble mean still suffers from the original $1D$ instability. This is an extremely interesting result because it seems to imply that while the entropy measure valued solution framework is incapable of resolving $1D$ numerical instability, it is nevertheless remarkably successful at resolving the more severe $1 - 1/2D$ numerical instability. This suggests that there is a significant difference between the $1D$ and $1 - 1/2D$ forms of numerical instability.

For a more complete analysis, we also consider the ensemble variance of the ensemble variance of the density of the measure valued entropy solution produced by the *RoeEC*1 scheme. As displayed in Figure 5.18, the variance consists of a smaller spike at the shock location and a larger spike at the outflow boundary. The spike in the variance at the outflow boundary is of course caused by oscillating spikes due to the $1 - 1/2D$ numerical instability so this result is to be expected. We observe that the variance at the shock location does oscillate slightly, which is likely due to the unresolved $1D$ shock instability but the variance at the outflow appears stable. This result therefore also supports out conclusion that while $1D$ numerical instability is not completely resolved, the entropy measure valued solution framework is nevertheless successful at resolving the more severe $1 - 1/2D$ numerical instability.

The analysis of the error residual strongly supports our conclusion. Figure 5.19 displays the $L1$-norm of the difference between the initial condition and the ensemble mean of the density at each time step for the *RoeEC*1 scheme. We observe that the error of the ensemble mean is significantly smaller than the error of the original solution. Indeed, by comparing to Figure 4.7 we immediately observe that the error residual for the ensemble mean is in fact lower than the error residual of both the Rusanov and the *RusanovES* scheme. Furthermore, while the error residual still suffers from oscillations,

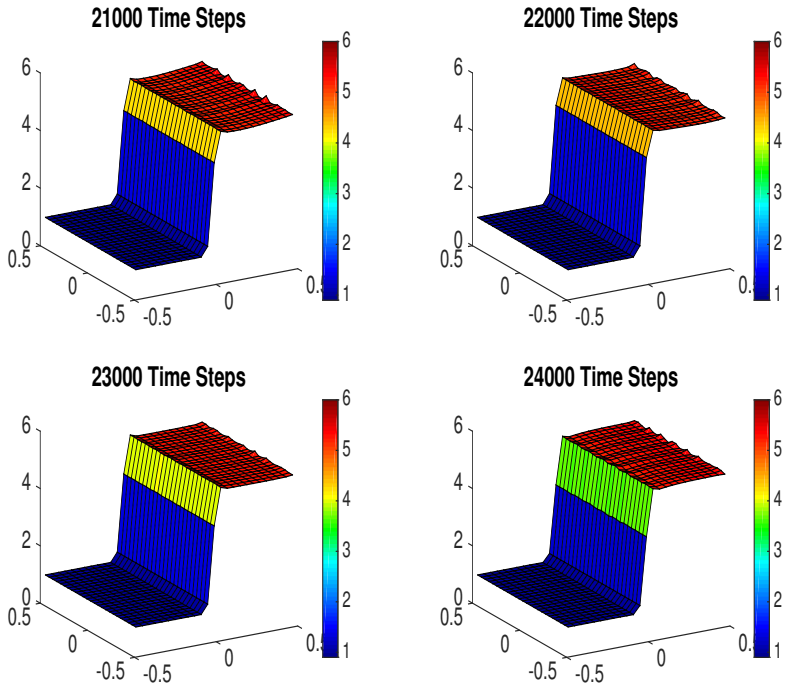

Figure 5.16 – Density plots of the ensemble mean using the *RoeEC*1 scheme at 21000, 22000, 23000 and 24000 time steps.

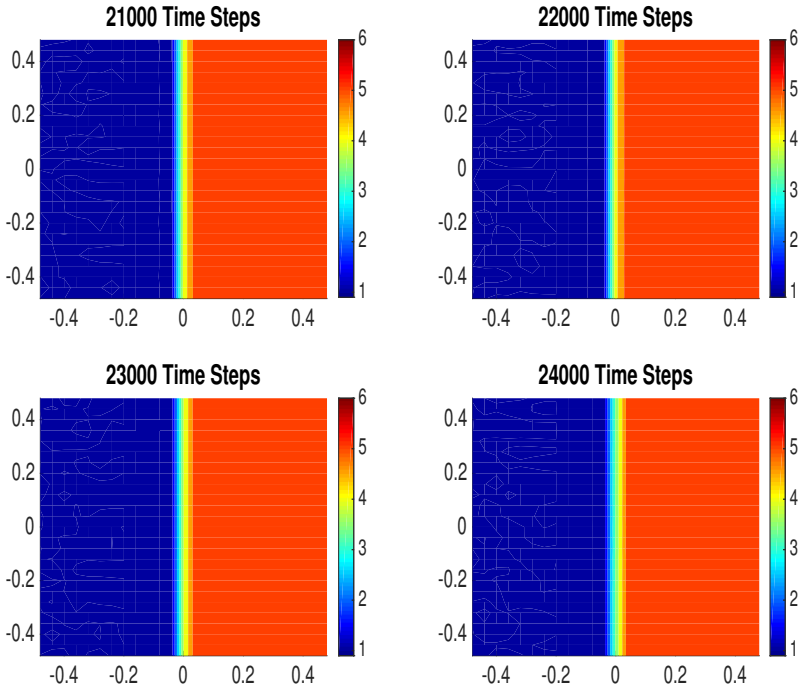

Figure 5.17 – Isodensity contour plots of the ensemble mean using the *RoeEC*1 scheme at 21000, 22000, 23000 and 24000 time steps.

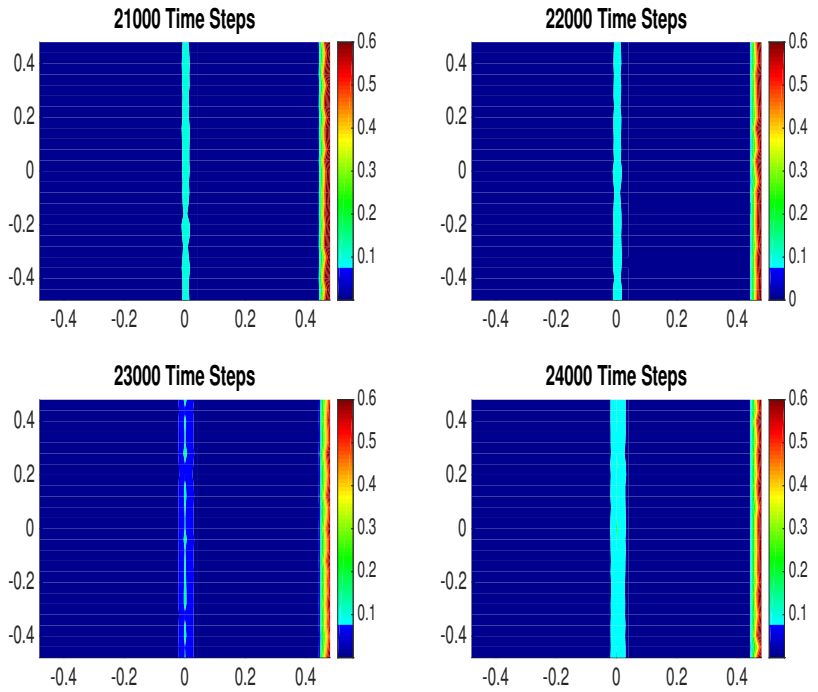

Figure 5.18 – Contour plots of the ensemble variance of the density using the *RoeEC*1 scheme at 21000, 22000, 23000 and 24000 time steps.

these are significantly smaller in magnitude. We therefore feel confident in concluding that apart from some slight shock position instability, the ensemble mean and variance are much more stable and do not suffer from any $1 - 1/2D$ instability.

In order to shed further light on these results, we explore the effects of increasing the mesh width refinement on the convergence of the ensemble mean and variance of the density. In particular we repeat the same experiment with a computational domain consisting of 50×50 cells i.e. with mesh width exactly halved. Figure 5.20 displays the $L1$-norm of the difference between the initial condition and the ensemble mean of the density at each time step for both the original 25×25 grid and the 50×50 grid. Clearly the error residual at higher mesh resolution is significantly smaller than the error residual at low mesh resolution. Nevertheless, the error for the 50×50 grid still suffers from oscillations. In light of the results of the ensemble mean and ensemble variance given below, we feel that this is an indication that using a fine mesh results in less numerical dissipation, which causes the $1D$ numerical instability to be much worse.

Figure 5.21 and Figure 5.22 display the density plot and isodensity contour

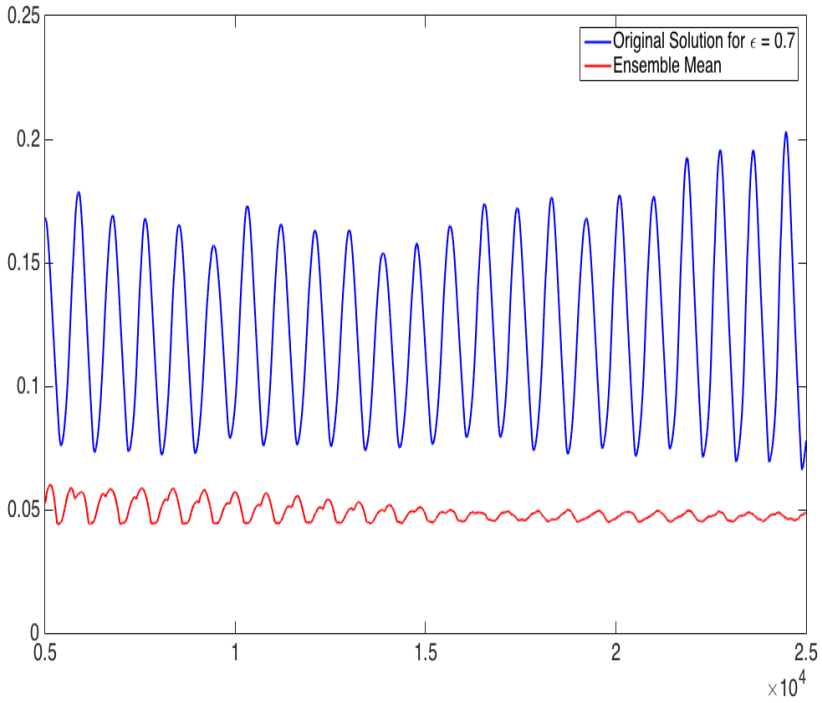

Figure 5.19 – The error $\|\rho_0 - \rho_\Delta^n\|_{L^1}$ vs. the number of time steps for the ensemble mean and the original solution with $\varepsilon = 0.7$ using the *RoeEC*1 scheme.

plots of the ensemble mean in the case of the 50×50 grid. As expected we observe that there is little indication of severe instability in the plots of the ensemble mean. Indeed, similar to the case for the coarse mesh, the ensemble mean once again does not appear to suffer from $1 - 1/2D$ numerical instability in the form of oscillating spikes.

The results for the ensemble variance of the density are more interesting. Figure 5.23 displays the ensemble variance for the 50×50 mesh and we immediately observe a significant qualitative difference from the coarser 25×25 mesh. Indeed, the spike in the variance at the shock location is much sharper and significantly more unstable and at the same time the variance at the outflow is significantly smaller and more sharply refined. The variance in this case therefore is qualitatively very similar to the case of $1D$ numerical instability. This seems to support our conclusion that $1D$ numerical instability in the form of an unstable shock location is a significant problem for higher mesh resolutions.

Next, We explore the effect of decreasing the amplitude of the perturbation parameter δ on the stability of the ensemble mean and variance of the density of the approximate entropy measure valued solutions. We recall

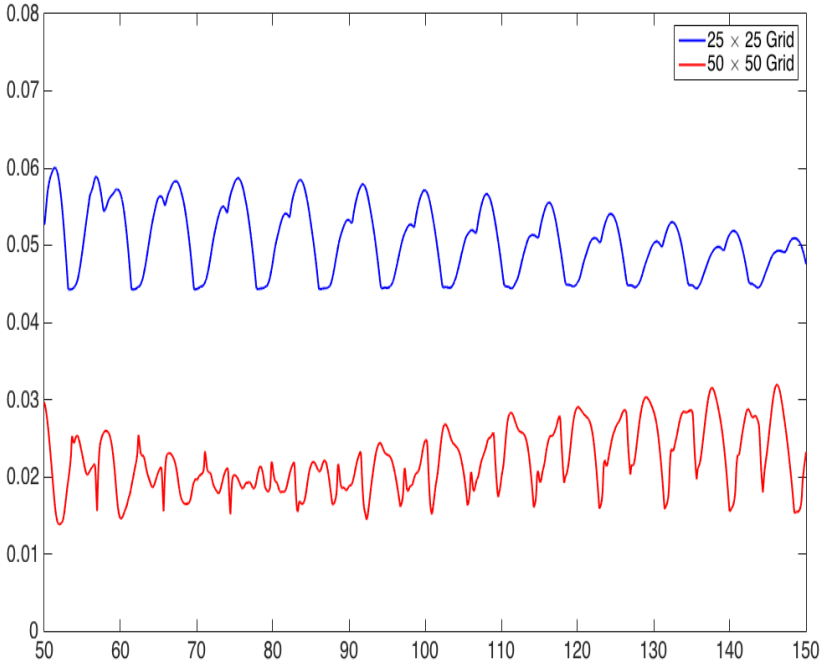

Figure 5.20 – The error $\|\rho_0 - \rho_\Delta^n\|_{L^1}$ vs. the number of time steps for both the 50×50 grid and the 25×25 grid using the *RoeEC*1 scheme.

that theoretical results (see, e.g., [18]) imply that decreasing the parameter δ should lead to convergence of the mean and variance of the measure entropy valued solution.

Figure 5.24 displays the $L1$-norm of the difference between the initial condition and the ensemble mean of the density at each time step for different values of the parameter δ. In contrast to the $1D$ case, we observe that the error residuals remain qualitatively similar as the value of δ is decreased. This is an important result because it seems to imply that ensemble mean is stable with respect to perturbations of the parameter δ. While the error residuals for all values of δ are still characterised by oscillations, the magnitude of these oscillations is significantly smaller than magnitude of the oscillations in the case of a single sample.

An analysis of the ensemble mean of the density for different values of δ reveals once again that the ensemble mean in each case does not suffer from $1 - 1/2D$ numerical instability. Figure 5.25 and Figure 5.26 display the ensemble mean of the density for different values of $\delta = 0.10$ and $\delta = 0.05$ respectively and both plots are almost identical. In fact there is little observable deviation of the shock location as well for both cases. This supports our

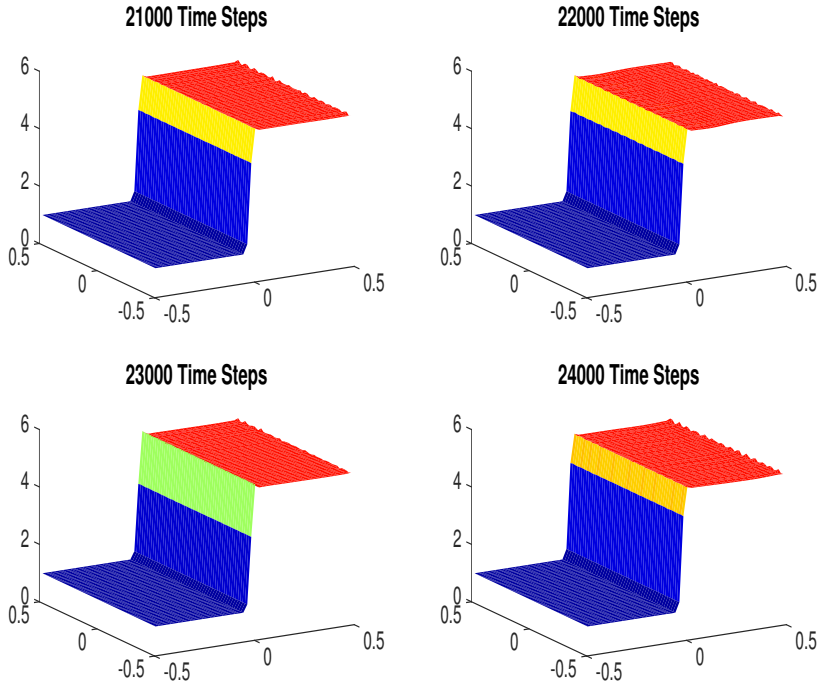

Figure 5.21 – Density plots of the ensemble mean for the 50×50 grid using the *RoeEC*1 scheme at 21000, 22000, 23000 and 24000 time steps.

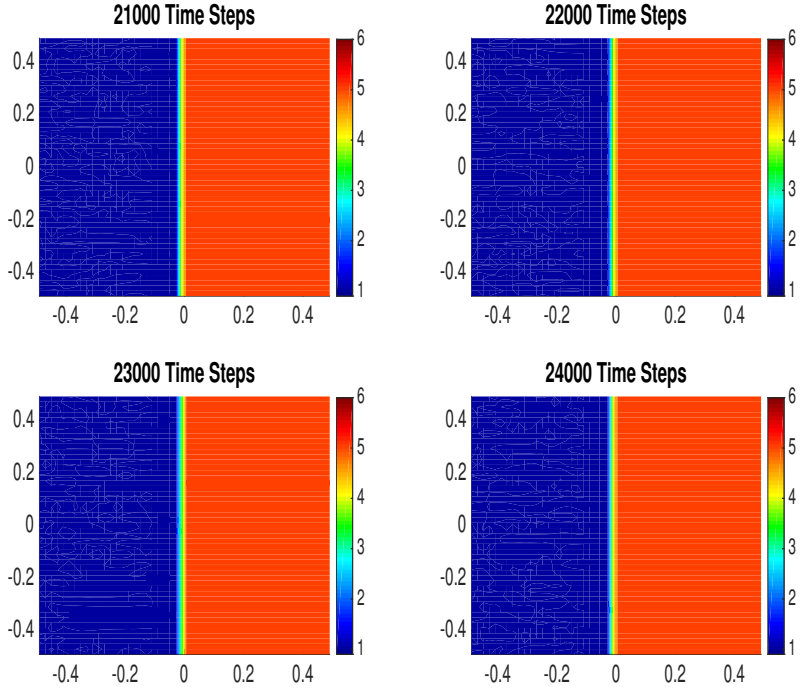

Figure 5.22 – Isodensity contour plots of the ensemble mean for the 50×50 grid using the *RoeEC*1 scheme at 21000, 22000, 23000 and 24000 time steps.

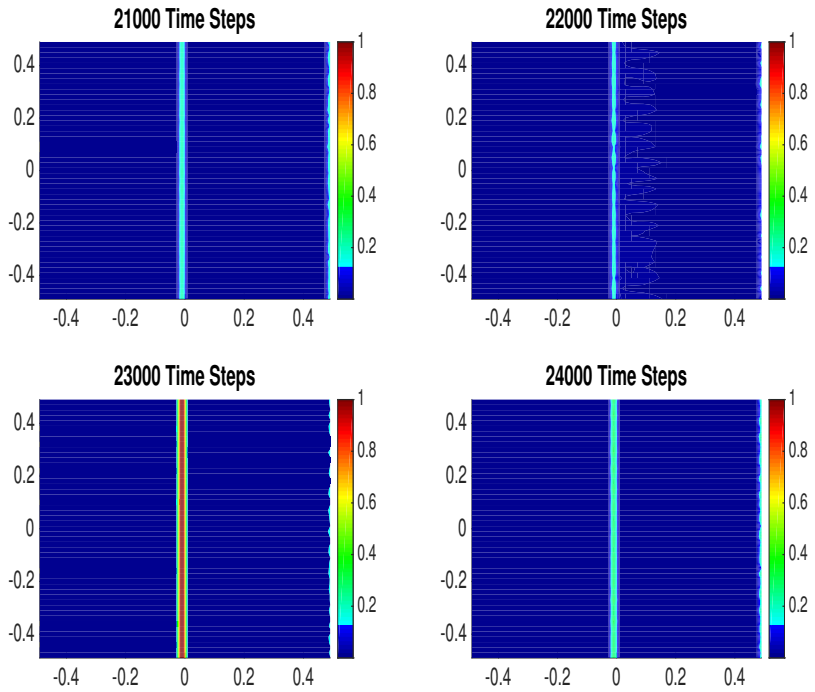

Figure 5.23 – Contour plots of the ensemble variance of the density for the 50×50 grid using the *RoeEC*1 scheme at 21000, 22000, 23000 and 24000 time steps.

conclusion that the ensemble mean of the entropy solution is stable under perturbations of the initial shock position.

A similar result is obtained for the ensemble variance of the density. Figure 5.27 and Figure 5.28 display the ensemble variance for $\delta = 0.10$ and $\delta = 0.05$ respectively. We once again observe that the variance consists of a small spike at the shock location and a larger spike at the outflow and furthermore, while the variance at the shock location does oscillate slightly, the variance at the outflow appears more stable. It is thus reasonable to conclude once more that the ensemble variance also does not suffer from $1 - 1/2D$ instability and is stable under perturbation of the shock position parameter ε.

In view of the results of Experiment 1 we feel that the following three conclusions can be drawn:

- The error residual of the ensemble mean of the density of the corresponding measure valued Cauchy problem is significantly smaller than the error residual of the solution to the original Cauchy problem.
- The ensemble mean and variance still suffer from $1D$ numerical instability but do not appear to suffer from the more severe $1 - 1/2D$

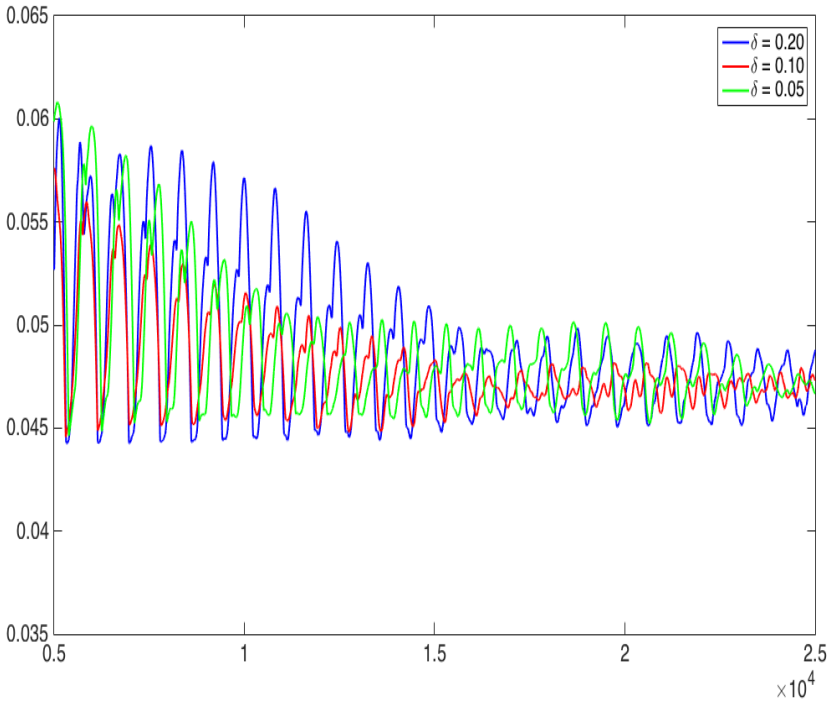

Figure 5.24 – The error $\|\rho_0 - \rho_\Delta^n\|_{L^1}$ vs. the number of time steps for different values of the parameter δ using the $RoeEC1$ scheme.

instability. The $1D$ numerical instability in the form of an oscillating shock position is more severe for a higher mesh resolution.

- Both the ensemble mean and the ensemble variance seem to be stable under perturbations of the shock position parameter ε.

We feel that this is an extremely promising result because it indicates that the $1 - 1/2D$ carbuncle phenomenon can be resolved to a large degree using the framework of entropy measure valued solutions. In particular this also seems to support our conclusion that nature of the Carbuncle phenomenon is significantly different in $1D$ and $1 - 1/2D$.

Experiment 2

We next consider the following corresponding $1 - 1/2D$ MV Cauchy problem involving the Euler equations (5.1) by perturbing the initial conditions (5.4).

Let $(\Omega, \mathcal{F}, \mathbb{P})$ be a probability space, let $\Theta\colon \Omega \to [0, 25]$ be a uniformly distributed random variable, let $\kappa \in \mathbb{R}$ be a constant and consider the same

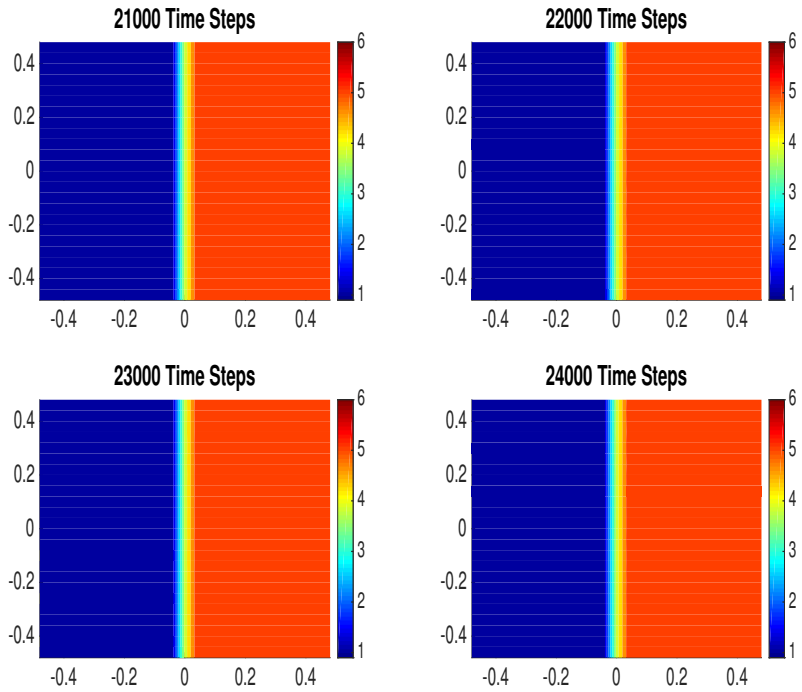

Figure 5.25 – Isodensity contour plots of the ensemble mean for the parameter $\delta = 0.10$ using the *RoeEC*1 scheme at 21000, 22000, 23000 and 24000 time steps.

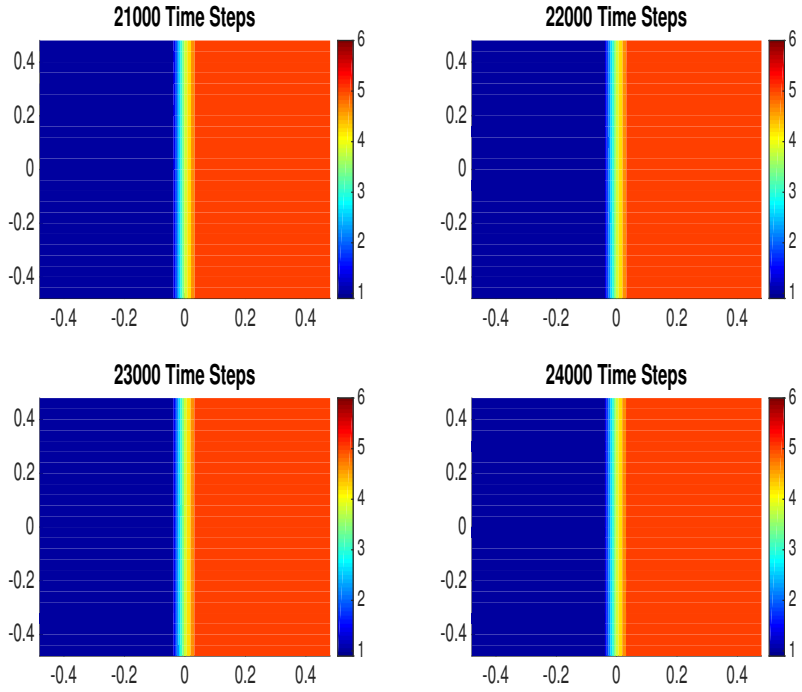

Figure 5.26 – Isodensity contour plots of the ensemble mean for the parameter $\delta = 0.05$ using the *RoeEC*1 scheme at 21000, 22000, 23000 and 24000 time steps.

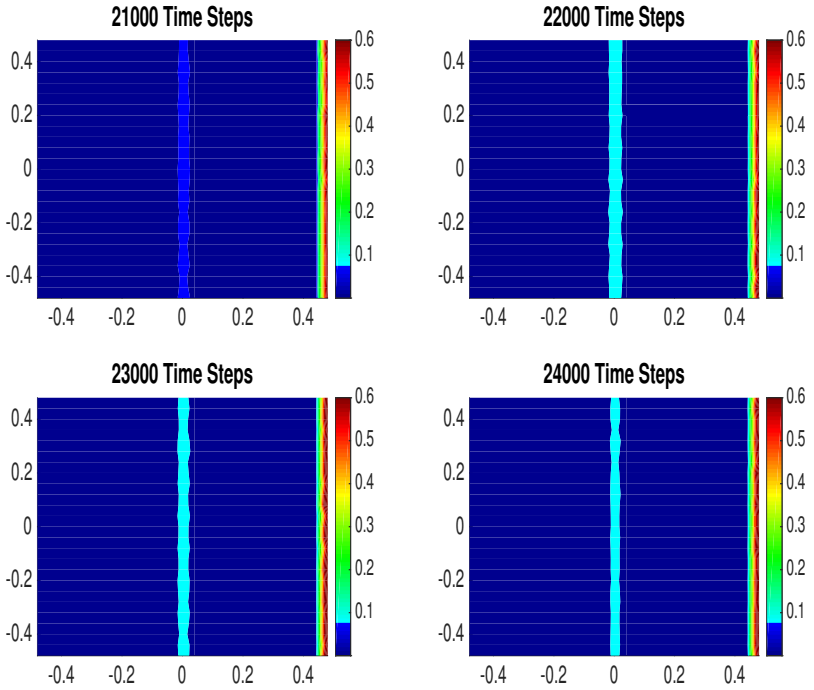

Figure 5.27 – Contour plots of the ensemble variance of the density for the parameter $\delta = 0.10$ using the *RoeEC*1 scheme at 21000, 22000, 23000 and 24000 time steps.

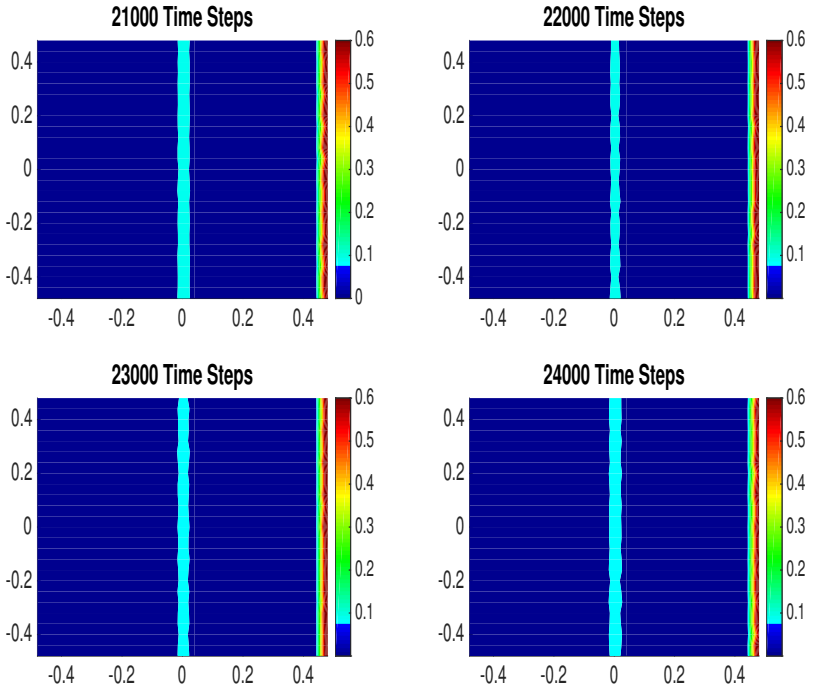

Figure 5.28 – Contour plots of the ensemble variance of the density for the parameter $\delta = 0.05$ using the *RoeEC*1 scheme at 21000, 22000, 23000 and 24000 time steps.

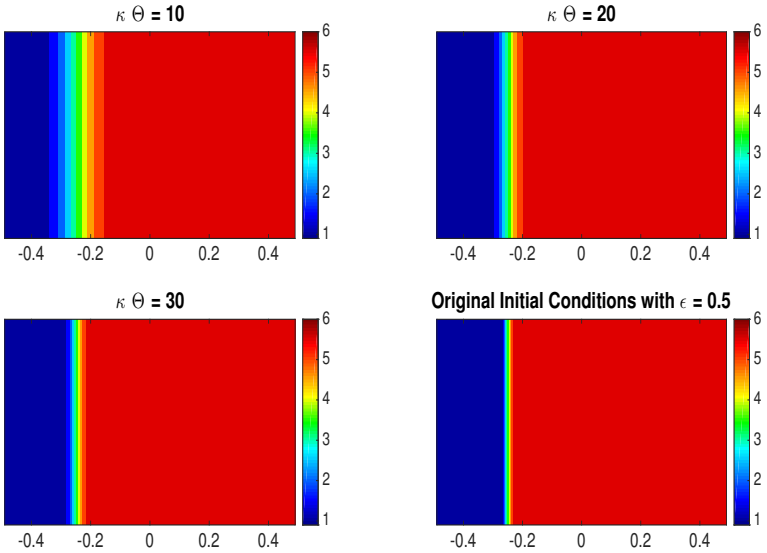

Figure 5.29 – Isodensity contour plots of the initial conditions for different realisations of the random variable Θ along with the original non-random initial conditions.

Cauchy problem introduced in Section (5.1) with initial conditions given by

$$\mathbf{U}_0(x,y) = \mathbf{U}_L + \mathbf{U}_R \frac{2}{\sqrt{\pi}} \int_0^{\kappa\Theta x} e^{-t^2} dt \tag{5.8}$$

where

$$\mathbf{U}_L = \begin{bmatrix} \dfrac{1+f(M_0)}{2} \\ 1 \\ 0 \\ \dfrac{\frac{1}{\gamma(\gamma-1){M_0}^2} + \frac{1}{2} + \frac{g(M_0)}{\gamma(\gamma-1){M_0}^2} + \frac{1}{2f(M_0)}}{2} \end{bmatrix} \tag{5.9}$$

and

$$\mathbf{U}_R = \begin{bmatrix} \dfrac{f(M_0)-1}{2} \\ 1 \\ 0 \\ \dfrac{\frac{g(M_0)}{\gamma(\gamma-1){M_0}^2} + \frac{1}{2f(M_0)} - \frac{1}{\gamma(\gamma-1){M_0}^2} + \frac{1}{2}}{2} \end{bmatrix}. \tag{5.10}$$

Thus, this experiment is essentially an extension of Experiment 2 in Chapter 4 in two dimensions. The remaining set up including the boundary

conditions is left unchanged. Once again we introduce a source of multi-dimensional instability by seeding a single randomly chosen cell upstream of the shock with a perturbation of the order of 10^{-14} and we then use Monte Carlo simulations to estimate the mean and variance of the approximate measure valued solutions and analyse the stability and convergence of these statistical quantities. Similar to Experiment 1, we focus specifically on the test cases with parameter values $\kappa = 10,\ \varepsilon = 0.7,\ M_0 = 6$ for the *RoeEC*1 ($\alpha = 0.2$) scheme. All results were computed using 400 Monte Carlo iterations.

Figure 5.30 and Figure 5.31, which display the density plot and the isodensity contour plots of the *RoeEC*1 scheme for $\varepsilon = 0.7$, clearly indicates that the *RoeEC*1 scheme seems to produce an ensemble mean of the density that does not suffer from $1 - 1/2D$ numerical instability. Indeed, the ensemble mean consists of a sharply resolved steady state shock with very little deviation of the shock location and no appearance of oscillating spikes that plague individual sample simulations.

Figure 5.32 displays the ensemble variance the density for both the *RoeEC*1 scheme. Once again we observe that the variance consists of a smaller spike at the shock location and a sharper spike at the outflow boundary. We also observe that the variance at the shock location does oscillate slightly, which likely indicates unresolved $1D$ shock instability but the variance at the outflow appears stable. This result therefore seems to imply that while $1D$ numerical instability is not completely resolved, both the ensemble mean and variance do not suffer from $1 - 1/2D$ numerical instability.

The analysis of the error residuals supports our conclusion. Figure 5.33 displays the $L1$-norm of the difference between initial condition and the ensemble mean of the density at each time step for the *RoeEC*1 scheme. Once more, two important points can immediately be inferred from the plot. First, the error for the ensemble mean is much smaller than the error of the original solution and second the oscillations in the error residual of the ensemble mean is significantly smaller than the oscillations in the error residual of the original solution. This is extremely similar to our results from Experiment 1 and we feel that this constitutes further evidence that while $1D$ numerical instability in the form of an unstable shock position can persist in the ensemble mean and variance, the entropy measure valued framework is nevertheless successful at resolving the $1 - 1/2D$ numerical instability.

In order to shed further light on these results, we also explore the effects of increasing the value of the parameter κ on the convergence of the ensemble mean and variance of the entropy measure valued solutions produced by the *RoeEC*1 ($\alpha = 0.2$) scheme. In particular we repeat the same experiment for the value $\kappa = 20$. Figure 5.34 displays the $L1$-norm of the difference between the initial condition and the ensemble mean of the density of the

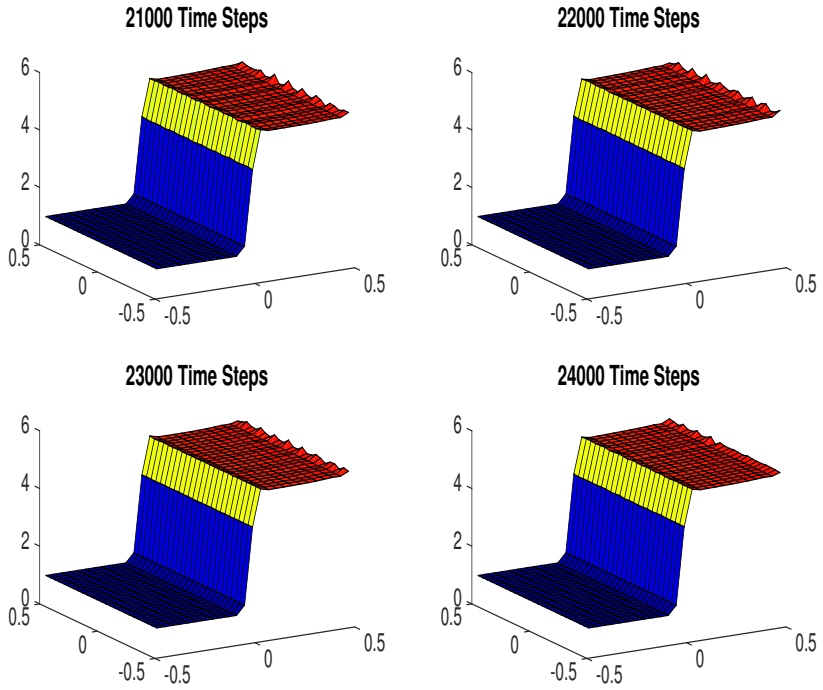

Figure 5.30 – Density plots of the ensemble mean for $\kappa = 10$ using the *RoeEC*1 scheme at 21000, 22000, 23000 and 24000 time steps.

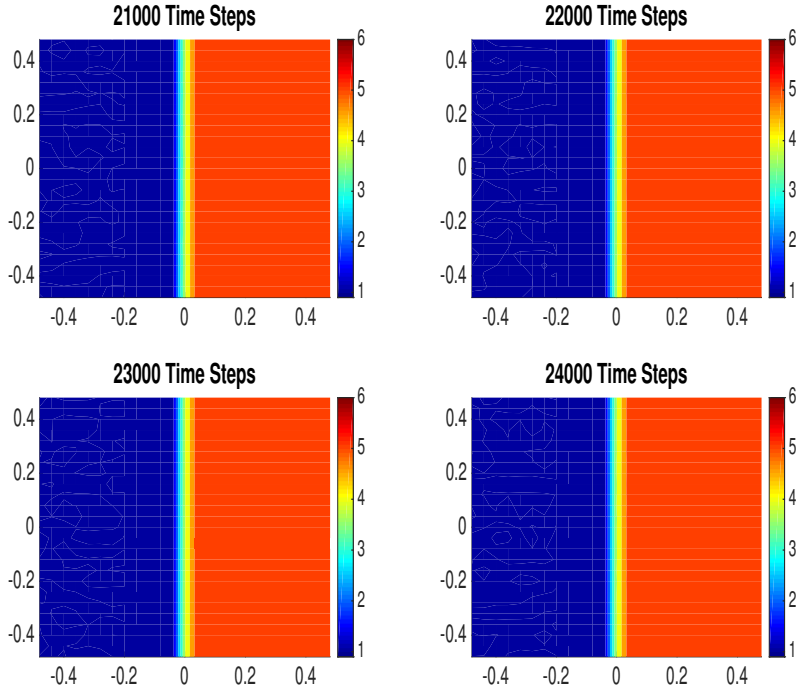

Figure 5.31 – Isodensity contour plots of the ensemble mean for $\kappa = 10$ using the *RoeEC*1 scheme at 21000, 22000, 23000 and 24000 time steps.

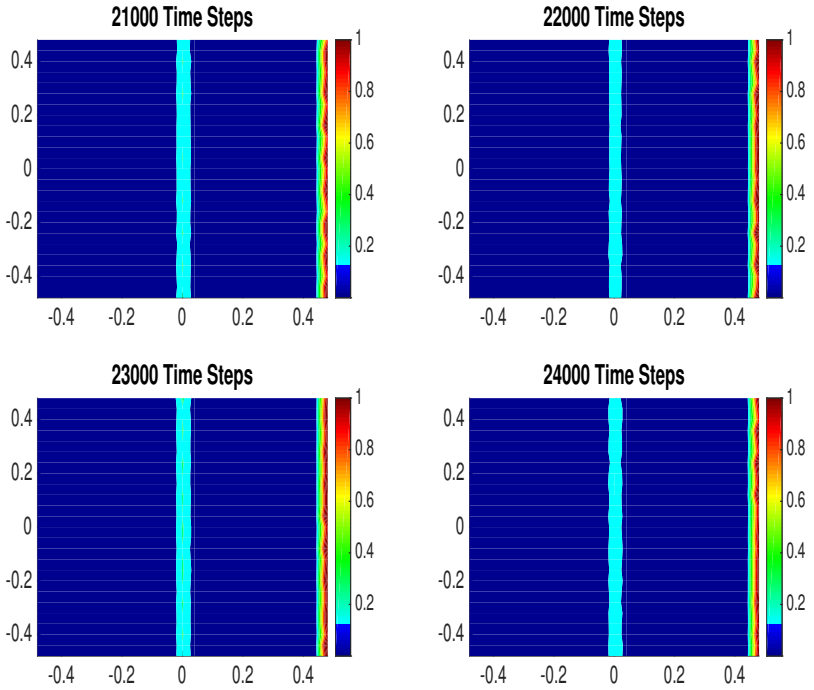

Figure 5.32 – Contour plots of the ensemble variance of the density for $\kappa = 10$ using the *RoeEC*1 scheme at 21000, 22000, 23000 and 24000 time steps.

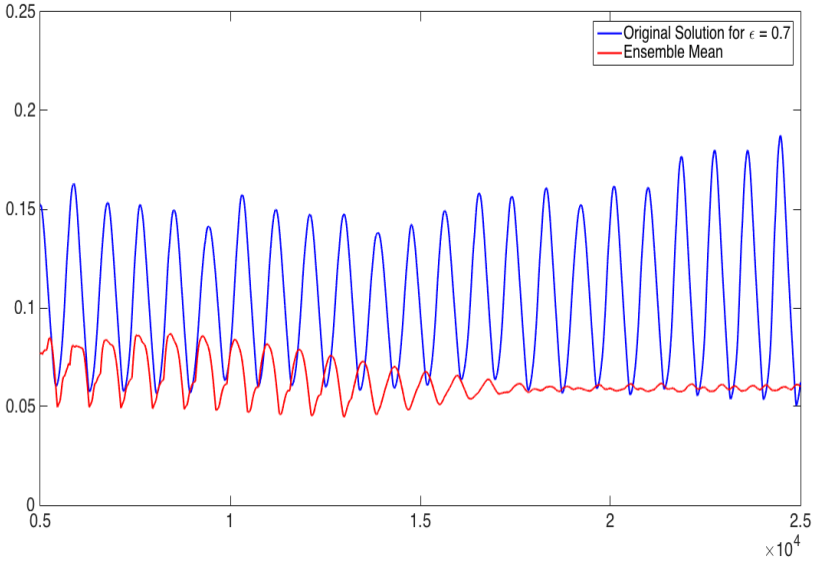

Figure 5.33 – The error $\|\rho_0 - \rho^n_\Delta\|_{L^1}$ vs. the number of time steps for the ensemble mean for $\kappa = 10$ and the original solution with $\varepsilon = 0.7$.

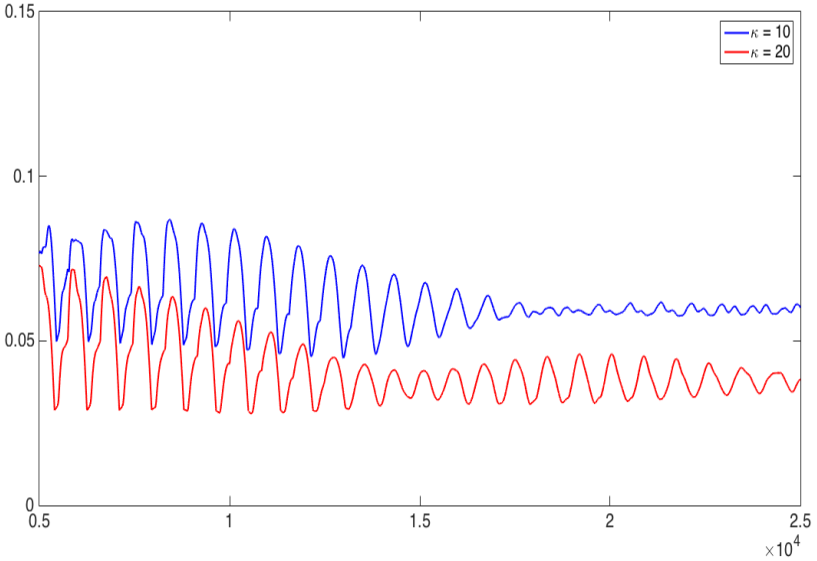

Figure 5.34 – The error $\|\rho_0 - \rho_\Delta^n\|_{L^1}$ vs. the number of time steps for both $\kappa = 10$ and $\kappa = 20$ using the *RoeEC*1 scheme.

approximate entropy measure valued solution at each time step for both $\kappa = 20$ and $\kappa = 10$. Clearly, the error residual for $\kappa = 20$ is smaller than the error residual for $\kappa = 10$ and this seems to indicate that the ensemble mean is stable under increasing values of κ. We note however that the error residual for $\kappa = 20$ still suffers from oscillations which indicates that ensemble mean is still afflicted by $1D$ numerical instability and has not converged to a steady state solution even after $20,000$ time steps.

Figure 5.35 and Figure 5.36 display the density plot and the isodensity contour plots of the ensemble mean of the density for $\kappa = 20$. We immediately observe that the mean does not appear to suffer from the more severe $1 - 1/2D$ numerical instability and in fact the solution consists of a sharply resolved shock. This supports the conclusion that the oscillations in the error residual for the case $\kappa = 20$ is due to $1D$ numerical instability in the form of an oscillating shock position.

We obtain a similar result for the ensemble variance of the density. Figure 5.37 displays the ensemble variance for $\kappa = 20$. Once again we observe that the variance consists of a smaller spike at the shock location and a sharper spike that the outflow boundary. Furthermore, the variance seems more stable for $\kappa = 20$ and the oscillation in the variance is not as prominent as in the case $\kappa = 10$. We therefore conclude that the ensemble variance is also stable under increasing values of κ. We feel that this is a strong indication that the entropy measure valued solution framework is successful at resolving the $1 - 1/2D$ carbuncle phenomenon.

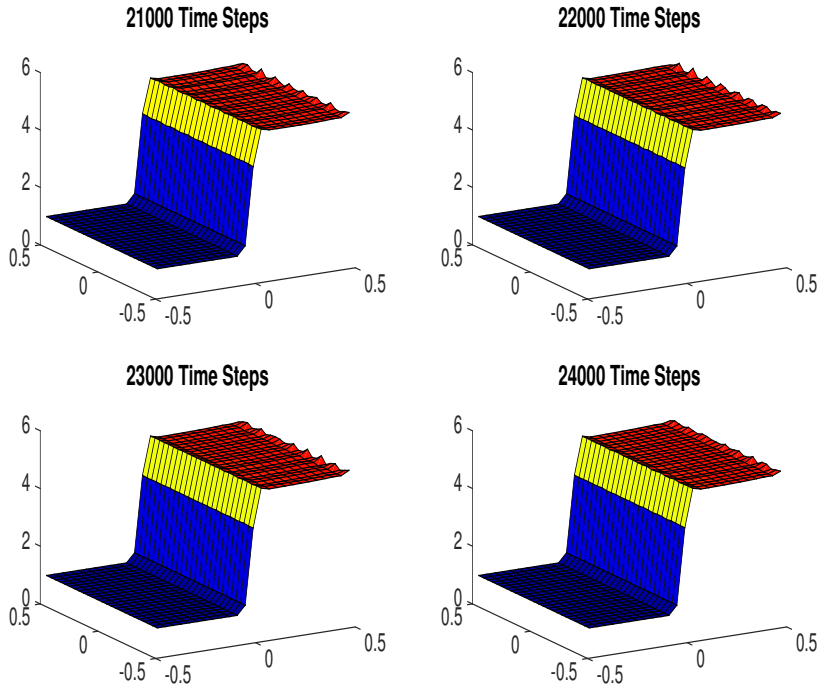

Figure 5.35 – Density plots of the ensemble mean for $\kappa = 20$ using the *RoeEC*1 scheme at 21000, 22000, 23000 and 24000 time steps.

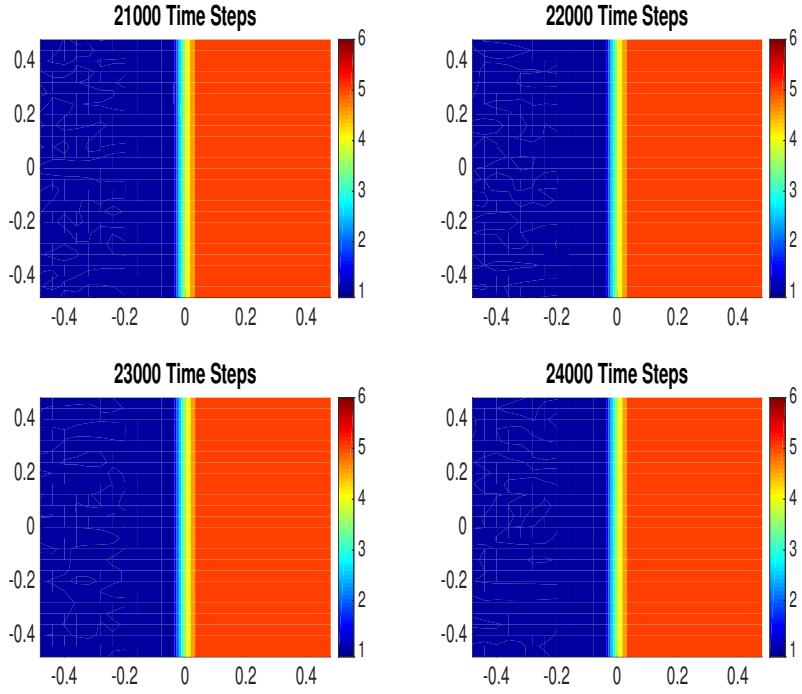

Figure 5.36 – Isodensity contour plots of the ensemble mean for $\kappa = 20$ using the *RoeEC*1 scheme at 21000, 22000, 23000 and 24000 time steps.

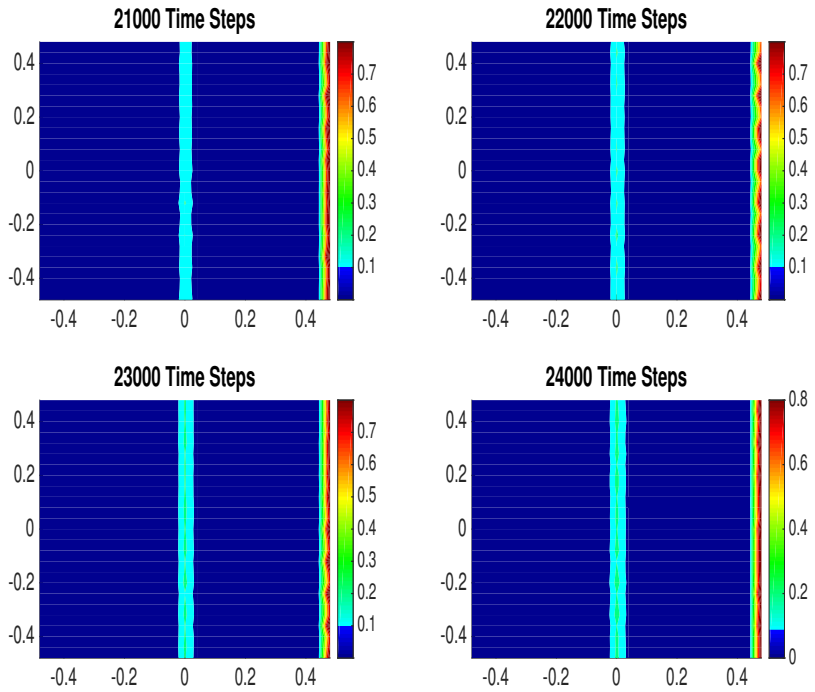

Figure 5.37 – Contour plots of the ensemble variance of the density for $\kappa = 20$ using the *RoeEC*1 scheme at 21000, 22000, 23000 and 24000 time steps.

Once again we feel that the same fundamental conclusions can be drawn in light of the results of Experiment 2:

- The error residual of the ensemble mean of the density of the corresponding measure valued Cauchy problem is significantly smaller than the error residual of the solution to the original Cauchy problem.
- The ensemble mean and variance still suffer from $1D$ numerical instability but do not appear to suffer from the more severe $1 - 1/2D$ instability.
- Both the ensemble mean and the ensemble variance seem to be stable under increasing values of the parameter κ.

To summarise, the results of Experiment 1 and Experiment 2 both seem to support the conclusion that the $1 - 1/2D$ carbuncle phenomenon can be successfully resolved in some cases simply by considering a corresponding MV Cauchy problem and calculating the ensemble mean and ensemble variance. Of course this methodology only works for schemes that are $1 - 1/2D$ unstable of type 1 and in particular this includes the entropy consistent *RoeEC*1 scheme. In light of the failure of the entropy measure valued solution framework to resolve the much more simple $1D$ carbuncle phenomenon we feel

that our results constitute evidence that the nature of these two forms of numerical instability is different. We conclude by remarking that from a purely practical point of view the ensemble mean of the entropy measure valued solutions produced by the *RoeEC*1 scheme in fact have a significantly smaller error residual than both the Rusanov scheme and the entropy stable *RusanovES* scheme, which therefore makes ensemble averaging an attractive choice for sharply resolving steady shocks.

Chapter 6

The Carbuncle Phenomenon in 2D

6.1 Numerical Experiments in 2D

The final step in our analysis is to consider the full-fledged Carbuncle problem in two dimensions. As mentioned previously, K. Peery and S. Imlay first observed this numerical instability when computing hypersonic flows past a blunt-body object [35]. Essentially, the use of the original Roe solver resulted in a solution consisting of a pair of oblique shocks rather than a smooth bow shock profile upstream of the solid cylinder. As a first step therefore, we attempt to replicate this result using the various schemes introduced in Chapter 4.

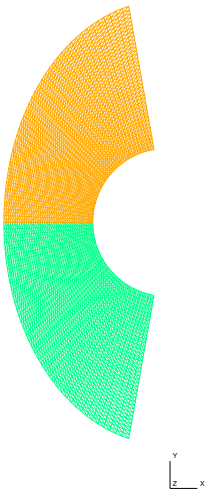

Figure 6.1 – Computational domain with a non-Cartesian Voronoi-type Mesh.

We consider the compressible Euler equations (5.1) along with the equation of state for an ideal, polytropic gas given by (5.3). Figure 6.1 displays the computational domain, which consists of a non-cartesian Voronoi-type mesh with a total of 6084 cells. The semi-circle at the right represents a solid cylinder and we therefore employ slip boundary conditions at this edge. In addition, we employ far-field boundary conditions at the left edge and outflow boundary conditions at the top and bottom edges.

We employ the following constant initial conditions for the purpose of this numerical experiment:

$$\mathbf{U}_0(x,y) = \begin{bmatrix} 1 \\ 1 \\ 0 \\ \frac{1}{\gamma(\gamma-1)M_0^2} \end{bmatrix} \tag{6.1}$$

where M_0 is the free-stream Mach number. Our goal is to analyse the steady-state solution for different values of the Mach number $M_0 \in \{2.0, 4.0, \ldots, 20.0\}$ and different choices of numerical schemes and we therefore categorise our numerical schemes in the following way:

- We declare a numerical scheme to be $2D$ **stable** if the steady state solution produced by the scheme consists of a smooth bow shaped shock upstream of the circular cylinder for all values of M_0.
- We declare a numerical scheme to be $2D$ **unstable type 1** if the steady state shock solution produced by the scheme consists of a non-smooth shock profile for some value of M_0 but does not suffer from a fully developed carbuncle in the form of oblique shocks for any value of M_0.
- We declare a numerical scheme to be $2D$ **unstable type 2** if the steady state shock solution produced by the scheme consists of a full fledged carbuncle in the form of two oblique shocks upstream of the circular cylinder for some value of M_0.

All simulations were performed using a CFL number of $1/2$ and were run until the flux residue dropped below 10^{-6}.

6.1.1 Results of the Numerical Experiments

As expected, our results indicate that the stability of the steady state shock solution depends on the value of the Mach number and the choice of numerical schemes. Table 6.1 displays the results of this $2D$ stability tests for various schemes. We remark however, that these simulations have all been performed for a specific choice of the mesh and it conceivable that using

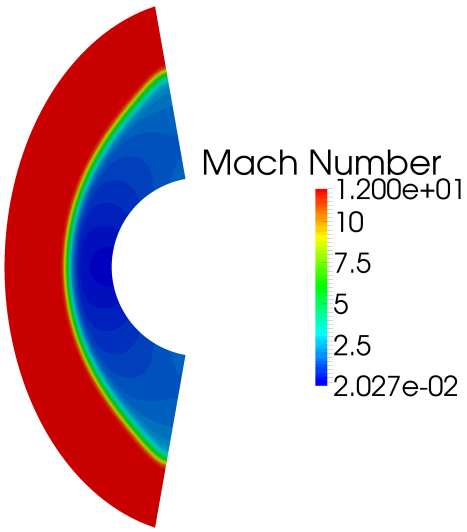

Figure 6.2 – **Stable**. Mach number plot of the steady state solution produced by the *RusanovES* scheme for $M_0 = 12$.

a different type of mesh with different mesh-width could result in slightly different results.

Scheme	$2D$ Stability
Rusanov	Stable
RusanovES	Stable
*RoeEC*1 $(\alpha = 0.2)$	Unstable Type 2
*RoeEC*1 $(\alpha = 0.8)$	Unstable Type 2
Roe	Unstable Type 1
RoeES	Unstable Type 1

Table 6.1 – Summary of the $2D$ stability of different numerical schemes.

Once again we observe that the numerically diffusive Rusanov and entropy stable *RusanovES* schemes produce a smooth bow shaped shock with no instability. Figure 6.2 for instance displays the approximate solution Mach numbers produced by the entropy stable *RusanovES* scheme for $M_0 = 12$ and we immediately observe that the solution appears to be completely stable.

On the other hand our results indicate that the original Roe scheme, the *RoeEC*1 schemes and the *RoeES* scheme all exhibit varying degrees of numerical instability. In fact, the *RoeEC*1 $(\alpha = 0.2)$ and $(\alpha = 0.8)$ schemes both exhibit the full-fledged Carbuncle phenomenon for different values of M_0. Figure 6.3 for instance displays the approximate solution Mach numbers for

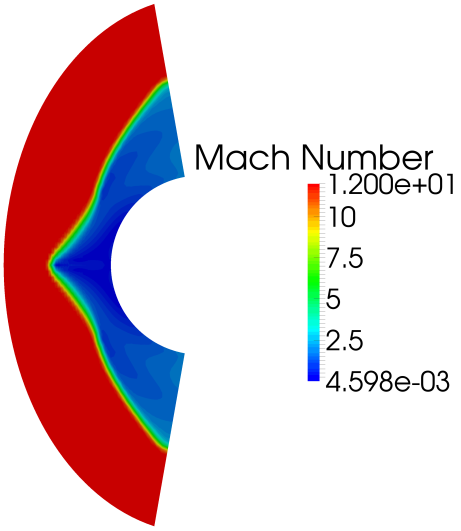

Figure 6.3 – **Unstable**. Mach number plot of the steady state solution produced by the *RoeEC*1 ($\alpha = 0.2$) scheme for $M_0 = 12$.

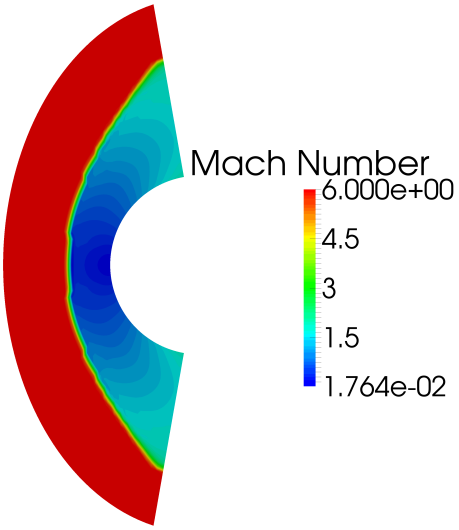

Figure 6.4 – **Unstable**. Mach number plot of the steady state solution produced by the *RoeES* scheme for $M_0 = 6$.

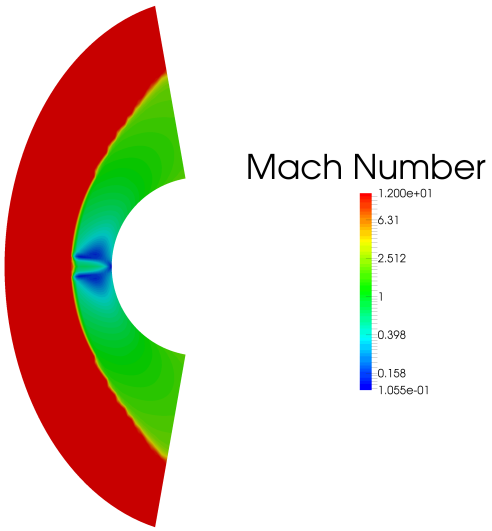

Figure 6.5 – **Unstable**. Mach number plot of the steady state solution produced by the original *Roe* scheme for $M_0 = 12$ with log-scale colour mappings.

$M_0 = 12$ produced by the $RoeEC1$ $(\alpha = 0.2)$ scheme and we observe immediately that the solution consists of unphysical oblique shocks that have been mentioned in the literature (see, e.g., [15, 34, 35]). A similar result is also obtained for the $RoeEC1$ $(\alpha = 0.8)$ scheme. We remark however that this carbuncle is only exhibited for specific values of M_0. At other values, the $RoeEC1$ scheme displays simple numerical instability of type 1.

Figure 6.4 displays the Mach numbers of the the approximate steady state solution produced by the $RoeES$ scheme and while solution does not consist of a fully developed carbuncle, there is nevertheless visible numerical instability in the form of of a non-smooth shock profile. This clearly indicates that while the $RoeES$ scheme does not produce a completely unphysical solution, it is nevertheless slightly unstable. A similar result is obtained for the original Roe scheme as displayed in Figure 6.5.

6.2 Numerical Experiments Involving Perturbed Initial Conditions

In this section we explore the effects of perturbing the initial conditions of the Cauchy problem (6.1) on the steady state solutions produced by our numerical schemes. Clearly, we can only expect the framework of entropy measure valued solutions to be able to resolve this $2D$ numerical instability if the approximate solutions produced by the numerical schemes exhibit some form of moderate instability with respect to perturbations of the initial conditions.

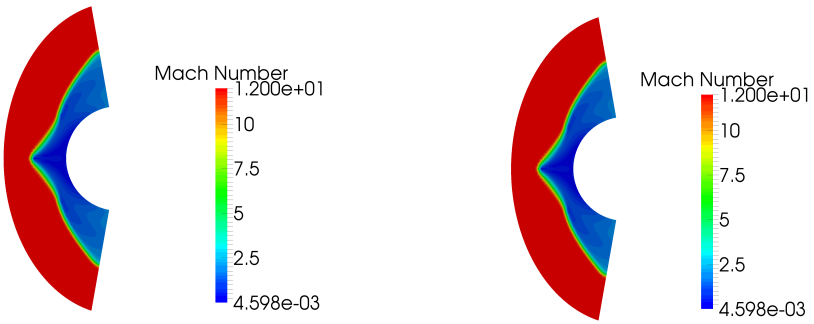

Figure 6.6 – (Left to Right) Steady state solution produced by the $RoeEC1$ ($\alpha = 0.2$) scheme with unperturbed and perturbed initial velocity in the y-direction $v_0 = 0.5$.

We begin by considering the $RoeEC1$ scheme, which is $2D$ unstable of type 2. As displayed in Figure 6.6, perturbing the initial value of the velocity in y-direction has no effect on the steady state solution produced by the $RoeEC1$ ($\alpha = 0.2$) scheme at all. Indeed, the mach number plot of the steady state shock solution still consists of a carbuncle. We obtain similar results for the $RoeEC1$ ($\alpha = 0.8$) scheme and for perturbations of other initial conditions.

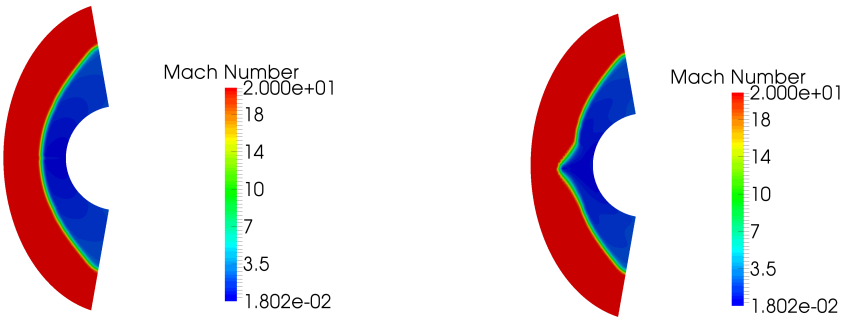

Figure 6.7 – (Left to Right) Steady state solution produced by the $RoeEC1$ ($\alpha = 0.2$) scheme at $M_0 = 20$ with unperturbed and perturbed initial velocity in the y-direction $v_0 = 10^{-6}$.

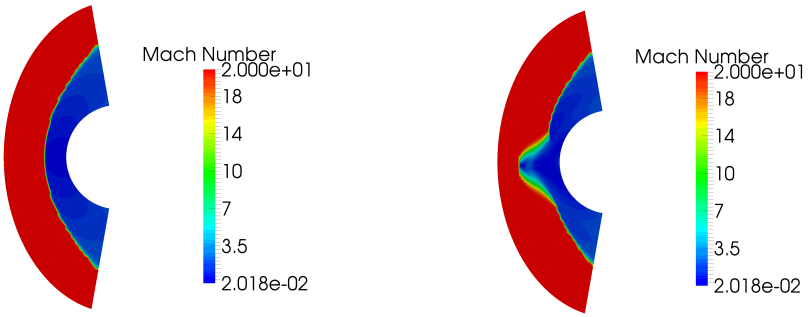

Figure 6.8 – (Left to Right) Steady state solution produced by the original Roe scheme at $M_0 = 20$ with unperturbed and perturbed initial velocity in the y-direction $v_0 = 10^{-6}$.

Furthermore, perturbing the initial conditions for a value of M_0 that originally produces an unstable type 1 solution actually results in a steady state solution that consists of a fully developed carbuncle. Indeed, Figure 6.7 indicates that perturbing the initial y-direction velocity in the case of the $RoeEC1$ ($\alpha = 0.2$) scheme with free-stream Mach number $M_0 = 20$ changes the stability of the solution from unstable type 1 to unstable type 2. These result very strongly indicate that the carbuncle solution produced by the unstable type 2 schemes is highly stable. It is therefore unreasonable to expect ensemble averaging to be able to resolve this type of instability.

Next we consider the effect of perturbing the initial conditions on the unstable type 1 numerical schemes. Here we observe a significant difference between the entropy stable $RoeES$ scheme and the original Roe scheme. Our results indicate that there is little effect of perturbing the initial conditions on the steady state solution produced by the $RoeES$ scheme. On the other hand as shown in Figure 6.8, perturbing the initial conditions even slightly results in the original Roe scheme changing from unstable type 1 to unstable type 2. In fact, the carbuncle now produced by the Roe scheme is even more pronounced than the carbuncle produced by the $RoeEC1$ ($\alpha = 0.2$) scheme.

Based on these results we conclude that the steady state carbuncle solution produced by the unstable numerical schemes listed in Table 6.1 is highly stable and therefore considering a corresponding MV Cauchy problem by perturbing the initial conditions (6.1) would not help in resolving $2D$ numerical instability. On the contrary, these numerical experiments indicate

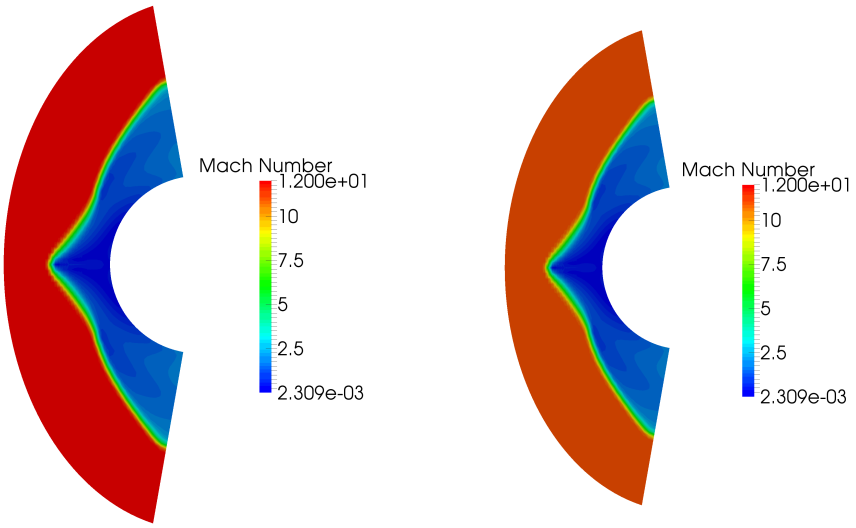

Figure 6.9 – (Left to Right) Steady state solution produced by the *RoeEC*1 scheme at $M_0 = 12$ and $M_0 = 10.5$.

that perturbing initial conditions does not result in any sort of moderate instability in the steady-state solution that we can exploit using ensemble averaging. Clearly therefore, the ensemble mean and variance of the approximate entropy measure valued solutions would continue to suffer from instability of types 1 and 2.

6.3 Numerical Experiments Involving Perturbed Far-Field Boundary Conditions

The next step in our analysis of $2D$ numerical instability is to explore the effects of perturbing the far-field boundary conditions on the steady state solutions to the Cauchy problem (6.1). In light of the failure of our usual approach of perturbing *initial conditions*, we hope that the effects of perturbing the far-field boundary conditions on the steady state solutions are more promising. Unfortunately, this does not appear to be the case as we discuss below.

We begin by exploring the effects of perturbing the far-field Mach Number on the steady state solution produced by the unstable numerical schemes listed in Table 6.1. Our results indicate that there is negligible effect on the structure of the numerical instability in every case and as shown in Figure 6.9 and Figure 6.10, unstable solutions of type 1 and type 2 continue to remain unstable with little observable difference. While the values of the conserved variables do change slightly, there is nevertheless no change in either the structure of fully developed carbuncle or the non-smooth shock

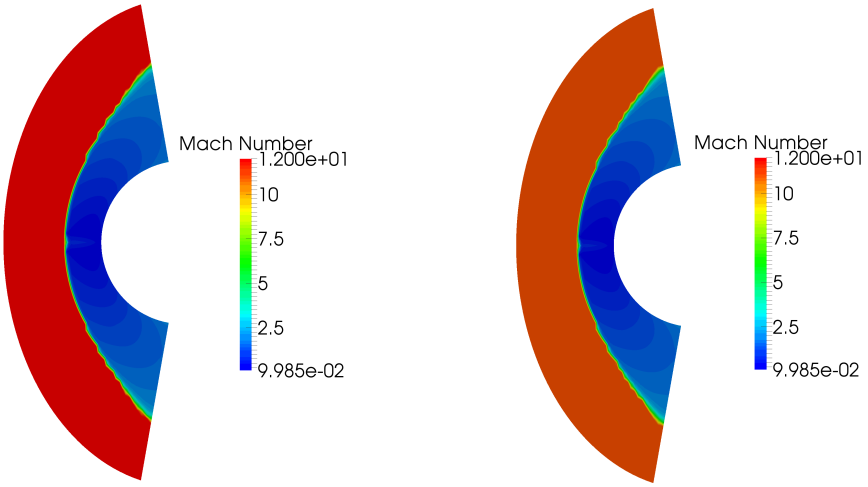

Figure 6.10 – (Left to Right) Steady state solution produced by the Roe scheme at $M_0 = 12$ and $M_0 = 10.5$.

profile. We conclude that perturbing the far-field Mach number has little effect on the unstable steady state solutions.

Hence, we focus primarily on perturbations of the far-field boundary value of the y-directional velocity. We consider the following $2D$ MV Cauchy problem involving the two dimensional Euler equations (5.1) by perturbing the initial conditions (6.1).

Let $(\Omega, \mathcal{F}, \mathbb{P})$ be a probability space, let $X\colon \Omega \to [-0.1, 0.1]$ be a uniformly distributed random variable and consider the same Cauchy problem introduced in Section (6.1) but with perturbed far-field boundary conditions given by

$$\mathbf{U}_{far-field} = \begin{bmatrix} 1 \\ 1 \\ X \\ \frac{1}{\gamma(\gamma-1)M_0^2} \end{bmatrix}, \tag{6.2}$$

The remaining set up including the initial conditions and the other boundary conditions are left unchanged. We again use Monte-Carlo simulations to estimate the mean and variance of the approximate entropy measure valued solutions to the associated $2D$ MV Cauchy problem and analyse the stability of these statistical quantities. As a concrete test case, we consider the $RoeEC1$ $(\alpha = 0.2)$ scheme with Mach number $M_0 = 12$. All results were computed using 100 Monte-Carlo iterations.

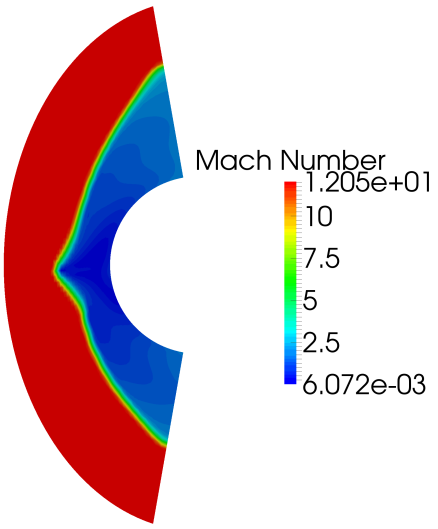

Figure 6.11 – Single sample steady state solution produced by the *RoeEC*1 scheme.

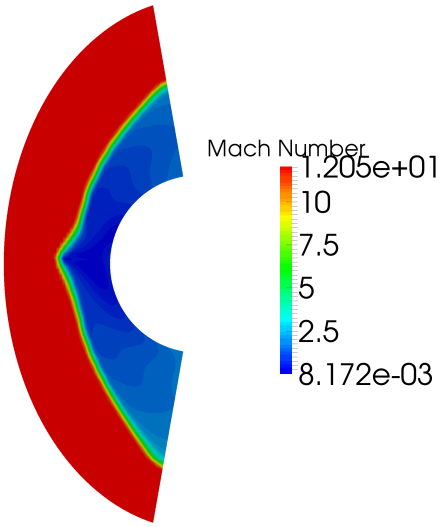

Figure 6.12 – Mach number plot of the ensemble mean of the approximate entropy measure valued solution produced by the *RoeEC*1 scheme.

Figure 6.11 displays the mach number plot of a single sample of the approximate entropy measure valued solution produced by the *RoeEC*1 scheme. We immediately observe that the mach number plot of the sample solution still consists of a fully developed carbuncle. The major qualitative difference however is that the so-called 'bulge' of the carbuncle is now asymmetric and tilted downwards. Unfortunately, this result also hints that perturbing the far-field boundary value of the y-directional velocity has little qualitative effect on the structure of the carbuncle.

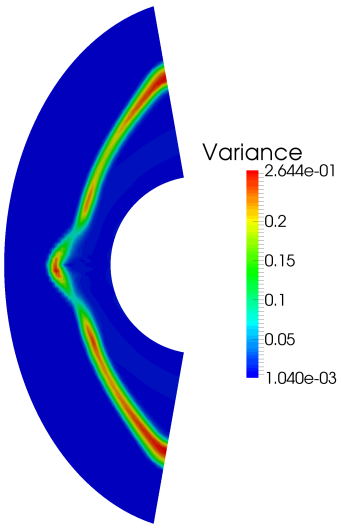

Figure 6.13 – Ensemble variance of the approximate entropy measure valued solution produced by the *RoeEC*1 scheme.

Figure 6.12, which displays the ensemble mean of the approximate entropy measure valued solutions confirms our conclusion. Clearly, the ensemble mean continues to suffer from the fully developed $2D$ Carbuncle phenomenon. Figure 6.13, which displays the ensemble variance indicates that while there is a slight variation in the location of the shock profile, it is not enough to produce carbuncle-free ensemble mean. We conclude therefore that $2D$ Carbuncle problem appears to be extremely stable and continues to afflict statistical quantities associated with the entropy measure valued solution to this MV Cauchy problem.

To summarise, the results of this section unequivocally support the following conclusions:

- The fully developed Carbuncle is extremely stable under perturbations of both the initial conditions as well the far-field boundary conditions.
- In several cases, perturbing the initial conditions can cause unstable solutions of type 1, which consist of a non-smooth shock profile, to evolve into unstable solutions of type 2, which instead consist of a full fledged carbuncle.
- The framework of entropy measure valued solutions is incapable of resolving this $2D$ numerical instability.

Chapter 7

Conclusions and Future Work

The entropy measure valued (EMV) solution paradigm is an exciting development in the study of hyperbolic systems of conservation laws. This framework has been successfully applied by S. Mishra and collaborators (see, e.g., [17, 18, 19]) to resolve issues of instability and lack of convergence in the well-known Kelvin-Helmholtz and Richtmyer-Meshkov problems (see, e.g., [18]). This thesis has been an attempt to use the structure created by S. Mishra and others to carry out a similar project for the Carbuncle problem in hypersonic compressible fluid flow.

We began by providing numerical evidence that even state-of-the-art, first-order finite volume schemes suffer from unstable shock resolution at very high Mach numbers in $1D$, $1-{}^{2}/_{2}D$ and $2D$ settings. In each of these settings we defined corresponding measure valued (MV) Cauchy problems and used numerical simulations to estimate statistical quantities of interest associated with the EMV solutions to these MV Cauchy problems.

Our results indicate that the ensemble mean and variance of the EMV solutions are somewhat more stable in the $1D$ setting and in certain cases significantly more stable in the $1-{}^{1}/_{2}D$ setting. Indeed, the results of several experiments in $1-{}^{1}/_{2}D$ indicate strongly that it is possible to successfully resolve the $1-{}^{1}/_{2}D$ Carbuncle phenomenon using ensemble averaging. Unfortunately, we were less successful in the case of the full fledged two-dimensional Carbuncle phenomenon and our results in the $2D$ setting indicate that it is likely not possible to obtain an ensemble mean and variance that is carbuncle-free simply by considering corresponding MV Cauchy problems.

Nevertheless, we do feel that we can draw some important conclusions from our work. First, we believe that the results of our numerical experiments very strongly support the prevalent view in the literature that the cause of the Carbuncle phenomenon in $2D$ is largely numerical in nature. In other

words unlike, for example, the Kelvin-Helmholtz instability problem, it is not possible to obtain completely stable statistical quantities unless the underlying numerical scheme is carbuncle-free. Second, we have demonstrated that in some cases in the $1 - 1/2D$ setting, it is nevertheless possible to produce significantly more stable statistical quantities using Monte Carlo methods and ensemble averaging, and we believe that this indicates that there is some underlying structure in the oscillations that afflict unstable numerical solutions. Contrasting this positive result with the more modest results we obtained in the $1D$ setting allows us to conclude that the so-called Carbuncle phenomenon manifests in crucially different ways in higher dimensions. In the absence of rigorous theoretical results explaining the cause of the Carbuncle phenomenon, we believe that this conclusion provides some insight into why, in some cases, trial-and-error approaches have not resulted in a universally accepted cure for the Carbuncle phenomenon (see, e.g., the comments of K. Kitamura et al in [28] regarding the HLLE solver).

The work presented in this thesis is by no means exhaustive in detail. In particular, we have not performed numerical simulations on extremely fine meshes and any future work in this direction should explore the effects of using even finer meshes on the Carbuncle phenomenon. Furthermore, our experiments in $2D$ were limited to a structured Voronoi-type mesh and it would be interesting to explore the effects of using a completely unstructured mesh. Finally, we would be interested in exploring the evolution of a fitted shock in $2D$ and comparing the results with our own experimental setup.

Bibliography

[1] Luigi Ambrosio and Nicola Gigli. A user's guide to optimal transport. In *Modelling and optimisation of flows on networks*, pages 1–155. Springer, 2013.

[2] Erik J. Balder et al. Lectures on young measures. *Cahiers de Mathématiques de la Décision*, 9517, 1995.

[3] John M. Ball. A version of the fundamental theorem for young measures. In *PDEs and continuum models of phase transitions*, pages 207–215. Springer, 1989.

[4] Timothy J. Barth and Dennis C. Jespersen. The design and application of upwind schemes on unstructured meshes. *AIAA*, 1989.

[5] Stefano Bianchini and Alberto Bressan. Vanishing viscosity solutions of nonlinear hyperbolic systems. *Annals of Mathematics*, pages 223–342, 2005.

[6] Yann Chauvat, Jean-Marc Moschetta, and Jérémie Gressier. Shock wave numerical structure and the carbuncle phenomenon. *International Journal for Numerical Methods in Fluids*, 47(8-9):903–909, 2005.

[7] Elisabetta Chiodaroli, Camillo De Lellis, and Ondrej Kreml. Global ill-posedness of the isentropic system of gas dynamics. *arXiv preprint arXiv:1304.0123*, 2013.

[8] Bernardo Cockburn, Frédéric Coquel, and Philipe G. LeFloch. Convergence of the finite volume method for multidimensional conservation laws. *SIAM Journal on Numerical Analysis*, 32(3):687–705, 1995.

[9] Bernardo Cockburn and Chi-Wang Shu. Tvb runge-kutta local projection discontinuous galerkin finite element method for conservation

laws. ii. general framework. *Mathematics of Computation*, 52(186):411–435, 1989.

[10] Michael G. Crandall and Andrew Majda. Monotone difference approximations for scalar conservation laws. *Mathematics of Computation*, 34(149):1–21, 1980.

[11] Constantine M. Dafermos. *Hyperbolic systems of conservation laws*. Springer, 1983.

[12] Ronald J. DiPerna. Convergence of approximate solutions to conservation laws. *Archive for Rational Mechanics and Analysis*, 82(1):27–70, 1983.

[13] Michael Dumbser, Jean-Marc Moschetta, and Jérémie Gressier. A matrix stability analysis of the carbuncle phenomenon. *Journal of Computational Physics*, 197(2):647–670, 2004.

[14] Bernd Einfeldt. On godunov-type methods for gas dynamics. *SIAM Journal on Numerical Analysis*, 25(2):294–318, 1988.

[15] Volker Elling. The carbuncle phenomenon is incurable. *Acta Mathematica Scientia*, 29(6):1647–1656, 2009.

[16] Lawrence C. Evans and Ronald F. Gariepy. *Measure theory and fine properties of functions*, volume 5. CRC press, 1991.

[17] Ulrik S. Fjordholm. *High-order accurate entropy stable numerical schemes for hyperbolic conservation laws*. PhD thesis, Eidgenössische Technische Hochschule ETH Zürich, Nr. 21025, 2013, 2012.

[18] Ulrik S. Fjordholm, Roger Y. Käppeli, Siddhartha Mishra, and Eitan Tadmor. Construction of approximate entropy measure valued solutions for hyperbolic systems of conservation laws. *arXiv preprint arXiv:1402.0909*, 2014.

[19] Ulrik S. Fjordholm, Siddhartha Mishra, and Eitan Tadmor. Arbitrarily high-order accurate entropy stable essentially nonoscillatory schemes for systems of conservation laws. *SIAM Journal on Numerical Analysis*, 50(2):544–573, 2012.

[20] Ami Harten. High resolution schemes for hyperbolic conservation laws. *Journal of computational physics*, 49(3):357–393, 1983.

[21] Ami Harten, Bjorn Engquist, Stanley Osher, and Sukumar R. Chakravarthy. Uniformly high order accurate essentially non-oscillatory schemes, iii. *Journal of computational physics*, 71(2):231–303, 1987.

[22] Andreas Hiltebrand and Siddhartha Mishra. Entropy stable shock capturing streamline diffusion space-time discontinuous galerkin (dg) methods for systems of conservation laws. *Num. Math., to appear*, 2013.

[23] Farzad Ismail. *Toward a reliable prediction of shocks in hypersonic flow: resolving carbuncles with entropy and vorticity control*. PhD thesis, University of Michigan, Ann Arbor, 2006.

[24] Farzad Ismail and Philip L. Roe. Affordable, entropy-consistent euler flux functions ii: Entropy production at shocks. *Journal of Computational Physics*, 228(15):5410–5436, 2009.

[25] Farzad Ismail, Philip L. Roe, and Hiroaki Nishikawa. A proposed cure to the carbuncle phenomenon. In *Computational Fluid Dynamics 2006*, pages 149–154. Springer, 2009.

[26] Jerome Jaffre, Claes Johnson, and Anders Szepessy. Convergence of the discontinuous galerkin finite element method for hyperbolic conservation laws. *Mathematical Models and Methods in Applied Sciences*, 5(03):367–386, 1995.

[27] Guang-Shan Jiang and Chi-Wang Shu. Efficient implementation of weighted eno schemes. Technical report, DTIC Document, 1995.

[28] Keiichi Kitamura, Philip L. Roe, and Farzad Ismail. Evaluation of euler fluxes for hypersonic flow computations. *AIAA Journal*, 47(1):44–53, 2009.

[29] S. N. Kružkov. First order quasilinear equations in several independent variables. *Sbornik: Mathematics*, 10(2):217–243, 1970.

[30] Hans P. Langtangen, Kent-Andre Mardal, and Ragnar Winther. Numerical methods for incompressible viscous flow. *Advances in Water Resources*, 25(8):1125–1146, 2002.

[31] Peter D. Lax. Hyperbolic systems of conservation laws ii. *Communications on Pure and Applied Mathematics*, 10(4):537–566, 1957.

[32] Randall J. LeVeque. *Finite volume methods for hyperbolic problems*, volume 31. Cambridge university press, 2002.

[33] Meng-Sing Liou and Christopher J. Steffen. A new flux splitting scheme. *Journal of Computational physics*, 107(1):23–39, 1993.

[34] Maurizio Pandolfi and Domenic D'Ambrosio. Numerical instabilities in upwind methods: analysis and cures for the "carbuncle" phenomenon. *Journal of Computational Physics*, 166(2):271–301, 2001.

[35] K. M. Peery and S. T. Imlay. Blunt-body flow simulations. *AIAA paper*, 2904:1988, 1988.

[36] James J. Quirk. *A contribution to the great Riemann solver debate*. Springer, 1997.

[37] Luc Tartar. Compensated compactness and applications to partial differential equations. In *Nonlinear analysis and mechanics, Heriot-Watt symposium*, volume 4, pages 136–211. Pitman, 1979.

ETH

Eidgenössische Technische Hochschule Zürich
Swiss Federal Institute of Technology Zurich

Declaration of originality

The signed declaration of originality is a component of every semester paper, Bachelor's thesis, Master's thesis and any other degree paper undertaken during the course of studies, including the respective electronic versions.

Lecturers may also require a declaration of originality for other written papers compiled for their courses.

I hereby confirm that I am the sole author of the written work here enclosed and that I have compiled it in my own words. Parts excepted are corrections of form and content by the supervisor.

Title of work (in block letters):

EXPLORING THE CARBUNCLE PHENOMENON IN HYPERSONIC FLOWS USING THE FRAMEWORK OF ENTROPY MEASURE VALUED SOLUTIONS.

Authored by (in block letters):

For papers written by groups the names of all authors are required.

Name(s):	**First name(s):**
HASSAN	MUHAMMAD

With my signature I confirm that

- I have committed none of the forms of plagiarism described in the 'Citation etiquette' information sheet.
- I have documented all methods, data and processes truthfully.
- I have not manipulated any data.
- I have mentioned all persons who were significant facilitators of the work.

I am aware that the work may be screened electronically for plagiarism.

Place, date	**Signature(s)**
ZÜRICH, 27/09/2015	Hassan

For papers written by groups the names of all authors are required. Their signatures collectively guarantee the entire content of the written paper.